POLITECNICO
MILANO 1863

SCUOLA DI INGEGNERIA INDUSTRIALE
E DELL'INFORMAZIONE

MOUETTE

Design and Commissioning of a Hybrid Rocket Engine with Optical Access

Tesi di Laurea Magistrale in
Aeronautical Engineering - Ingegneria Aeronautica

Author: **Fabio Angeloni**

Student ID:	944805
Advisor:	Prof. Roberto Andriani
Co-advisor:	Prof. Patrick Hendrick
Academic Year:	2020-21

Contents

Abstract iii
Abstract in lingua italiana iv
List of Figures v
List of Tables ix
Nomenclature x
1. Introduction 1
1.1 Hybrid Rocket Engines 1
1.1.1 Pros and Cons of Hybrid Propulsion Technology 2
1.1.2 Applications 4
1.1.3 New Frontiers of Hybrid Rocket Engines 6
1.2 Hybrid Rocket Combustion 7
1.2.1 Classical Fuels Combustion 7
1.2.2 Blocking Effect 9
1.2.3 Regression Rate Affecting Phenomena 10
1.2.4 Regression Rate Enhancing Techniques for Classical Hybrid Fuels 12
1.2.5 Non-Classical Liquefying Fuels Combustion 14
1.2.6 Generalized Hybrid Combustion Theory 18
2. Hybrid Rocket Visualization Experiments 19
2.1 Motivation 19
2.2 Previous Work and State of the Art 20
2.3 Objective of the Thesis Work 24
3. Design of a Hybrid Rocket Engine with Optical Access 26
3.1 Requirements and Applications 27
3.2 Oxidizer Selection 27
3.3 Metal Components 28
3.3.1 Combustion Main-Chamber, Pre-Chamber and Post-Chamber 30
3.3.2 Flanges and Welding 34
3.3.3 Window Frame 36
3.3.4 Injector Head and Injector Plate 37

3.3.5 Nozzle Plate 42
3.3.6 Grain Holder and Pre-Chamber Insert 43
3.4 Glass 44
3.4.1 Material Selection 44
3.4.2 Thickness Sizing 47
3.4.3 Glass Dimensioning and Interfaces 47
3.5 Gaskets 48
3.6 Fuel Grain 50
3.7 Nozzle 51
3.7.1 Exhaust System Overview 51
3.7.2 Combustion Process Estimation and Nozzles Selection 52
3.8 Feed System 55
3.8.1 Feed System Overview 55
3.8.2 Oxygen and Nitrogen Lines 55
3.8.3 Orifice 57
3.8.4 Pressure Transducers and Thermocouples 58
3.9 Ignition 59
3.10Test Bench 60
4. Engine Commissioning and Experimental Activity 63
4.1 Test Facility 63
4.2 Data Acquisition and Control System 64
4.3 Imaging Apparatus 66
4.4 Verification Test Campaign 67
5. Conclusions and Future Developments 71
APPENDIX A – Hybrid Combustion Model 73
APPENDIX B – List of MOUETTE components 75
APPENDIX C – Stress analysis of hollow bars 76
Bibliography 79
Acknowledgements 84
Ringraziamenti 85

Abstract

A Hybrid Rocket Engine (HRE) is a propulsion system where fuel and oxidizer are stored separately and in different phases. Although less widespread and common, hybrid propulsion technology offers significant safety and costs advantages with respect to Solid Rocket Motors (SRMs) and Liquide Rocket Engines (LREs). Thanks to the propellant configuration, hybrids have almost no explosion hazard and are therefore safer than solid motors. In addition, they feature controllable thrust as well as shut-off and restart capability. Compared to liquid engines, HREs are characterized by a simplified feed system resulting in reduced weight, improved reliability and, consequently, reduced costs. Furthermore, hybrid propulsion systems have increased performance than solid motors and a specific impulse almost comparable to liquids.
Nevertheless, despite the several advantages, the adoption of HREs has historically been inhibited by performance issues stemming from the diffusive nature of hybrid combustion and leading, for conventional fuels, to a slow burning rate and a consequent poor fuel flow production. Only in recent years, the discovery of fast-burning liquefying fuels, such as paraffin-based, has renewed the interest on hybrid propulsion and increased the awareness of this technology. However, HREs are still not widespread in today's space industry and the *Technology Readiness Level* associated to hybrid rocket propulsion is low. The main reason is that the hybrid combustion process is extremely complex and challenging, as it involves several coupled physical phenomena whose interdependencies have yet to be completely clarified.
Within this scenario, *MOUETTE* (Moteur OptiqUe pour ÉTudier et Tester Ergols hybrides) a lab-scale hybrid rocket engine with optical access was designed, developed and commissioned during the thesis work carried out in collaboration with the Aéro-Thermo-Mécanique Department of Université Libre de Bruxelles. The burner uses gaseous oxygen as oxidizer, with a mass flow rate up to 100 g/s, and is able to operate in a rather broad range of combustion chamber pressure, from atmospheric level to 15 bar. The test chamber features two quartz glass windows to allow high-speed imaging of combustion and a graphite nozzle to adjust the operating pressure. The feed system and the test bench have been designed and integrated into the test facility. Leak and proof tests have been performed together with an initial test campaign aimed at assessing the overall system functionality. The main goal of the project, in fact, is to provide an experimental setup enabling an extensive comprehension of hybrid rockets internal ballistics, thanks to its direct visualization and subsequent analysis. Real-time data of the hybrid combustion process will empower a detailed characterization of the phenomenon, as well as support the improvement of numerical models for CFD simulations, with the ultimate mission of contributing to make hybrid propulsion a competitive candidate for the next generation of launch systems and in-space missions, taking full advantage of its enhanced safety and low-cost benefits.

Keywords: Rocket Propulsion, Hybrid Rocket Engine, Optical Access, Liquefying Fuels, Combustion Visualization, Internal Ballistics.

Abstract in lingua italiana

Un motore a razzo ibrido (HRE) è un sistema di propulsione in cui il combustibile e l'ossidante sono conservati separatamente e in diverse fasi. Seppur meno diffusa, la tecnologia di propulsione ibrida offre significativi vantaggi in termini di sicurezza e costi rispetto agli endoreattori a propellente solido (SRM) e liquido (LRE). Grazie alla configurazione dei carburanti, gli ibridi hanno un rischio praticamente nullo di esplosione e sono quindi più sicuri degli endoreattori a solido. Inoltre, dispongono di una spinta regolabile e della capacità di spegnimento e riavvio. Rispetto agli endoreattori a liquido, gli HRE sono caratterizzati da un sistema di alimentazione semplificato che comporta un peso inferiore, una migliore affidabilità e, di conseguenza, costi ridotti. Inoltre, i sistemi di propulsione ibrida hanno prestazioni migliori rispetto ai motori solidi e un impulso specifico quasi paragonabile ai liquidi.
Tuttavia, nonostante i numerosi vantaggi, l'adozione degli HRE è stata storicamente inibita da problemi di prestazioni derivanti dalla natura diffusiva della combustione ibrida. Essa comporta, infatti, per combustibili convenzionali, una limitata velocità di regressione del combustibile e, di conseguenza, una scarsa produzione di flusso di carburante e di spinta. Solo negli ultimi anni, la scoperta dei cosiddetti *liquefying solid fuels*, ossia combustibili bassofondenti a combustione rapida come quelli a base di paraffina, ha rinnovato l'interesse nei confronti della propulsione ibrida e aumentato la consapevolezza di questa tecnologia. Tuttavia, gli HRE sono ancora poco diffusi nell'industria spaziale e il *Technology Readiness Level* ad essi associato è basso. La ragione principale è che il processo di combustione ibrido è estremamente complesso poiché coinvolge diversi fenomeni fisici accoppiati, le cui interdipendenze devono ancora essere completamente chiarite.
All'interno di questo scenario, *MOUETTE* (Moteur OptiqUe pour ÉTudier et Tester Ergols hybrides) un motore a razzo ibrido da laboratorio con accesso ottico è stato progettato, sviluppato e messo in funzione durante il lavoro di tesi realizzato in collaborazione con il Dipartimento di Aéro-Thermo-Mécanique dell'*Université Libre de Bruxelles*. Il combustore utilizza ossigeno gassoso come ossidante, con una portata fino a 100 g/s, ed opera in un intervallo piuttosto ampio di pressione in camera di combustione, da livelli atmosferici a 15 bar. La camera di prova dispone di due finestre in quarzo per consentire la visualizzazione della combustione e di un ugello in grafite per regolare la pressione operativa. Il sistema di alimentazione e il banco di prova sono stati progettati e integrati nella struttura di prova. Sono stati eseguiti test di tenuta e di calibrazione, oltre ad una campagna di test iniziale per verificare la funzionalità del sistema. L'obiettivo principale del progetto è quello di fornire un setup sperimentale che consenta un'estesa comprensione della balistica interna dei razzi ibridi, grazie alla sua visualizzazione diretta e alla successiva analisi. I dati in tempo reale del processo di combustione ibrida permetteranno una caratterizzazione dettagliata del fenomeno, così come il miglioramento dei modelli numerici per le simulazioni CFD, con la missione finale di contribuire a rendere la propulsione ibrida un candidato competitivo per la prossima generazione di sistemi di lancio e missioni nello spazio, sfruttando appieno i benefici di maggiore sicurezza e costi ridotti.

List of Figures

Figure 1.1 – Schematic of a hybrid rocket engine 1

Figure 1.2 – Single port vs multiport fuel grain design.....5

Figure 1.3 – Schematic of liquefying fuels combustion 6

Figure 1.4 – Schematic of the diffusion flame combustion process in a turbulent reacting boundary layer [20].....7

Figure 1.5 – Schematic of the blocking effect 9

Figure 1.6 – Variation of the regression rate in hybrid rockets with the total mass flux in a logarithmic plot [2].....11

Figure 1.7 – Water discharged at 30 bar from a showerhead injector (a) and a pressure-swirl injector (b) [12].....13

Figure 1.8 – Schematic of the entrainment phenomenon proposed by Karabeyoglu et al.....14

Figure 1.9 – Space-time-averaged regression rate vs. average oxidizer mass flux for various liquefying materials and HTPB [5] 16

Figure 2.1 – Combustion chamber set-up at Tokai University [24].....21

Figure 2.2 – Combustion visualization of paraffin-wax FT-105 produced by Nippon Serio, having (on average) 51 carbon and 104 hydrogen atoms [24] 21

Figure 2.3 – Progression of a roll wave in the liquid layer during an atmospheric pressure test [19] 21

Figure 2.4 – Filament-like structures in the combustion of blackened paraffin at non-atmospheric, subcritical, pressures [10] 22

Figure 2.5 – High-speed images of paraffin combustion at 4.9 bar. Nominal combustion (left) and blowing event (right) [20].....22

Figure 2.6 – High-speed images of paraffin combustion at 7.1 bar. Nominal combustion (left) and blowing event (right) [20].....23

Figure 2.7 – Schlieren images of paraffin combustion at 4.9 bar (left) and 7.1 bar (right) [20].....23

Figure 2.8 – High-speed images of paraffin combustion at 40 bar [29].....23

Figure 3.1 – Overview picture of some engine's components 26

Figure 3.2 – Picture of MOUETTE engine.....26

Figure 3.3 – Overview of the metal components of *MOUETTE* 29

Figure 3.4 – AISI 304L hollow bars during manufacturing 30
Figure 3.5 – CAD visualization of the Main-Chamber.....31
Figure 3.6 – CAD model section view of the Injector Plate and the Pre-Chamber.....32
Figure 3.7 – Fluid domain of the CFD injection simulation.....33
Figure 3.8 – Injection CFD simulation resulting streamlines.....33
Figure 3.9 – From left to right, picture of Post-chamber, Pre-Chamber and Main-Chamber 34
Figure 3.10 – Socket Flange Welding in a section view of the Post-Chamber drawing.....35
Figure 3.11 – External welding, Main-Chamber.....35
Figure 3.12 – Picture of the front and back of the Window Frame.....36
Figure 3.13 – CAD image of the Injector Head and the Injector Plate.....37
Figure 3.14 – Picture of the Injector Head and the Injector Plate.....37
Figure 3.15 – Injector Head picture.....37
Figure 3.16 – Section view of the Injector Head drawing (simplified version).....37
Figure 3.17 – Picture of Injector Head A (left) and Injector Plate B (right) 38
Figure 3.18 – Orifice schematic.....39
Figure 3.19 – Flowchart of the algorithm implemented to estimate the injection pressure.....41
Figure 3.20 – Section view of the Nozzle Plate drawing (simplified version) 43
Figure 3.21 – Nozzle Plate picture.....43
Figure 3.22 – CAD image of the Grain Holder and Pre-Chamber Insert placed on the respective chambers.....44
Figure 3.23 – Picture of the paraffin grain positioned on the Grain Holder 44
Figure 3.24 – Quartz Glass picture.....45
Figure 3.25 – Transmittance curves of optical materials [36].....46
Figure 3.26 – Reference image for a supported window [36].....47
Figure 3.27 – CAD image of the Glass positioned on the Main-Chamber.....48
Figure 3.28 – CAD section view of the Main-Chamber.....48
Figure 3.29 – O-ring deformation caused by a pressurized fluid [39].....49
Figure 3.30 – Static Application for O-rings with Axial Squeeze [38].....50

Figure 3.31 – Paraffin grain and pellets 50
Figure 3.32 – Mold for paraffin grains 50
Figure 3.33 – CAD section view of Post-Chamber, Nozzle Plate and Convergent Insert 51
Figure 3.34 – CAD section view of *MOUETTE* 51
Figure 3.35 – Regression Rate vs Oxygen Mass Flux plot 53
Figure 3.36 – Fuel Mass Flow Rate vs Oxygen Mass Flow Rate plot 53
Figure 3.37 – Oxidizer to Fuel Ratio vs Oxygen Mass Flow Rate plot 53
Figure 3.38 – Technical drawing of the 15 mm throat diameter Nozzle (simplified version) 54
Figure 3.39 – Picture of Nozzle and Nozzle Plate assembly 54
Figure 3.40 – Piping and instrumentation schematic of *MOUETTE*'s feed system 55
Figure 3.41 – Choked orifice manufacturing on the lathe of the ATM laboratory of Université Libre de Bruxelles from a hexagonal bar of brass 57
Figure 3.42 – Detail of the two 1/8" NPT threaded holes in the Post-Chamber 58
Figure 3.43 – Rocket candy positioned inside the engine 59
Figure 3.44 – Technical drawing of the frame Table 60
Figure 3.45 – Picture of the frame Table with Sole on it 60
Figure 3.46 – Picture of the Post-Chamber with particular attention to the central groove 61
Figure 3.47 – Detail of the Pre-Chamber connection to the test bench 61
Figure 3.48 – MOUETTE test bench 62
Figure 3.49 – Feedline mounted on the test bench 62
Figure 4.1 – Schematic of the test facility at Beauvechain Air Base 63
Figure 4.2 – Electrical schematic of the control box 64
Figure 4.3 – LabVIEW Virtual Instrument panel 65
Figure 4.4 – Test bench and imaging apparatus 66
Figure 4.5 – MOUETTE first firing test (31/03/2022) 67
Figure 4.6 – MOUETTE firing test, detail of the combustion process 67
Figure 4.7 – High-speed images of the flame development over the fuel surface during ignition. Oxygen flows from left to right 68

Figure 4.8 – CH* chemiluminescence images of paraffin combustion at 5 bar. Oxygen flows from left to right 69
Figure 4.9 – OH* chemiluminescence images of paraffin combustion at 2.5 bar, detected development of roll waves. Oxygen flows from left to right ...69
Figure C.1 – Representation of a generic elementary cube in a thick cylindrical vessel [45].....76
Figure C.2 – Diagrams of σ_t, σ_r and σ_a along the cylinder thickness as a function of the radius. Stress calculated with generic values, namely R_i=0.03 m, R_e=0.06 m, p_i=10 bar and p_e=1 bar. 77

List of Tables

Table 1.1 – Theoretical specific impulse comparison for rocket propulsion systems 3

Table 1.2 – Pentane and paraffin wax properties 17

Table 3.1 – Injection simulation parameters 32

Table 3.2 – Estimated discharge coefficients for Injector Plate A and B.....39

Table 3.3 – Estimated injection pressure as function of chamber pressure and oxidizer mass flow rate – Injector Plate A 42

Table 3.4 – Estimated injection pressure as function of chamber pressure and oxidizer mass flow rate – Injector Plate B.....42

Table 3.5 – Optical material properties [36].....46

Table 3.6 – Example of the characteristic velocity computation.....53

Table 3.7 – Description of *MOUETTE* feed system components as indicated in Figure 3.40 56

Table 3.8 – Description of *MOUETTE* pressure sensors and thermocouples.....58

Table B – List of *MOUETTE*'s components.....75

Table C – Maximum allowed internal pressure for the AISI 304L stainless steel hollow bars used for *MOUETTE*'s chambers manufacturing.....78

Nomenclature

A_b	Burning area [m²]
A_{eff}	Nozzle efflux area [m²]
A_O	Orifice throat area, Injector Plate modelling [m²]
A_t	Nozzle throat area [m²]
a	Experimentally obtained coefficient of regression rate expression
B	Blowing parameter
BF	Blocking factor
b	Parameter appearing in the discharge coefficient correlation
C_d	Discharge coefficient
$C_{d,\infty}$	Discharge coefficient in the limit of infinite Reynolds number
C_f	Skin friction coefficient
C_{f0}	Skin friction coefficient without blowing
C_h	Heat transfer coefficient
C_{h0}	Heat transfer coefficient without blowing
C_p	Specific heat at constant pressure [J/kg*K]
CR	Critical ratio
c^*	Characteristic velocity [m/s]
Da	Damköhler number
D_0	Length of window aperture [m]
F	Thrust [N]
G	Mass flux [kg/ m²s]
G_f	Fuel mass flux [kg/ m²s]
G_{ox}	Oxidizer mass flux [kg/ m²s]
h	Sum of sensible (thermal) and chemical (heat of formation) enthalpies [J/kg]
I_{sp}	Specific impulse [s]
K	Generalized constant for glass thickness sizing
Le	Lewis number
M_1	Injector Plate upstream Mach number
M_{eff}	Nozzle efflux Mach number
m	Experimentally obtained exponent of regression rate expression
$\dot{m}$	Mass flow rate [kg/s]
$\dot{m}_{ent}$	Mass flow rate of entrained liquid fuel droplets [kg/s]
$\dot{m}_f$	Fuel mass flow rate [kg/s]
$\dot{m}_{ox}$	Oxidizer mass flow rate [kg/s]
N	Number of holes for oxidizer passage in the Injector Plate
n	Experimentally obtained exponent of regression rate expression
O/F	Oxidizer to fuel ratio
Pr	Prandtl number

p_1	Injector Plate upstream pressure [Pa]
p_2	Injector Plate downstream pressure [Pa]
p_{amb}	Ambient pressure [Pa]
p_c	Combustion chamber pressure [Pa]
p_{eff}	Efflux pressure [Pa]
p_e	External pressure [Pa]
p_i	Internal pressure [Pa]
p_{T1}	Injector Plate upstream total pressure [Pa]
$\dot{Q}_c$	Convective heat flux [J/m²s]
$\dot{Q}_r$	Radiative heat flux [J/m²s]
Re	Reynolds number
R_e	External radius [m]
R_i	Internal radius [m]
r	Radius [m]
$\dot{r}$	Regression rate [m/s]
$\dot{r}_{vap}$	Regression rate due to solid fuel evaporation [m/s]
$\dot{r}_{ent}$	Regression rate due to entrainment [m/s]
T_f	Temperature at flame location [K]
T_s	Temperature of the solid fuel grain [K]
t	Glass thickness [m]
SF	Safety factor
u_c	Flow velocity at the flame location [m/s]
u_e	Flow velocity at the boundary layer edge [m/s]
u_w	Flow velocity at the fuel surface [m/s]
v_{eff}	Nozzle efflux velocity [m/s]
x	Axial coordinate in the boundary layer [m]
z	Exponent appearing in the discharge coefficient correlation
γ	Specific heats ratio
ΔH_f	Heat of gasification of the fuel [J/kg]
Δp	Pressure difference [Pa]
ϵ_g	Combustion gas grain emissivity
ϵ_r	Radial strain
ϵ_s	Solid fuel grain emissivity
ϵ_t	Tangential strain
λ	Thermal conductivity [W/m*K]
μ	Dynamic viscosity [Pa*s]
ρ_1	Injector Plate upstream density [kg/m³]
ρ_c	Flow density at the flame location [kg/m³]
ρ_e	Flow density at the boundary layer edge [kg/m³]
ρ_f	Fuel density [kg/m³]

ρ_w	Flow density at the fuel surface [kg/m^3]
σ	Stefan-Boltzmann constant [W/m^{2}K^4]
σ_a	Axial stress [Pa]
σ_r	Radial stress [Pa]
σ_t	Tangential stress [Pa]
σ_y	Tensile yield strength [Pa]
σ^*	Equivalent stress [Pa]
τ_{max}	Maximum shear stress [Pa]
τ_w	Shear stress at wall [Pa]

1. Introduction

1.1 Hybrid Rocket Engines

Hybrid Rocket Engines (HREs) are bipropellant rocket propulsion systems where fuel and oxidizer are stored separately and in different phases. Although there are many components that are common to the other major classes of rocket chemical propulsion, the operation of hybrids is different.

In solid rocket motors (SRMs), the propellant is contained and stored directly within the combustion chamber and consists of a mixture of oxidizer, fuel and other ingredients held together in a matrix of synthetic rubber or plastic binder. Solid rocket motors have a relatively low specific impulse (I_{sp}), but the high density of the propellant make them particularly suitable for boosters or first stages applications. From the mechanical point of view, they are very simple, nevertheless they are typically not able to be throttled or re-ignited.

A liquid propellant rocket propulsion system consists of one or more thrust chambers, a set of tanks where fuel and oxidizer are stored separately in liquid phase and a feed mechanism for supplying propellants from tanks to thrust chamber(s). Liquid rocket engines (LREs) offer the highest specific impulse, re-start and throttle ability, but the engine mechanical system is rather complex and costly.

Hybrid rocket engines provide an attractive alternative to conventional solid and liquid rockets as they are somehow placed in the middle between them. The most common hybrid configuration, usually referred as direct, classical or typical configuration, combines a solid fuel with a liquid or gaseous oxidizer. The inverse or reverse configuration, presenting a solid oxidizer and a liquid or gaseous fuel, is by far

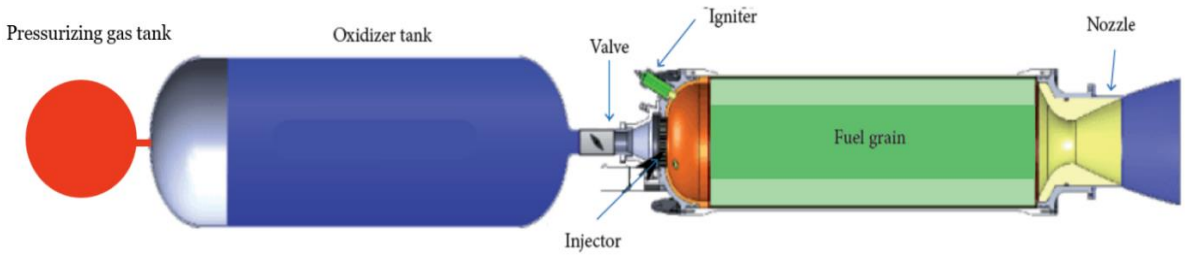

Figure 1.1: *Schematic of a hybrid rocket engine.*

less common and not widely used, and, therefore, it will not be covered nor studied in this work.

A classical hybrid rocket engine schematic is shown in Figure 1.1. The liquid (or gaseous) oxidizer is stored in a tank, like in a liquid system, which may have an external gas pressurization system. The latter is not necessary for hybrid motors using a 'self-pressurizing' oxidizer, such as nitrous oxide (N_2O), achieving pressurization thanks to its high vapor pressure. The oxidizer is delivered to the combustion chamber through a single feed system, controlled by a main run valve.

The oxidizer is then injected into the combustion chamber head end through an injector. In the case of a liquid oxidizer, the liquid is atomized and vaporized into a spray across the injector and in the fore end of the combustion chamber, also referred as pre-chamber. The solid fuel grain is stored directly in the combustion chamber, like in a solid motor. An igniter, usually located at the head of the combustion chamber, is used to vaporize some of the fuel so that, once the oxidizer flow enters the chamber, combustion initiates. Since fuel and oxidizer are not premixed and mixing happens during combustion itself, hybrid rocket engines are characterized by a diffusion flame. Combustion occurs in the reactive boundary layer above the fuel surface and the reaction is driven by solid fuel diffusion in the oxidizer stream. Burning reactions are completed along the length of the chamber and eventually in a post combustion chamber. Gaseous reaction products are then accelerated and expelled from a nozzle to generate thrust.

1.1.1 Pros and Cons of Hybrid Propulsion Technology

By storing fuel and oxidizer separately and in different phases, hybrids offer several advantages over liquid and solid rockets. The main benefits of hybrid technology are discussed in the following.

1) ***Safety.*** Since fuel and oxidizer are separated, hybrids have almost no explosion hazard. In contrast, solid propellant, where fuel and oxidizer are intimately mixed, are extremely dangerous, as cracks, grain imperfections, shocks, vibrations or static electricity may cause accidental ignitions and consequent explosions. Liquid fuels can be hazardous too, especially volatiles ones such as hydrogen, methane or kerosene. Therefore, hybrids provide enhanced safety compared to liquid and solid systems, for both the storage and the transportation of propellants.

2) ***Flexibility.*** Hybrid engines can be throttled, switched off and re-started by just adjusting the oxidizer mass flow rate, allowing thrust control and maneuvering with consequent greater mission flexibility. In solid rocket motors, a sort of throttle ability is possible but complex. The propellant grain can be shaped in

such a way that the burning area varies during firing, thus changing the mass flow rate and the thrust. However, it is clear that only thrust variation already planned during the design phase are possible. In liquid engines, throttling is not as easy as for hybrids since both fuel and oxidizer mass flow rates need to be precisely adjusted to match the desired values.

3) ***Reliability.*** Since only the oxidizer is stored in liquid or gaseous phase, hybrids require half of the feed system hardware of liquid engines. This implies reduced feed system weight, less complex design and improved reliability.

4) ***Performance.*** Hybrid motors have a higher theoretical specific impulse than solids and a higher volumetric specific impulse than liquids. A comparison of the usual range of specific impulse is reported in Table 1.1.

	Solid	**Liquid**	**Hybrid**
$I_{sp}\ [s]$	200 – 300	250 – 500	250 – 300

Table 1.1: *Theoretical specific impulse comparison for rocket propulsion systems.*

5) ***Insensitivity.*** Since hybrid fuel grains are not explosive, they are insensitive to cracks and imperfections. Combustion is limited to the reacting boundary layer developing on the fuel surface, therefore potential internal grain cracks, that may increase the burning area, have no significant effect on internal ballistic and chamber pressure. On the contrary, grain cracks and imperfections can have catastrophic consequences in solid rocket motors as they actually increase the burning area and, in turn, the chamber pressure beyond design limits.

6) ***Propellant versatility.*** Hybrids offer a quite vast propellant choice because two phases are available. The largest class of suitable fuels is that of polymeric synthetic rubbers based on polybutadiene monomer, such as polybutadiene acrylonitrile (PBAN) or hydroxyl-terminated polybutadiene (HTPB). Other hydrocarbons that have been used and tested are for example paraffin waxes, polyethylene or Plexiglas. In addition, the solid fuel provides a convenient matrix for introducing several additives. The latter can enhance either motor performance or grain mechanical properties. Liquid oxidizers used in hybrids can be either noncryogenic or cryogenic and they are essentially the same as for liquid engines, for instance oxygen(O_2), nitrous oxide (N_2O) or nitrogen tetroxide (N_2O_4).

7) ***Environmental friendliness.*** Green, non-hazardous and non-toxic propellants can be easily chosen as propellants. Hybrid most common combinations, such as liquid oxygen (LOX) and rubber-based fuels, have relatively clean exhaust with reduced environmental impact.

8) ***Low cost.*** The low cost of a hybrid propulsion system is mainly a consequence of propellants' high level of safety. The almost no explosion hazard allows to contain costs during manufacturing, transport, storage and tests. Moreover, expensive grain quality control operations are not necessary since combustion is not sensitive to crack or debonding of the fuel.

Despite the significant advantages, some drawback must be highlighted too.

1) ***Low regression rate.*** Due to the diffusive nature of hybrid combustion, conventional polymeric fuels, such as HTPB, show low regression rates, at least an order of magnitude slower than solid propellants [1].

2) ***Combustion efficiency.*** The fuel and oxidizer mixing and combustion occurring in a macroscopic diffusion flame zone may result in a lower overall combustion efficiency than competing chemical propulsion systems. To ensure a complete mixing and combustion, an aft combustion chamber is usually used, thus leading to a larger installation envelope and a poor volumetric loading.

3) ***O/F shift.*** During firing, the burning area increases as the fuel grain is consumed and its internal port becomes larger. This causes a time variation of the mixture ratio (O/F) and, therefore, a change in the internal ballistics, which can lower theoretical performances. However, with a proper design, this loss is minimal and it can be held to less than 1% for a typical hybrid [2].

1.1.2 Applications

The versality of propellants available, the large range of performance capability and the thrust flexibility make hybrids theoretically suitable for all rocket applications. In order to be competitive, hybrids need to maintain safety, low cost and simplicity features while reaching equal or better performance than solid and liquid systems. The main possible hybrid rocket engine applications are the following:

- Sounding Rockets. Because of the low cost, safety of operation and wide propellant range, sounding rocket represent one of the most extensive uses of hybrid technology.
- Tactical Rockets. The throttle ability of hybrids is extremely appealing for tactical rockets, which make a hybrid engine favourable over a solid motor where the compact envelope requirement is not too restrictive.
- Space Engines. Throttling and start/stop features are ideal to provide either a coasting phase or thrust termination for exact final velocity in orbital insertion.
- Thrust Augmentation. Hybrids can be used as additional engines for thrust augmentation to shape exo-atmospheric trajectory.

- Suborbital Flight – Space Tourism – High Speed atmospheric transportation. Contained costs, safety and reliability make a hybrid engine appreciable for suborbital launchers with human crew for private access to space.

However, despite the potential advantages of HREs, whose concept is known since the 30-40's, i.e. when solid and liquid rockets were firstly studied, they are not widely used in today's industry and, in general, the *Technology Readiness Level (TRL)* associated to hybrid rocket propulsion systems is low.
In particular, the adoption of hybrid motors for high-thrust applications has been inhibited by performance issues, mainly related to the low regression rate of conventional hybrid propellants.
Due to the slow regression rate ($\dot{r}$), i.e. the velocity at which the propellant grain recedes, a solution to generate high thrust consists in increasing the burning area (A_b) in order to obtain a sufficiently large fuel mass flow rate, as stated in Equation 1.3. This is achieved through complicated multiport fuel grain designs, as shown in Figure 1.2. However, this solution is not effective since multiport grains inherently have a low volumetric loading and, moreover, they present large unburned sliver fractions, which lower combustion efficiency, and are susceptible to chunking.
This important problematic has hindered the use of HREs in the past years despite their advantages with respect to solid and liquid engines.

$$F = \dot{m}\, v_{eff} + (p_{eff} - p_{amb})A_{eff} \tag{1.1}$$

$$\dot{m} = \dot{m}_{ox} + \dot{m}_f \tag{1.2}$$

$$\dot{m}_f = \rho_f\, \dot{r}\, A_b \tag{1.3}$$

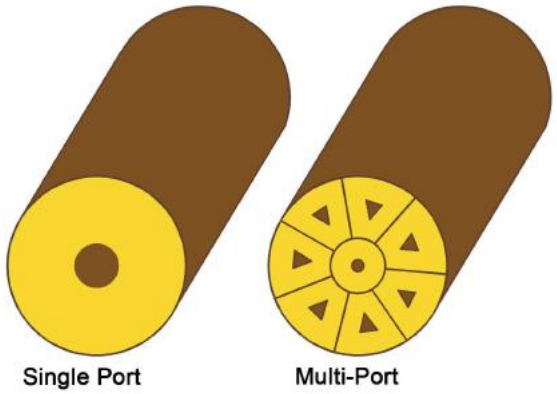

***Figure 1.2**: Single port vs multiport fuel grain design [3].*

1.1.3 New Frontiers of Hybrid Rocket Engines

Only recently, in 1997, the discovery of new classes of high regression rate hybrid rocket fuels has renewed the interest in hybrid propulsion systems.
After many series of experimental tests and analysis Karabeyoglu, Altman and Cantwell proposed a mathematical theory justifying that cryogenic fuels and normal-alkane hydrocarbons, with carbon number greater than approximately 14, show considerably higher regression rates than conventional fuels [4]. For instance, cryogenic solid n-pentane shows regression rates up to 10 times higher than polymeric hybrid fuels, while paraffin-based fuels show 3-5 times higher regression rates compared to polymers [5].

The reason behind the fast burning of these fuels is a different combustion process, experienced thanks to their low viscosity and surface tension features. As shown in Figure 1.3, a thin liquid layer, composed of melted fuel, is formed on the grain surface during combustion. The incoming oxidizer mass flow rate induces instabilities in the liquid layer, which cause liquid droplets to be detached and thus introduced in the oxidizer stream. The result is a substantial increase in the fuel regression rate since this phenomenon, called droplet entrainment, acts like a spray injection.

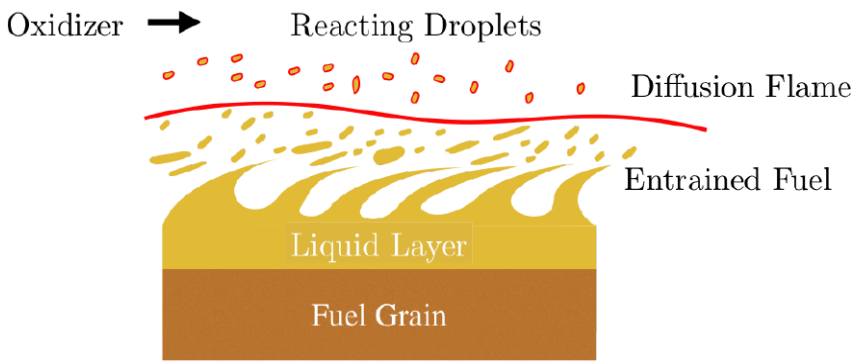

Figure 1.3: *Schematic of liquefying fuels combustion [4].*

The discovery of high regression rate fuels has revitalized the research activity on hybrids and has increased the awareness of these propulsion systems, opening the doors for large thrust hybrid rocket engines.
However, a much deeper study of hybrid propellants combustion is mandatory in order to better comprehend the complicated and challenging physical phenomena involved, with the final goal of taking full advantage of hybrid potential benefits to design safer and cheaper rockets.
With this spirit, ***MOUETTE*** (Moteur OptiqUe pour ÉTudier et Tester Ergols hybrides), a hybrid rocket engine with optical access, was designed and developed during the thesis work.

1.2 Hybrid Rocket Combustion

The aim of this Section is to analyze the internal ballistics of a hybrid rocket engine, for both classical and non-classical fuels, with particular attention to the solid fuel regression rate. The latter is indeed the key parameter influencing the design of a hybrid fuel grain and, consequently, the overall motor design.

1.2.1 Classical Fuels Combustion

The reference model for the combustion of classical fuels in hybrid rocket engines, i.e. polymeric rubbers such as HTPB, was developed by Marxman and Gilbert in the 60's [6].
After the ignition of the grain, combustion occurs in the chemically reacting boundary layer developing over the fuel surface. Since the Reynolds number associated to the oxidizer injection is typically high, the boundary layer is assumed to be turbulent. According to Marxman and Gilbert, the flame is located at approximately 10-20% of the boundary layer thickness. The heat generated by the flame is transferred to the fuel surface by convection and radiation, which causes the solid fuel to undergo pyrolysis phenomenon, i.e. the solid-to-gas phase change accompanied by a chemical change. Then, the pyrolyzed fuel vapour diffuses to the flame zone, where it mixes with the gaseous oxidizer flow, providing an ignitable mixture to the diffusion flame.
Figure 1.4 shows the theoretical schematic of a reacting boundary layer. The flame divides the boundary layer in two zones:

- the region between the fuel surface and the flame is the fuel-rich zone, composed of pyrolyzed fuel vapour and combustion products. It is characterized by concordant velocity and temperature gradients;
- the region between the flame and the boundary layer upper limit, the oxidizer-rich zone, is composed of oxidizer (in gaseous phase) and combustion products. Velocity and temperature gradients are opposite.

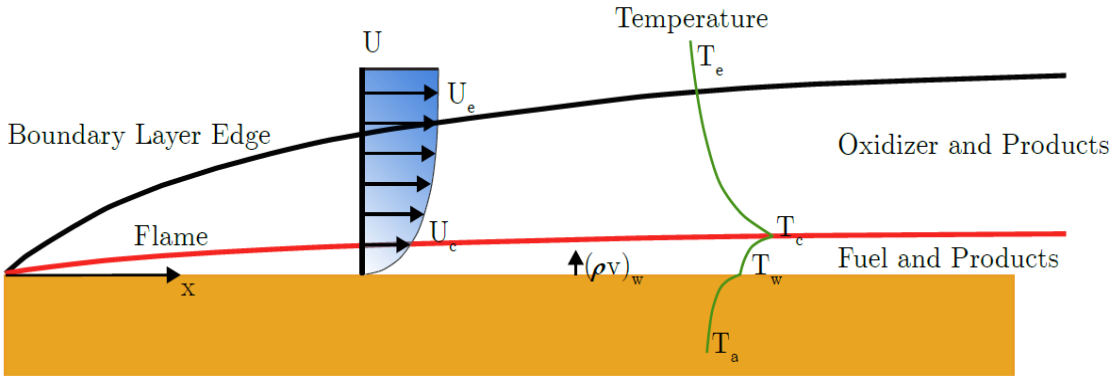

Figure 1.4: *Schematic of the diffusion flame combustion process in a turbulent reacting boundary layer [20].*

However, it is significant to underline that this description of the combustion process, characterized by two distinct regions, separated by a flame of infinitesimal thickness, is valid only from a theoretical point of view. Indeed, due to interdiffusion effects and to the finite rate of chemical reactions, the flame actually has a finite thickness and the two regions are not perfectly distinguishable.

In order to obtain a simplified regression rate expression for hybrid combustion, Marxman et al. assumed the convective heat transfer to be the controlling mechanism of the phenomenon. Indeed, in non-metallized fuel grains at pressures and flux levels of interest for propulsion applications, the heat transfer by convection is much larger than that transferred by radiation. Assuming quasi-steady conditions, the energy flux balance at the fuel surface can be written as follows:

$$\dot{Q}_c = \rho_f \, \dot{r} \, \Delta H_f \tag{1.4}$$

where $\dot{Q}_c$ is the convective heat flux (heat transfer per unit area) to the grain surface, ρ_f the fuel density, $\dot{r}$ the regression rate and ΔH_f the effective heat of gasification of the solid fuel.

By expressing Equation 1.4 in terms of different dimensionless numbers and by considering the Prandtl number to be equal to unity, indicating similar transfer of momentum and energy, the simplified regression rate expression for hybrid combustion with no radiant heat transfer can be written as:

$$\dot{r} = 0.036 \, \frac{G^{0.8}}{\rho_f} \left(\frac{\mu}{x}\right)^{0.2} B^{0.23} \tag{1.5}$$

where $G = G_{ox} + G_f$ is the total mass flux, defined as the mass flow rate divided by the cross section area, μ the combustion gas dynamic viscosity and B the blowing parameter. The complete derivation procedure of Equation 1.5 is reported in Appendix A.

The above equation indicates that the regression rate of a hybrid fuel for a non-radiative system is strongly dependent on the total mass flux and it is rather weakly dependent on axial location (x) and fuel blowing characteristics.

In practical applications, Equation 1.5 is usually replaced by a more compact form, where coefficients are obtained experimentally:

$$\dot{r} = a \, G^n \, x^m = a \left[G_{ox} + G_f(x)\right]^n x^m \tag{1.6}$$

Since the fuel mass flux (G_f) grows along x direction because of the addition of new fuel mass, the regression rate is expected to increase along the length of the grain. However, this increment is counteracted by the presence of the term x^m. Indeed, from the physical point of view, by increasing x, the boundary layer thickness increases too, therefore the flame moves away from the fuel surface, thus reducing the heat transfer to the fuel and the regression rate.

1.2.2 Blocking Effect

Unlike solid rocket motors where the flame develops directly on the fuel surface, in hybrids, due to the diffusive nature of hybrid combustion, the flame is not attached to the grain but it is located inside the reacting boundary layer. As a consequence, the energy required to vaporize the fuel is given by the heat transferred by convection and radiation from the flame region to the grain surface, with the convective heat transfer being predominant.

The reason why classical hybrid fuels exhibit low regression rate values precisely lies in a phenomenon involving the convective heat transfer, the so-called blocking effect. The diffusion of fuel mass from the solid surface to the gaseous stream, caused by fuel pyrolysis and vaporization, blocks some of the convective heat transfer to the grain, which consequently reduces the regression rate. In other words, fuel pyrolysis and vaporization, which are caused and directly proportional to the heat transfer, limit the heat transfer itself.

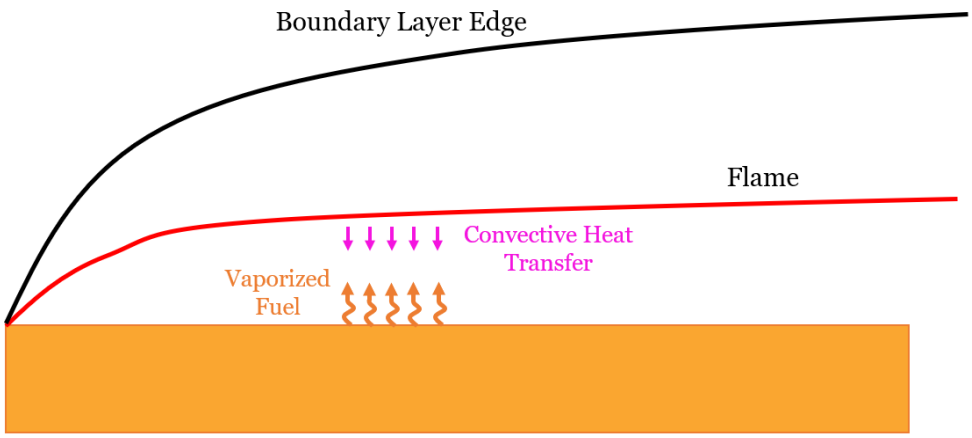

Figure 1.5: *Schematic of the blocking effect. For the sake of clarity, the boundary layer height is unrealistically increased.*

The blocking effect introduces the tendency of a self-regulating interaction between the heat flux and the mass blowing, in the sense that an increment in the fuel mass addition creates a stronger blockage of the convective heat transfer, which in turn decrease the regression rate, and vice versa.

This phenomenon is accounted in Marxman's model through the blocking factor, which is a correction of the friction and the heat transfer coefficients:

$$BF = \frac{C_f}{C_{f0}} = \frac{C_h}{C_{h0}} = f(B) \tag{1.7}$$

where C_f, C_h, C_{f0}, C_{h0} are respectively the friction and heat transfer coefficient with (no subscript) and without (subscript 0) accounting the blowing of vaporized fuel from the grain surface.
Marxman experimentally derived an expression to evaluate the blocking factor as a function of the blowing coefficient B (see Appendix A for more details). B is a non-dimensional coefficient evaluating the importance of the mass flux injected transversely in the boundary layer with respect to the axial free stream flux.

The blocking effect is nowadays the physical phenomenon limiting classical fuel hybrid propulsion technology, in particular for high-thrust applications, as any technique aimed at enhancing the regression rate by increasing the heat transfer toward the fuel grain has been found to have a limited effect [7].

1.2.3 Regression Rate Affecting Phenomena

A. Thermal Radiation Effects

For systems where radiant heat transfer to the fuel surface may be important, such as in the case of metal additive presence inside the fuel grain, the Marxman's model must be modified. In particular, a radiation heat flux must be added to the energy balance (Eq. 1.4):

$$\dot{Q}_c + \dot{Q}_r = \rho_f \dot{r} \Delta H_f \tag{1.8}$$

$$\dot{Q}_r = \sigma \epsilon_s (\epsilon_g T_f^4 - T_s^4) \tag{1.9}$$

where $\dot{Q}_r$ is the radiation heat flux from the flame to the solid grain, σ the Stefan-Boltzmann constant, ϵ_s and T_s respectively the emissivity coefficient and the temperature of the solid fuel grain, ϵ_g the combustion gas emissivity and T_f the flame temperature.
Because of the blocking effect, Marxman noted that small amounts of radiant heat transfer flux do not affect the regression rate. Indeed, thermal radiation increases the regression rate of the solid grain, but, on the other hand, the additional mass transfer into the boundary layer acts to further block the convective heat flux. Marxman et al. suggested that only strong radiation sources are likely to significantly affect regression rate [8]. The benefits of a higher heat flux to fuel thanks to the addition of radiation are damped by the blocking effect.

B. Chemical Kinetics Effects

As already discussed in Subsection 1.2.1, the hybrid diffusive combustion theory proposed by Marxman is valid under the assumption of infinitely fast chemical reactions. In particular, the Damköhler number is assumed to be elevated, meaning that chemical reactions rate is much greater than the mixing rate of reactants.

$$Da = \frac{chemical\ reactions\ rate}{mixing\ rate} = \frac{fluid\ dynamics\ characteristic\ time}{chemistry\ characteristic\ time} \quad (1.10)$$

However, this hypothesis is not always valid. For example, at high oxidizer mass flux regimes, the consequent high oxidizer velocity decreases significantly the residence time of gases in the combustion region; therefore, in these cases it is necessary to account the regression rate reduction caused by chemical kinetics.
In addition, when gas-phase reaction rates are low (slow reaction in the flame zone) a large fraction of the oxidizer gas can pass through the flame zone, reach the grain surface and start heterogeneous reactions on the fuel surface.

C. Pressure Effects

Examining Equation 1.6, it is possible note that the regression rate is not explicitly dependent on chamber pressure. This is valid for several practical applications, however, as reported in Figure 1.6, a dependency of the regression rate on chamber pressure is observed for some ranges of mass fluxes [2].
At low mass fluxes, thermal radiation becomes important because the convective heat transfer is relatively small. In this regime, for a fixed value of mass flux, a regression rate increment is achieved either by metal addition or by increasing the product of pressure and port diameter (pD), as both produce a more prominent thermal radiation.
At high mass fluxes, chemical kinetics becomes important. As consequence, since pressure influences chemical reaction rates (higher pressure means higher reaction rates), the fuel regression rate becomes itself pressure-dependent. As it is possible to observe in Figure 1.6, in this region the regression rate is smaller than theoretically predicted due to the finite rate of chemical reaction and, in addition, a pressure increment produces a higher $\dot{r}$.

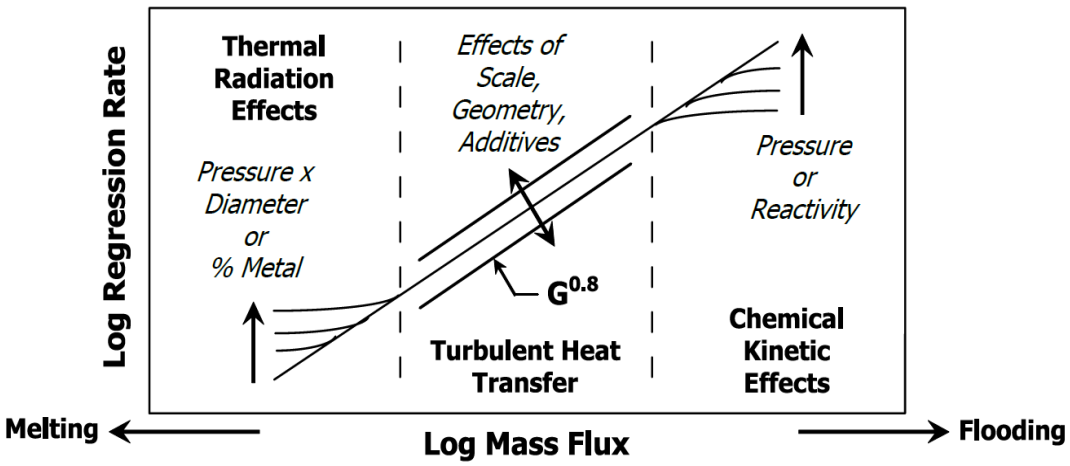

Figure 1.6: Variation of the regression rate in hybrid rockets with the total mass flux in a logarithmic plot [2].

Moreover, when the combustion chamber pressure is increased, the diffusion flame is pushed to a closer distance from the fuel surface, resulting in a greater heat transfer and higher regression rate.

The aim of Subsections 1.2.1, 1.2.2 and 1.2.3 was to show that dealing with the combustion process of a hybrid rocket engine for classical fuels is rather challenging, as several coupled phenomena must be included such as diffusion, convection, radiation, chemical kinetics and pyrolysis. For this reason, it is usual, during preliminary design phases, to formulate the regression rate expression with an even more simplified expression with respect to Equation 1.7, defined as follows:

$$\dot{r} = a\,(G_{ox})^n \tag{1.11}$$

Coefficient a and exponent n are evaluated experimentally and depend on the propellant choice and operating conditions.

1.2.4 Regression Rate Enhancing Techniques for Classical Hybrid Fuels

Classical polymeric fuels used in hybrids are known to display poor burning characteristics, leading to severe deficiencies, such as low combustion efficiency, low regression rate and low volumetric loading. This made rocket propulsion industry to refrain from seriously considering hybrid propellants as viable alternatives to liquids and solids, despite the potential enhanced safety and reduced costs benefits. For this reason, in the past years, several research activities focused their attention to improve the regression rate of hybrids. In the following, two of the most used techniques are presented: swirl injection and energetic materials' addition.

A. Swirl Injection

Several experimental research activities, such as the ones reported in References [9], [10] and [11], show regression rate improvement with the use of a swirling flow injector in comparison to traditional axial injectors.
The whole hybrid combustion process is severely affected by the oxidizer flow pattern, as it alters the flow dynamics on the grain surface. The images reported in Figure 1.7, taken from Reference [12], show the diverse flow patterns produced by a showerhead injector and a pressure-swirl injector.
The centrifugal force possessed by the swirling oxidizer flow flattens the turbulent reacting boundary layer, consequently pushing the flame to a closer distance to the fuel surface. This increases the heat transfer from the flame to the fuel grain, resulting in a higher regression rate.

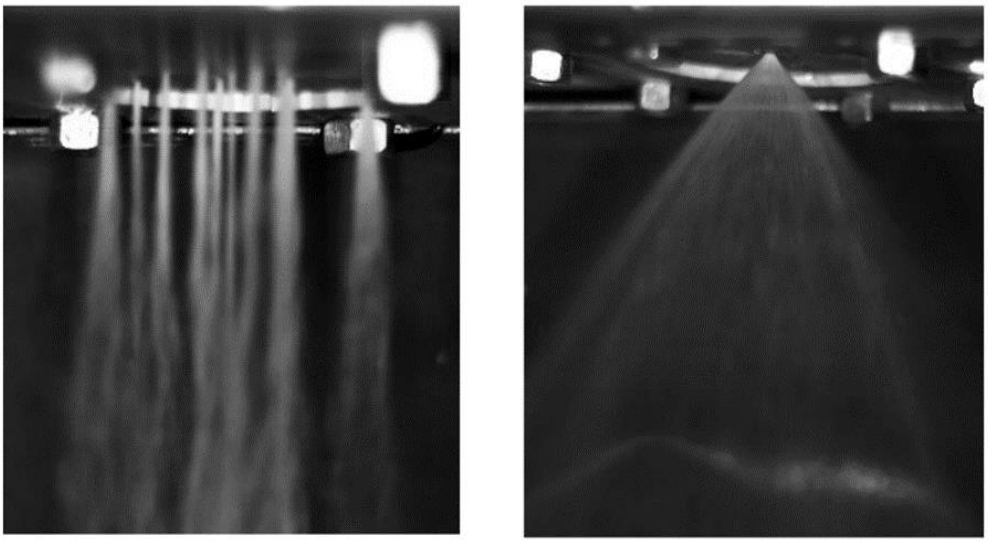

Figure 1.7: *Water discharged at 30 bar from a showerhead injector (a) and a pressure-swirl injector (b) [12].*

B. Energetic Additives

The performance enhancement of classical hybrid propulsion systems via the addition of energetic material can be achieved in different ways [13]:

1. addition of energetic particles into the solid fuel grain, mainly metal powders;
2. addition of oxidizing material particles into the solid fuel grain, e.g. ammonium perchlorate (AP) or potassium nitrate;
3. replacement of the inert HTPB with more energetic polymers, e.g. glycidyl azide polymer (GAP);
4. replacement of conventional liquid oxidizer, as liquid oxygen or nitrous oxide, with more energetic and denser ones, such as hydroxyl ammonium perchlorate (HAP) or hydroxyl ammonium nitrate (HAN).

However, adding oxidizer in the fuel grain or using more energetic fuels and oxidizers is not attractive, since the consequence is losing the desired safety operations properties of a hybrid rocket motor. Therefore, the most used technique consists in the addition of metal particles in the fuel grain.
Metals possess highly desirable combustion properties, which make them well suited for this application. First of all, thanks to their high heat of combustion, the inclusion of metal particles in solid fuels provides a higher energy release, corresponding to increased flame temperature, specific impulse and regression rate. Moreover, the introduction of metals can improve the physical properties of the grain, for example increasing its density.

1.2.5 Non-Classical Liquefying Fuels Combustion

In 2001, Karabeyoglu, Altman and Cantwell, researchers at Stanford University, proposed that an effective method to increase the regression rate in hybrids is to use the so-called liquefying fuels. Thanks to their low viscosity and low surface tension properties, these fuels form a melt layer on the grain surface during burning, resulting in a different combustion mechanism with respect to classical hybrid fuels.
Under typical operating conditions of hybrid motors, the shear forces between the liquid layer and the oxidizer flow induce instabilities in the liquid layer itself: roll waves are produced and fuel droplets are forced to detach and then to entrain into the flow (Figure 1.8).
As result, the entrainment of fuel droplets acts like a spray injection along the length of the combustion chamber, increasing the effective burning area and reducing the blocking effect. The mass transfer of liquid fuel droplets from the grain surface to the flame region sums to the classical fuel vaporization, resulting in a substantial increase of the regression rate. As a consequence, simple single-port fuel grain configurations result sufficient to generate high thrust values, making hybrid propulsion systems competitive candidates for launch systems and in-space missions.

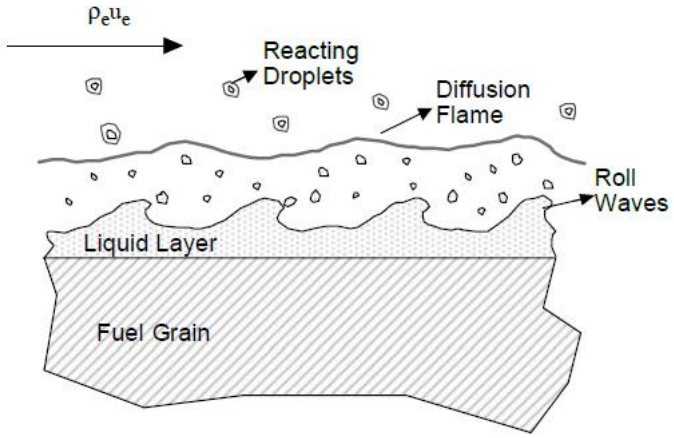

Figure 1.8: *Schematic of the entrainment phenomenon proposed by Karabeyoglu et al.*

In the light of experimental findings and liquefying fuel theory predictions, the following empirical expression for the entrainment rate of liquid fuel droplets in term of the relevant properties of the hybrid motor was suggested [4]:

$$\dot{m}_{ent} \propto \frac{p_D^{\alpha}\, h^{\beta}}{\mu_L^{\gamma}\, \sigma^{\pi}} \tag{1.12}$$

where:

- p_D is the dynamic pressure;
- h is the liquid layer thickness;
- μ_L is the liquid layer viscosity;

- σ is the liquid layer surface tension;
- $\alpha, \beta, \gamma, \pi$ are experimental parameters.

This relation clearly shows that the entrainment phenomenon is favored by low values of viscosity and surface tension of the liquid melt layer.

The main fuel classes showing a melt layer during combustion are cryogenic fuels and normal alkanes.

A. Cryogenic Solid Fuels

The first fuels discovered to show higher regression rate values compared to classical polymeric fuels were cryogenic solid fuels. During the 90's, several research groups at U.S. Air Force Research Laboratory (AFRL) [14, 15] and ORBITEC [16, 17] began investigating cryogenic hybrid propellants with the initial motivation to develop a method to stabilize and combust high-energy density matter.
Hot fire tests demonstrated that cryogenic solid hydrocarbons such as solid pentane, solid ethylene and solid RP-1, regressed from 2 to 10 times faster than HTPB operating at the same conditions.

Although the cryogenic hybrid concept may appear appetible due to the high performance, comparable to liquid bipropellant engines, the safety and operational advantages of hybrid propulsion are basically lost. As a matter of fact, the use of cryogenic fuels adds significant complications in the engine design and in the manufacturing, transport and storage processes of the fuel.

B. Paraffin-Based Solid Fuels

The above-mentioned cryogenic solid fuels investigations did not provide any model or theory to explain the resulting high regression rates. However, the authors indicated that the energy required to gasify a unit of mass of fuel is much smaller for cryogenic solids with respect to conventional solid fuels, by a factor of around 10-20.
During the development of the liquefying fuels theory, Karabeyoglu et al. assumed that the very high regression rates of cryogenic solid fuels cannot be explained simply because of a lower heat of vaporization [4]. Indeed, in the regression rate expression according to Maxman's theory, the heat of vaporization is incorporated in the blowing parameter B, raised to a power 0.32 (see Equation 1.5 and Appendix A). Thus, even a significant reduction of the heat of vaporization would only cause modest increase in the regression rate (up to 30-50%), not in agreement with the observed increases of more than 300%.
For this reason, Karabeyouglu et al. postulated the existence of an additional mass transfer mechanism, involving the entrainment of liquid fuel droplets from the surface melt layer, to be responsible for the very high regression rates observed during cryogenic solid fuels firing tests.

Even though the liquefying fuels combustion theory was first developed to explain the behavior of solid cryogenic propellants, it is appliable to any material that would form a liquid layer on its burning surface [4]. Particular interest was given to materials having this property while being solid at standard conditions.
The theory was applied to the homologous series of n-alkanes (C_nH_{2n+2}) and results indicated paraffin and polyethylene waxes, having an intermediate range of carbon numbers in the range 16 to 50, to be non-cryogenic materials generating high rates of entrainment of liquid droplets into the gas stream [5].
Moreover, as shown in the comparison reported in Figure 1.9, it was surprisingly noted that the regression rate of paraffin wax is comparable to that of the lower molecular weight cryogenic pentane.

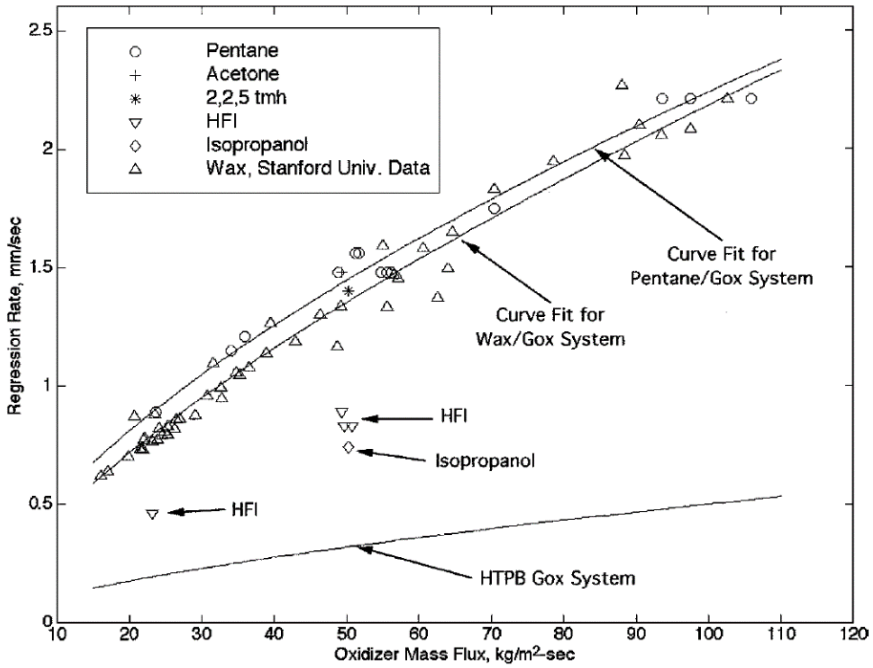

Figure 1.9: *Space-time-averaged regression rate vs. average oxidizer mass flux for various liquefying materials and HTPB [5].*

Since, for normal alkanes, a higher number of carbon atoms increases the molecular weight and the viscosity, one may think that the regression rate of paraffin wax should be rather lower than pentane. However, a higher carbon number increases the melting point too, thus reducing the viscosity of the liquid melt layer. The same is valid for surface tension.
The overall result is that, for paraffin waxes, viscosity and surface tension increments due to the higher molecular weight are overcome by their decrease due to a higher melting temperature.
Low viscosity and surface tension favor the instability of the melt layer, promoting the release of fuel droplet and thus enhancing the entrainment phenomenon [18].

As reported in Table 1.2, viscosity and surface tension values are similar for pentane and paraffin wax, which explains why their regression rates are comparable.

Propellant	Pentane C_5H_{12}	Paraffin Wax
Molecular weight [g/mol]	72.15	432.8
Viscosity [mPa·s]	0.46	0.65
Surface tension [mN/m]	14.3	7.1
Liquid phase density [kg/m^3]	688.4	654.4
Melting temperature [K]	143.3	339.6
Boiling temperature [K]	309.6	727.4
Heat of fusion [kJ/kg]	116.7	167.2
Heat of vaporization [kJ/kg]	357.8	163.5

Table 1.2: *Pentane and paraffin wax properties. Liquid properties other than surface tension are evaluated at a mean temperature between melting and vaporization temperatures. Surface tension is evaluated at boiling temperature [5].*

More recent studies have shown the combustion process of paraffin-based fuel to be significantly pressure-dependent.
While, at atmospheric pressure, unsteady roll waves and droplet entrainment, as explained previously in this subsection, are the main phenomena that characterize paraffin burning, the combustion process is rather different at elevated pressures. Chandler et al. [19] and Jens et al. [20] experimental activities observed the nature of combustion to dramatically change with growing pressure. Increasing pressure starting from ambient conditions, the liquid melt layer presents filament-like structures and upward bursts, resulting in a greater number of entrained droplets. At pressures above paraffin critical pressure, which is around 6.7 bar, filament structures become less important, while numerous intense blowing events are observed.

The results of the liquefying fuels theory show that paraffin-based materials are the class of non-cryogenic fuels having the best properties among hybrid rocket fuels. Since, in addition, paraffin waxes are commercial, available, low-cost and easy to manufacture materials, paraffin-based fuels are the perfect candidates for hybrid fuels, enabling high-thrust application thanks to the high regression rate and keeping the enhanced safety and reduced costs benefits of hybrid propulsion.

1.2.6 Generalized Hybrid Combustion Theory

By modifying Marxman's classical hybrid combustion theory, it is possible to obtain a generalized theory that can be applied to liquefying high regression rate fuels too. Karabeyoglu et al. proposed three major modifications.

1. The detachment of fuel droplets from the liquid melt layer reduces the effective heat of vaporization. For the same mass of fuel leaving the grain surface and entering in the flow, less energy is required for fuel evaporation as a significant portion of fuel directly detaches from the melt layer in the form of droplets.
2. The blocking factor $C_f/C_{f0} = C_h/C_{h0}$ (Equation 1.7) is altered due to the two-phase flow regime.
3. The fuel surface roughness and the heat transfer from the flame front to the fuel grain are increased as a result of the roll waves and ripples in the liquid layer.

Finally, the regression rate of a hybrid fuel can be written as the sum of two terms:

$$\dot{r} = \dot{r}_{vap} + \dot{r}_{ent} \tag{1.13}$$

In this expression, $\dot{r}_{vap}$ corresponds to the evaporation regression rate, i.e. the fuel entering into the gas stream because of the vaporization occurring in the liquid melt layer over the grain surface. $\dot{r}_{ent}$, instead, is the entrainment regression rate, related to the transfer of fuel droplets into the flow due to the unstable melt layer interaction with the oxidizer stream.
It is however significant to note that, for non-classical liquefying hybrid fuels as well as for classical polymeric ones, during preliminary design and experimental phases, it is generally accepted to use the most simplified regression rate expression reported in Equation 1.11 ($\dot{r} = a\,(G_{ox})^n$).

2. Hybrid Rocket Visualization Experiments

2.1 Motivation

The combustion process within a hybrid rocket engine is extremely complex and not completely understood. The main reason is that it involves several phenomena which are deeply coupled between each other. The flame develops in a turbulent reacting boundary layer at a certain distance from the fuel grain. The heat transferred from the diffusive flame region to the fuel surface by thermal convection and radiation, causes the fuel to degrade, soften and then pyrolyze. Fuel vapors are transported, via convection and diffusion, to the flame region, where they mix and react with the oxidizer stream. In addition to fluid dynamics, chemical kinetics plays a major role too, due to its influence on reactions development. Chemical kinetics modeling is particularly challenging, as it requires the knowledge of pyrolysis products as well as reaction rate constants for the reactions involved in the combustion mechanism.
The complexity of the hybrid combustion process is further increased if liquefying fuels, instead of classical polymerics fuels, are considered. In this case, a liquid melt layer forms on the grain surface during burning and becomes unstable due to the action of the gas flow. Liquid fuel droplets detach from the melt layer, being entrained by the gas stream, and then participate to combustion.
As result, the purely theoretical modeling of hybrid combustion is very challenging. As a matter of fact, the current theory presented in Section 1.2 is not able to accurately predict the regression rate of a hybrid rocket fuel without the support of experimental data from a rigorous test campaign for the desired propellant combination.

As well as theoretical modeling, numerical activities to simulate the combustion of a hybrid rocket engine are rather complicated and thus not very frequent. The reason lies again in the vast amount of coupled physical phenomena involved in the combustion process. Computational fluid dynamics studies are even less frequent for liquefying fuels, since the formation of a liquid melt layer on the grain surface and the entrainment phenomenon impose to introduce the dynamics of the liquid phase and to model its instability mechanism. Although, in the past, several CFD models accounting for the interaction between a high-speed gaseous flow and liquid droplets

have been developed, a complete description of the transition process from an unstable free surface to dispersed droplets appears to be well beyond actual CFD solver capabilities [7].

On the other hand, experimental investigation of hybrid rocket combustion at realistic operating conditions is also challenging. The chamber pressure is usually greater than 13 bars for typical hybrid rocket motors, while the temperature at the flame location is often greater than 3000 K. High temperatures combined with elevated pressures make in-situ diagnostics nearly impossible.

Since both theoretical modelling and in-situ experimental investigation show some intrinsic difficulties, combustion visualization experiments provide a solution to analyze and study the burning process characterizing a hybrid rocket engine within the turbulent boundary layer.
Optical investigations are a viable tool to better understand the combustion phenomenon and, therefore, be able to accurately model it, in order to eventually improve the design of HREs.

2.2 Previous Work and State of the Art

The study of hybrid rocket motor combustion process with visualization experiments is not novel. Marxman and colleagues [8] developed the hybrid combustion theory on the basis of shadowgraph and schlieren images collected by Muzzy, who used a slab motor burning polymethyl methacrylate (PMMA), a transparent thermoplastic, and gaseous oxygen [21]. During the 90's, hybrid rocket visualization facilities were built at JPL [22] and at Pennsylvania State University [23] in order to investigate respectively the combustion of HTPB fuel grains embedded with coal and aluminum particles, and the regression rates and heat transfer phenomena of HTPB fuel with gaseous oxygen (GOX).

The discovery of liquefying hybrid fuels revitalized the interest in optical investigations, with the particular goal of capturing the entrainment process. In 2011, Nakagawa et al. from Tokai University published the first high-speed images of the combustion of paraffin-wax fuel grains with GOX at atmospheric pressure [24]. In addition, the regression rate dependence on the fuel viscosity was investigated. Pictures of the combustion chamber set-up and of the burning fuel are reported respectively in Figure 2.1 and 2.2. The low pressure and low oxidizer mass fluxes made relatively easy to detects fuel droplets, but were quite far from actual hybrid rocket operating conditions.

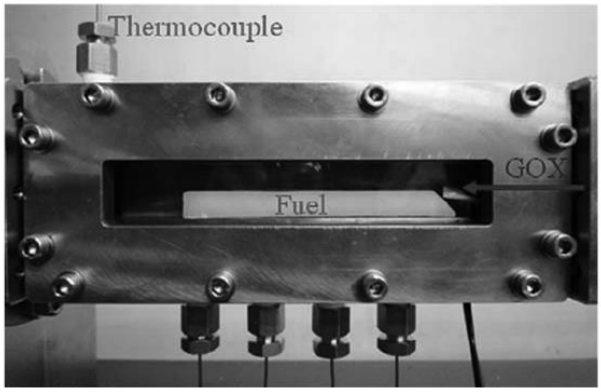

Figure 2.1: *Combustion chamber set-up at Tokai University*

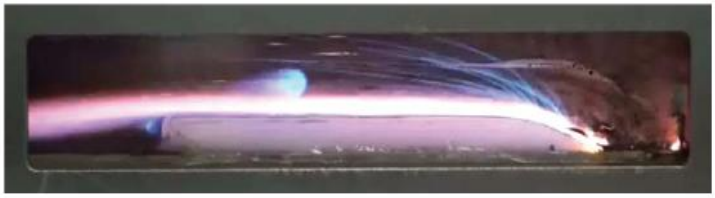

Figure 2.2: *Combustion visualization of paraffin-wax FT-105 produced by Nippon Serio, having (on average) 51 carbon and 104 hydrogen atoms [24].*

In 2012, Chandler et al. at Stanford University designed a combustion visualization facility to study the combustion of paraffin-based fuels with GOX, using high-speed videos [21]. Results showed unsteady roll waves in the melt layer and droplet entrainment at atmospheric pressures (Figure 2.3), with mass fluxes between 25 and 32 kg/m^{2}s. The first non-atmospheric pressure tests were performed too [19], revealing filament-like structures in the melt layer and upward bursts (Figure 2.4). However, because of polycarbonate windows cracking, only short burns at non-atmospheric pressure were allowed.

Figure 2.3: *Progression of a roll wave in the liquid layer during an atmospheric pressure test [19]. (Oxygen flows from left to right)*

In addition, Chandler et al. also tested conventional hybrid fuels to verify the predictions of liquefying fuels theory. Tests confirmed that high-density polyethylene (HDPE) forms a stable melt layer without any significant droplet entrainment due to its high viscosity, and that HTPB burns with no liquid melt layer on its surface.

Figure 2.4: *Filament-like structures in the combustion of blackened paraffin at non-atmospheric, subcritical, pressures [19].* (Oxygen flows from left to right)

Afterwards, Jens et al. modified Stanford University combustion facility in order to accommodate schlieren imaging instrumentation and to gain high-pressure test capability. The combustion of paraffin-based fuels was analyzed with high-speed, schlieren and OH* chemiluminescence images. The first visualizations of paraffin-wax and GOX combustion at super-critical pressures were obtained (paraffin critical pressure is around 6.7 bar) and showed that, at these conditions, the fuel melt layer is dominated by numerous intense blowing events, instead of filament-like structures [20]. Nevertheless, a radical change in the nature of combustion when chamber pressure overcomes paraffin super-critical pressure was not found. Tests conducted by Jens et al. revealed intermittent blowing events to be present starting from 2.7 bar. As chamber pressure was increased up to almost 12 bar, the time between these events appeared to decrease, while the ejection of droplets became more violent. The high-speed and schlieren images of paraffin combustion at elevated pressure published by Jens et al. are reported in Figure 2.5, 2.6 and 2.7.

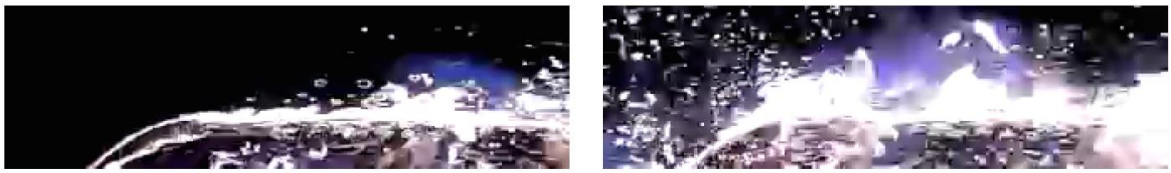

Figure 2.5: *High-speed images of paraffin combustion at 4.9 bar. Nominal combustion (left) and blowing event (right) [20]. (Oxygen flows from left to right)*

Figure 2.6: *High-speed images of paraffin combustion at 7.1 bar. Nominal combustion (left) and blowing event (right) [20]. (Oxygen flows from left to right)*

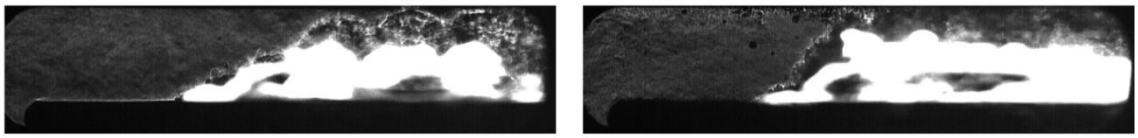

Figure 2.7: *Schlieren images of paraffin combustion at 4.9 bar (left) and 7.1 bar (right) [20]. (Oxygen flows from left to right)*

Starting from 2013, optical investigations of paraffin-based hybrid rocket fuels were conducted at the German Aerospace Center (DLR). Kobald et al. presented high-speed and schlieren images of paraffin-wax and GOX, at atmospheric pressure, showing periodic wave-like structures in the liquid melt layer [26]. The role of fuel viscosity in the melt layer instability was analyzed too. Later on, in 2015, decomposition techniques (proper orthogonal decomposition) were applied to high-speed videos data to capture the main structures characterizing the flow field and the combustion flame and, then, to compare experimental results with the well-known Kelvin-Helmholtz instability theory [27]. Petrarolo et al. continued similar investigations to study the instabilities of the liquid melt layer. Atmospheric pressure tests allowed to relate the frequency of wave-like structures to both viscosity and oxidizer mass flux: the higher the viscosity, the lower the frequency and the longer the waves, resulting in a more stable liquid layer, while increasing the oxidizer mass flux the liquid layer becomes more unstable [28].

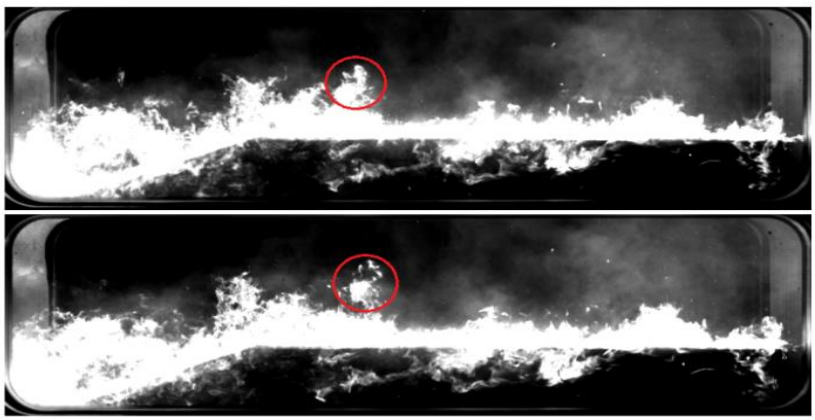

Figure 2.8: *High-speed images of paraffin combustion at 40 bar [29]. (Oxygen flows from left to right)*

Lately, in 2018, after updating the DLR optical visualization facility to run elevated pressure tests up to 50 bar, Petrarolo et al. presented a comparison between the combustion of paraffin-based fuels at sub-critical and super-critical pressures [29]. While a periodic wave-like behavior connected to Kelvin-Helmholtz instability was recognized in atmospheric tests, no periodicity was found at elevated pressures, with the combustion process characterized by flame bursting and blowing events (Figure 2.8). As result, the regression rate of paraffin-based fuel was found to be greatly affected by chamber pressure: the higher the pressure, the faster the fuel burns.

Recently, experimental activities on liquefying hybrid fuels were conducted by Paravan et al. at Space Propulsion Laboratory (SPLab) of Politecnico di Milano. Investigations involved both cold-flow tests to study the entrainment phenomenon in a dedicated experimental setup and burning tests at ambient conditions in a lab-scale motor to evaluate the regression rate. Cold tests allowed to visualize with high-speed video the droplets entrainment without combustion and, in addition, to analyze the average size of entrained droplets for different paraffin-based fuel formulations [30].

2.3 Objective of the Thesis Work

The presented optical experimental investigations open the following scenario for liquefying hybrid rocket fuels. First of all, experiments confirmed the entrainment of droplets to be responsible for the high regression rates showed by liquefying fuels, as it acts like a spray injection along the grain length that sums to the conventional fuel vaporization. Moreover, optical visualizations revealed the entrainment phenomenon to be the direct consequence of the liquid melt layer instability, which was found to be strongly affected by fuel viscosity and oxidizer mass flux. These results translate into a significant achievement reached by experimental optical investigations. As a matter of fact, they provide a verified way to properly select the fuel viscosity and the oxidizer mass flux to achieve the desired regression rate. This, together with the intrinsically high regression rate values of liquefying hybrid fuels, enables to design single-port fuel grain configurations for high-thrust applications.
However, HREs are not widespread in the current space industry with a technological maturity still between a university level of research and development and an industrial business level.
The major issue is that the interdependencies between the several coupled physical phenomena characterizing hybrid propulsion have yet to be fully clarified, with particular reference to realistic operative conditions of HREs. Especially, the presented rather detailed understanding of hybrid rocket combustion involving solid fuels liquefaction is limited to atmospheric pressure conditions only [7]. Instead, in order to accurately design a hybrid rocket engine, it is required an extensive knowledge of the combustion process at realistic operating conditions, which usually feature a pressure

well above 10 bar. Although tests of paraffin-based fuel at super-critical pressures have been performed by Jens et al. and Petrarolo et al., showing how the nature of the combustion phenomenon changes with increased pressure, a systematic analysis with variable fuel viscosity and oxidizer mass flux is still missing.

Within this framework, my Master's Degree thesis in Aeronautical Engineering at *Politecnico di Milano*, carried out in collaboration with the Aéro-Thermo-Mécanique Department of *Université Libre de Bruxelles*, has involved the design, development and commissioning of a laboratory hybrid rocket engine with optical access, capable of performing both low and high-pressure combustion tests of hybrid rocket fuels. The major objective of ***MOUETTE*** (**Moteur OptiqUe pour ÉTudier et Tester Ergols hybrides**) is to provide an experimental setup enabling a better comprehension and characterization of the combustion process of hybrid fuels in a broad range of operative conditions, with a particular interest to elevated pressures. With reference to paraffin-based fuels, the main choice, on which the engine design was developed, was the selection of 15 bar as maximum chamber pressure. In fact, although hybrid engines operate at even higher pressures, beyond the critical pressure of paraffin, which is about 7 bar, the physics of the combustion process is expected to remain unchanged. Therefore, a maximum chamber pressure of 15 bar ensures the capability of studying the combustion process of HREs at realistic operating conditions.
Real-time data of the hybrid rockets internal ballistics will empower an exhaustive characterization of the phenomenon, as well as support the improvement of numerical models for CFD simulations, with the ultimate mission of contributing to make hybrid propulsion a competitive candidate for the next generation of launch systems and in-space missions, taking full advantage of its enhanced safety and low-cost benefits.

3. Design of a Hybrid Rocket Engine with Optical Access

The purpose of this chapter is to provide a comprehensive presentation of *MOUETTE* project, explaining and motivating each design choice. A detailed list of the engine's components is provided in Appendix B.

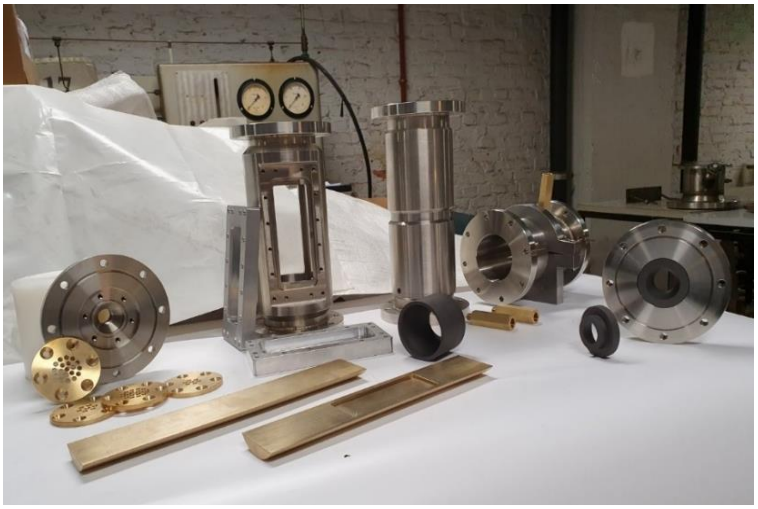

Figure 3.1: *Overview picture of some engine's components.*

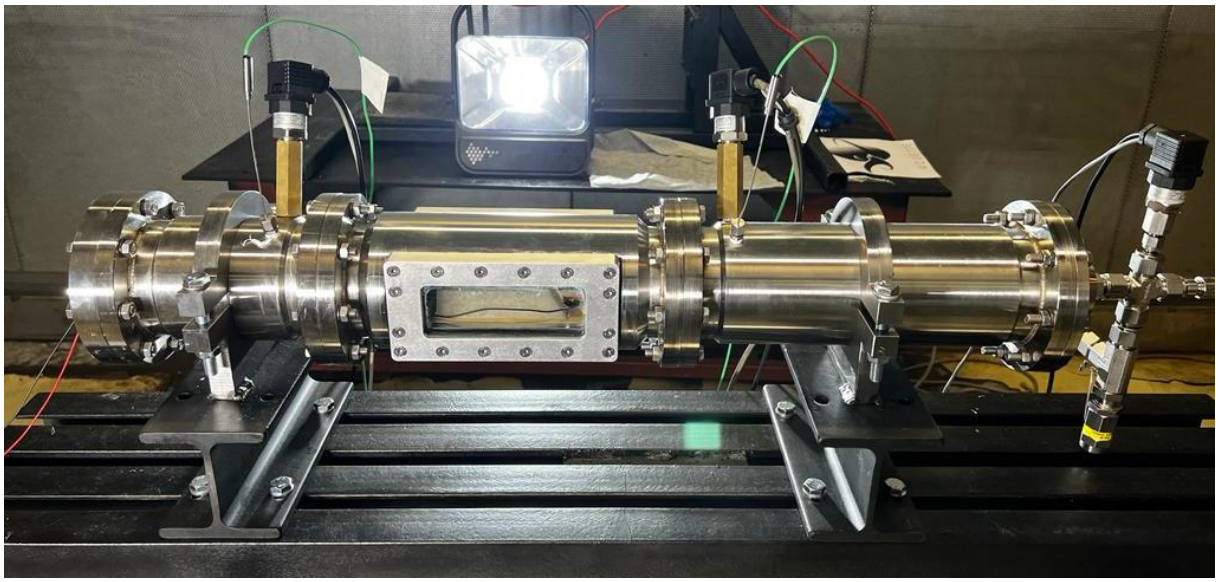

Figure 3.2: *Picture of MOUETTE engine.*

3.1 Requirements and Applications

MOUETTE was designed with the goal of providing an experimental setup capable of analyzing the combustion process and the internal ballistics of hybrid rocket fuels via optical visualization, in a broad range of operating conditions.
As a first step, the engine requirements have been identified, in order to begin the design phase on the correct path. The main *MOUETTE* requirements are listed in the following:

1. Optical accessibility, i.e. the capability of visualizing, in a proper manner, the combustion process of hybrid fuels from the exterior.
2. Nominal operating conditions: chamber pressure ranging from atmospheric levels up to 15 bar.
3. Engine dimensions compatible to a slab burner with optical access previously developed by *Université Libre de Bruxelles (ULB)* and *Royal Military Academy of Belgium (RMA)*, having end flanges of 150 mm diameter with 8 holes for M8 bolts located on a circumference of 130 mm diameter.

In addition, since *MOUETTE* is a laboratory engine, i.e. designed for scientific research, it was essential to define from the beginning the type of experimental investigations that are planned to be performed in the future. At the time of writing this thesis, the following research activities at *Université Libre de Bruxelles* will be based on experimental tests with *MOUETTE*:

- Characterization of liquefying fuels (such as paraffin) combustion process at different chamber pressures.
- Analysis of the effects of the grain geometry on the internal ballistics of hybrid fuels.
- Analysis of the effect of additives on the internal ballistics of hybrid fuels.
- Analysis of the effect of fuel manufacturing procedures on the internal ballistics of hybrid fuels.

Furthermore, it is significant to point out that a modular design was adopted. The engine is composed by multiples parts (modules) that can be assembled, disassembled and replaced to grant an easy and fast manual access to the engine interior.

3.2 Oxidizer Selection

The two main oxidizer that have been considered for *MOUETTE* are gaseous oxygen (GOX) and liquid nitrous oxide (N_2O). Other oxidizers such as liquid oxygen (LOX) and hydrogen peroxide (H_2O_2) were not considered due to the complex handling of these propellants.

It is also relevant to consider that, since *MOUETTE* experimental activities concern internal fuel ballistic only, the specific impulse and other engine performance were not taken into special account during the oxidizer choice.

From a chemical perspective, there is no difference in the oxidation phenomenon using nitrous oxide over oxygen. Indeed, once N_2O dissociation occurs ($N_2O \rightarrow N_2 + O$ [31]), oxygen is the true oxidizer agent, while nitrogen behaves like the inert species it is.
The main advantages of using N_2O, such as a lower tank size per unit mass with respect to gaseous oxidizers due to its liquid state and its self-pressurizing property, are not particularly significant for *MOUETTE* applications.
Since GOX allows to obtain much clearer and "cleaner" visualization of the combustion phenomenon with respect to liquid oxidizers, such as N_2O, it was selected as oxidizer.

The oxygen mass flow rate was defined to range between 50 g/s and 100 g/s to have an oxidizer mass flux (G_{ox}) similar to the values reported in literature for optical visualization facilities.

3.3 Metal Components

A CAD model overview of *MOUETTE* metal parts is shown in Figure 3.3.
From left to right, the engine consists of the following components:

1. Injector Head
2. Pre-Chamber
3. Main-Chamber
4. Window Frame
5. Post-Chamber
6. Injector Plate
7. Pre-Chamber Insert
8. Grain Holder
9. Nozzle Plate

The metals used for the construction of the components in contact with the oxidizer flow are stainless steel AISI 304L and brass, both compatible with gaseous oxygen, while the Window Frame is built in aluminum.
Stainless steel was chosen as the material for structural components due to its excellent mechanical properties and its superior corrosion resistance at atmospheric and elevated temperatures, consequence of the chromium addition [32]. Brass was selected for the components in contact with the high temperature flow but with no structural task.

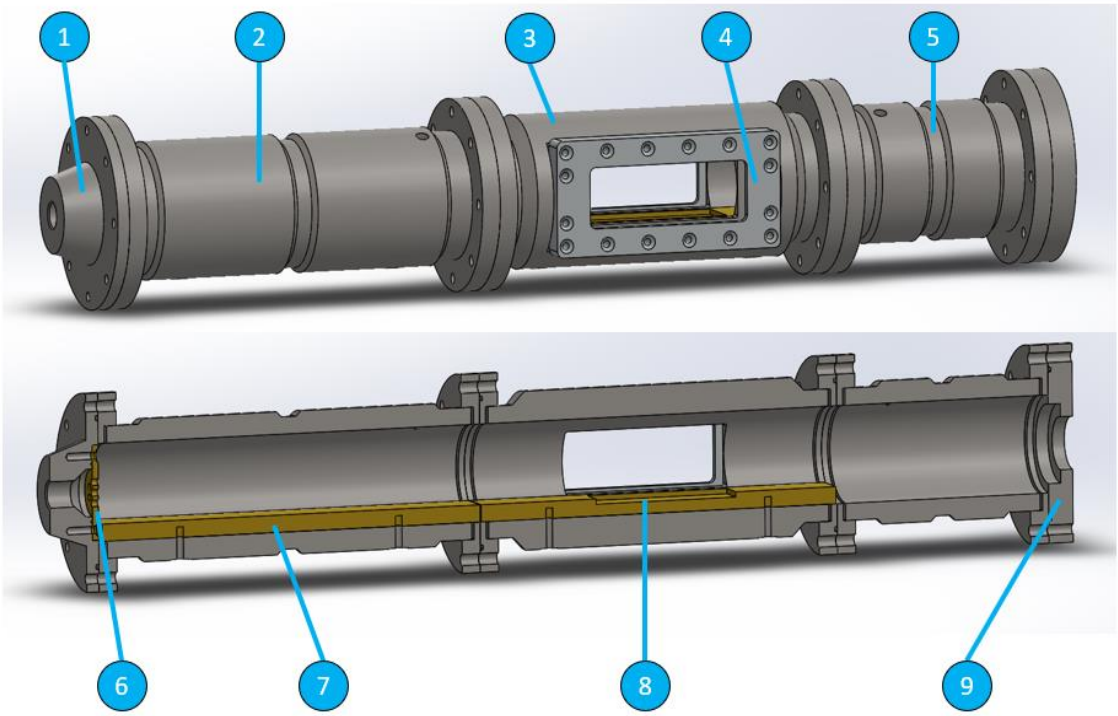

Figure 3.3: *Overview of the metal components of MOUETTE.*

The two grades of stainless steel that were considered are AISI 304L and AISI 316. Thanks to the nickel content characterizing the chromium-nickel 300 series [32], both AISI 304L (nickel content 8-12%) and AISI 316 (nickel content 10-14%) have austenitic microstructures, resulting in the following favorable properties for *MOUETTE* application:

- Excellent corrosion resistance;
- Good performance at both low and high temperatures;
- Excellent weldability.

Since AISI 316 is the choice for salty or acidic environment use, which is not the *MOUETTE* case, and its cost is about 25% higher than AISI 304L, the latter was selected. Moreover, AISI 304L (maximum carbon content: 0.03%) was picked over AISI 304 (maximum carbon content: 0.08%) because the lower carbon content helps minimize/eliminate carbide precipitation during the welding process, allowing the 304L alloy to be used in a welded state even in severe corrosive environments. Welding, indeed, was a fundamental procedure of *MOUETTE* manufacturing, as the flanges were welded onto the tubular part of chambers (more details in Subsection 3.3.2).

3.3.1 Combustion Main-Chamber, Pre-Chamber and Post-Chamber

The fundamental modules of *MOUETTE*'s modular structure are the Main-Chamber, the Pre-Chamber and the Post-Chamber, all built in stainless steel AISI 304L.

The first and most important design choice, which directly influenced the chambers, was the definition of the engine cross section, selecting between a square and a circular shape.
The decision was driven by the requirements of optical accessibility and elevated pressure tests capability. In particular, although a square combustion chamber shape allows for a much easier design of a window, i.e. the opening to view the combustion phenomenon from the outside of the engine, a square cross section is not well suited to support the stresses generated by the elevated chamber pressures. A circular cross section was thus selected.
In addition, it is significant to point out that the choice of a circular cross section, as opposed to a square one, has some important advantages with regard to the manufacturing procedure. Indeed, circular stainless steel tubes (low thickness) or hollow bars (high thickness) are commercial, widespread and, moreover, easily machinable on the lathe to obtain the desired dimensions. On the other hand, square tubes are not so diffused and are only available in small thicknesses.

Therefore, the decision was to design the chambers so that they could be manufactured from commercial stainless steel hollow bars, which are indeed capable of withstanding extremely high internal pressures. Please refer to Appendix C for a detailed analysis of stress distribution in thick cylindrical tubes.

A picture of hollow bars during manufacturing process of *MOUETTE* is shown in Figure 3.4.

Figure 3.4: *AISI 304L hollow bars during manufacturing.*

Main-Chamber

The Main-Chamber is *MOUETTE*'s most peculiar component as well as the engine's core, i.e. where combustion takes place. It features two side windows so that the combustion process of the hybrid fuel sample can be visualized from the outside.

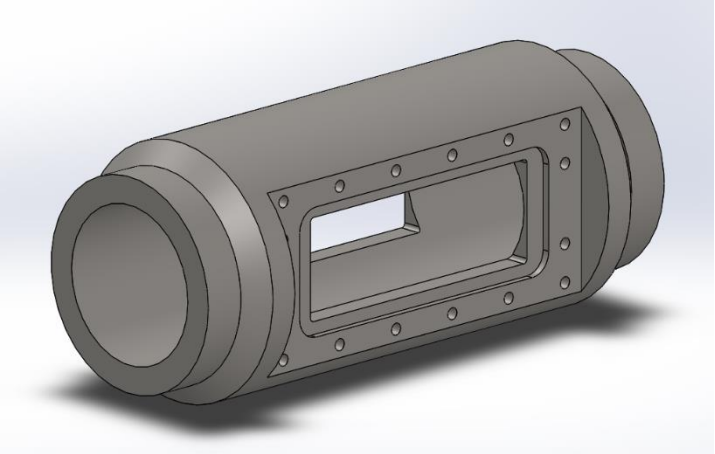

Figure 3.5: *CAD visualization of the Main-Chamber.*

It was chosen to have two optical accesses to the chamber in order to have the possibility to use both OH*/CH* chemiluminescence and schlieren visualization techniques, which need one and two windows, respectively.

The Main-Chamber is built starting from a hollow bar with a 74 mm inner diameter (ID) and a 120 mm outer diameter (OD), thus having a 23 mm thickness. Although even a much smaller wall thickness would be enough to withstand the maximum chamber pressure of 15 bar (see Appendix C), a high thickness has been adopted to directly machine the window slots inside it. As it possible to observe in Figure 3.5, the sides of the Main-Chamber are indeed machined in order to accommodate the Glass and the Window Frame. The coupling between the Main-Chamber, Glass and Window Frame is explained in detail in Subsection 3.3.3 and in Section 3.4.

The Main-Chamber is 280 mm long, while the lateral openings for optical access have a 133 x 48 mm size.

Pre-Chamber

The Pre-Chamber, built starting from a hollow bar with a 74 mm ID and a 108 mm OD, is the component located between the Injector Head and the Main-Chamber and its function is to provide the Main-Chamber with the most uniform and laminar oxidizer flow possible. First of all, a laminar oxidizer flow is desired to clearly visualize the combustion process. Furthermore, since the purpose of future experimental activities with *MOUETTE* is to analyze the effect of different grain geometries and additives on the level of turbulence that characterizes the turbulent reacting boundary layer where combustion takes place, a uniform, laminar oxygen flow is desired to visualize only

the effective results. Since, after the injection through the Injection Plate, the oxygen flow entering the Pre-chamber is characterized by recirculation zones, the Pre-chamber must be long enough to allow the flow reattachment before it reaches the Main-chamber.

To evaluate the Pre-chamber length properly suited to ensure a full oxidizer flow reattachment, a CFD simulation with *Ansys Fluent* was performed. The worst-case scenario for flow separation was chosen, i.e., the condition in which the oxidizer flow velocity exiting the Injection Plate is maximum. Therefore, the simulation was implemented with the maximum oxygen mass flow rate (100 g/s) and atmospheric chamber pressure.

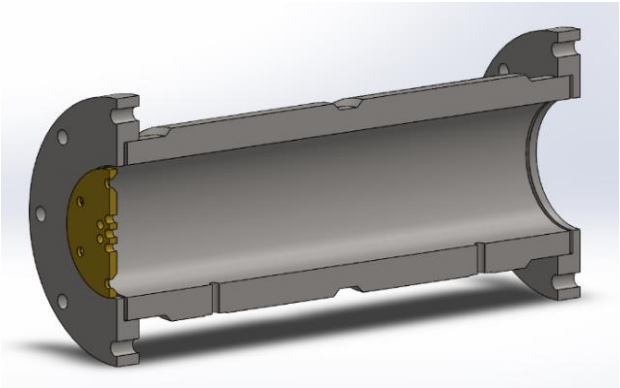

Figure 3.6: *CAD model section view of the Injector Plate and the Pre-Chamber.*

Mesh Size	
Cells	142893
Faces	291987
Nodes	27150
Physical Models	
Space	3D
Time	Steady
Viscous	Standard k-epsilon turbulence model
Wall Treatment	Standard Wall Functions
Heat Transfer	Enabled
Boundary Conditions	
Inlet	
Mass Flow Rate	0.1 kg/s
Temperature	300 K
Outlet	
Pressure	101325 Pa
Wall	
Shear Boundary Condition	No Slip

Table 3.1: *Injection simulation setup parameters.*

The simulation was set up with the goal of reproducing the oxygen injection into an unrealistically long Pre-Chamber (500 mm), in such a way that the point of flow reattachment could be identified and the necessary Pre-Chamber length defined. The fluid domain is shown in Figure 3.7 while main simulation parameters are reported in Table 3.1.

As it is possible to observe from the resulting streamlines reported in Figure 3.8, the flow reaches a uniform state around 250 mm from the injection point. Therefore, the length of the Pre-Chamber was chosen to be 300 mm in order to be completely sure to have a homogeneous and laminar flow at the Main-Chamber inlet and, in addition, to have some flexibility in case the oxidizer mass flow rate is increased in the future.

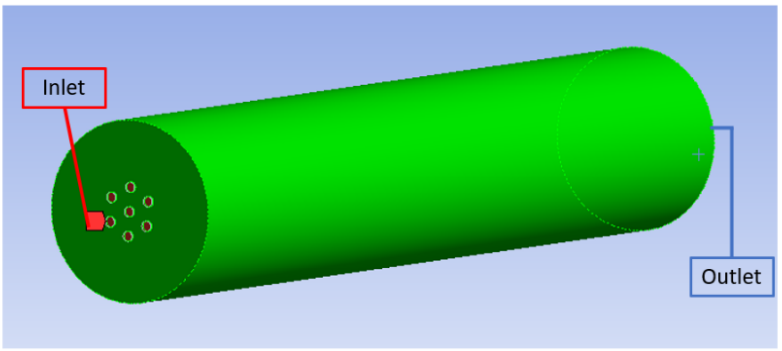

Figure 3.7: *Fluid domain of the CFD injection simulation.*

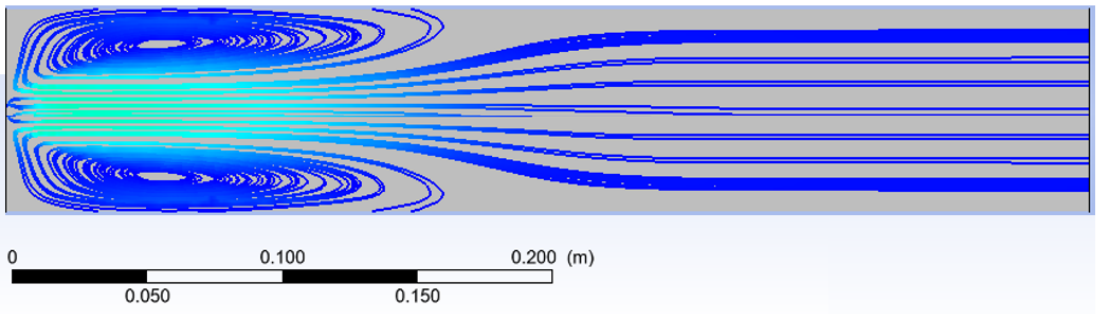

Figure 3.8: *Injection CFD simulation resulting streamlines.*

Post-Chamber

As the Pre-Chamber, the Post-Chamber is also built starting from a hollow bar with a 74 mm ID and a 108 mm OD. In *MOUETTE* application, the main function of the Post-Chamber is not to ensure the completion of the combustion reactions, but rather to provide some separation between the Main-chamber and the Nozzle, so that the internal ballistics is not affected by nozzle fluid dynamics.

The Post-Chamber is 160 mm long and it is designed to accommodate the Convergent Insert in graphite to direct combustion products to the Nozzle.

Figure 3.9: *From left to right, picture of Post-Chamber, Pre-Chamber and Main-Chamber.*

3.3.2 Flanges and Welding

The Flanges are essential components of *MOUETTE* because they have the function to connect the three chambers in correspondence of their extremities, and to form therefore a modular structure.
The Flanges' size is compatible with the old *ULB-RMA* combustion chamber (see Section 3.1), thus having a 150 mm external diameter and 8 holes for M8 bolts located on a circumference of 130 mm diameter. They are machined from AISI 304L stainless steel plates and then welded to the ends of the chambers.
The alternative of obtaining each chamber with its two flanges from a single piece of stainless steel, to be machined from solid, was immediately discarded because of the extremely high cost of both material and machining, and because the advantage of constructing the chambers from commercial hollow bars would be lost.

The welding of Flanges to the chambers was treated and designed with special care to ensure structural tightness even at high pressures. Therefore, it was decided to adopt the so-called *Socket Flange Welding*, a peculiar welding procedure for high-pressure piping in accordance with ASME B31.1 1998 127.3 standard.
As it is possible to observe in technical drawing in Figure 3.10, for each Flange, a double welding was performed as explained in the following.

First of all, the Flange was welded to the external surface of the chamber by means of a tungsten inert gas (TIG) welding without filler metal. The junction is made by fusion of the two components to be welded, suitably placed side by side. It was decided to avoid the presence of a weld bead to prevent the possible formation of cracks in it and their subsequent branching, which could eventually lead to the failure of the welded joint.
Furthermore, an additional welding was performed in the internal part of Flanges. As shown in Figure 3.10, Flanges are designed to have an internal step so that the hollow bar ends can be inserted into them. To allow for thermal expansion, the chamber ends are not in contact with the inside of the Flanges, but a 2 mm gap is provided. Then, the inner surfaces of the hollow bar and the flange were joined by a Metal-arc Inert Gas (MIG) welding with filler metal. Once the internal welding was completed, the weld bead was machined on the lathe to obtain a uniform 74 mm in diameter and avoid the generation of flow distortions.

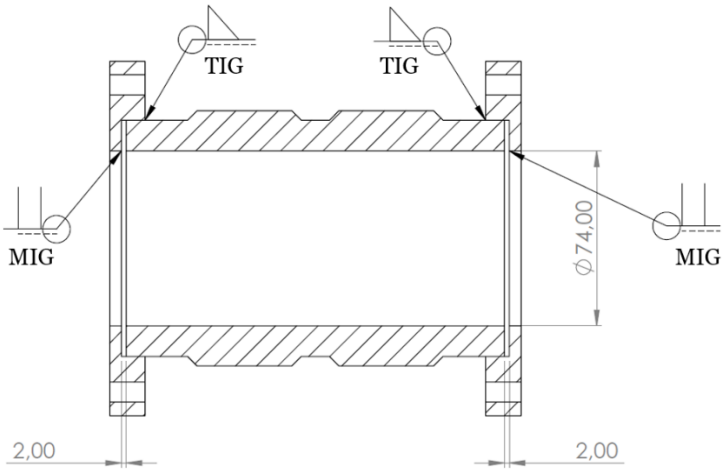

Figure 3.10: *Socket Flange Welding in a section view of the Post-Chamber drawing. Dimensions in millimeters.*

Figure 3.11: *External welding, Main-Chamber.*

3.3.3 Window Frame

The Window Frames are essential components of *MOUETTE* as their function is to hold the two quartz Glasses in place and thus allow the visualization of the combustion phenomenon. Furthermore, Window Frames have a considerable structural importance, namely to withstand the pressure generated in the engine.
Each Window Frame is built in aluminum, as it is not in direct contact with gaseous oxygen, and has a rectangular shape of 189 x 91 mm, with a thickness of 20 mm. It is connected to the Main-chamber by sixteen M5 countersank stainless steel screws.

Although a much smaller number of screws would be sufficient to withstand the pressure difference between the chamber pressure and the external atmospheric pressure, it was decided to connect each Window Frame to the Main-chamber with sixteen screws, for the reason explained in the following.
The stress generated by the previous-mentioned pressure jump across the window acts on the Glass and is then transmitted to the Window Frame, where it is supported by the screws that hold the two components in place.
Since the Glass is the most critical component, as it is more prone to breakage, a large number of screws is appropriate to have a uniform load distribution, as well as a homogeneous stress state. In the extreme case where only two screws are used to connect the Window Frame to the chamber, it is clear that the stress in the Glass would be concentrated at the points closest to the screws, generating a bending load eventually causing its breakage.

On the outward face, the Window Frame has a slit of the same size as the opening in the Main-chamber (133 x 48 mm). Instead, in the face in contact with the Main-chamber, it features a housing of 15 mm depth to accommodate the Glass. The size of this slot is 153 x 60 mm with rounded corners, slightly larger than the Glass size to allow for the introduction of a gasket layer between the quartz and the aluminum. Please refer to Sections 3.4 and 3.5 for a more detailed description of the coupling between the Window Frame and Glass and the gaskets used.

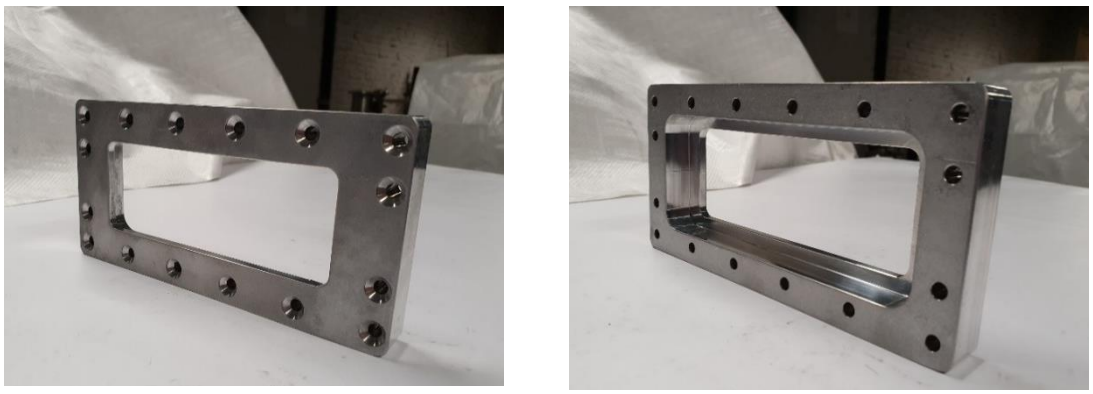

Figure 3.12: *Picture of the front and back of the Window Frame.*

3.3.4 Injector Head and Injector Plate

The Injector Head and the Injector Plate are the two parts that compose *MOUETTE*'s injection system. Oxygen enters the Injector Head and it is then injected into the Pre-chamber through the Injector Plate.

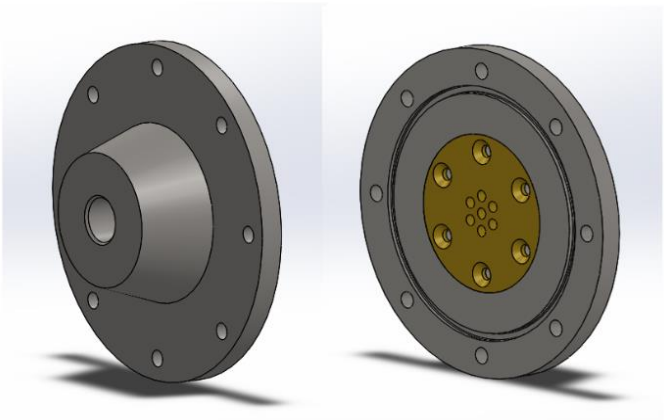

Figure 3.13: *CAD image of the Injector Head and the Injector Plate.*

Figure 3.14: *Picture of the Injector Head and the Injector*

Injector Head

The Injector Head is built in AISI 304L stainless steel and has the same dimensions of the Flanges to ensure connection to the Pre-chamber, i.e., it features a 150 mm external diameter and 8 holes for M8 bolts located on a circumference of 130 mm diameter.

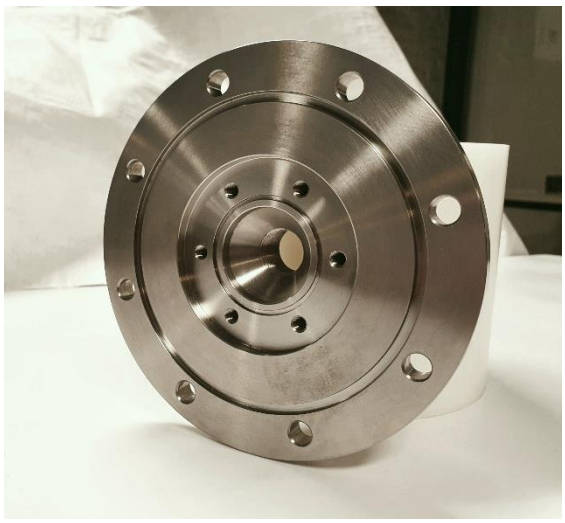

Figure 3.15: *Injector Head picture.*

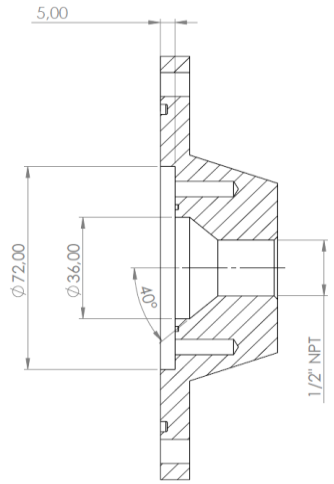

Figure 3.16: *Section view of the Injector Head drawing (simplified version). Dimensions in millimeters.*

As shown in the picture in Figure 3.15 and in the section view in Figure 3.16, on one side the Injector Head has a truncated cone geometry with a 1/2" NPT female threaded hole for the connection of the feed line. Instead, on the face in contact with the Pre-chamber, the Injector Head features a slot to accommodate the Injection Plate. Two O-ring grooves are visible: an external one on the contact surface between Injector Head and Pre-chamber and an internal one on the contact surface between Injector Head and Injector Plate.
Internally, the Injector Head has a divergent manifold to distribute and decelerate the oxidizer flow before reaching the Injector Plate.

Injector Plate

The Injector Plate has the function to uniform, distribute and inject into the Pre-chamber the oxygen flow delivered by the feedline. Unlike liquid rocket engines and hybrid rocket engines with liquid oxidizer where the injection plate is responsible for the atomization process, in *MOUETTE* application the plate plays the role of a distribution grid.
The Injector Plate, built in brass, has a circular shape of 72 mm diameter with a 5 mm thickness and it is inserted in the appropriate slot inside the Injector Head. It is fixed by six M5 stainless steel countersank screws that are fastened into the Injector Head.

The flow is injected through 5 mm diameter holes, whose number (N), and related flow passage area, was chosen in order to obtain the desired pressure jump across the Injector Plate. Two plates were designed and built, as shown in Figure 3.15:

- Injector Plate A, featuring $N = 7$ holes for oxygen passage (1 central hole and 6 external holes located on a 16 mm diameter circumference);
- Injector Plate B, featuring $N = 19$ holes for oxygen passage (12 holes in addition with respect to plate A, located on a 26 mm diameter circumference).

Figure 3.17: *Picture of Injector Head A (left) and Injector Plate B (right).*

The design procedure that led to the decision to have two different injector plates to be suitable for every engine's operating condition range, in terms of both mass flow rate and chamber pressure, is explained in the following.

Discharge coefficient estimation

As a first step, the Injector Plate discharge coefficient C_d was estimated. In a nozzle or orifice, the discharge coefficient is defined as the ratio between the actual to the ideal mass flow rate discharged, hence being by definition always less than 1. Even if the discharge coefficient of orifice plates is known to be around 0.6, it was evaluated in order to have a higher degree of accuracy. In accordance to Reference [33], the Injector Plate was modelled as a single orifice plate, and the following correlations were used to estimate C_d.

$$C_d = C_{d,\infty} + \frac{b}{Re^z} \tag{3.1}$$

where $C_{d,\infty}$, the discharge coefficient at infinite Reynolds number, b and z are computed as follows:

$$C_{d,\infty} = 0.5959 + 0.0312\,\beta^{2.1} - 0.184\,\beta^6 \tag{3.2}$$

$$b = 91.71\,\beta^{2.5} \tag{3.3}$$

$$z = 0.75 \tag{3.4}$$

being β is the ratio of the orifice throat diameter to the pipe diameter ($\beta = D_0/D_1$ in reference to Figure 3.18).

The resulting discharge coefficients for the two Injector Plates for different oxidizer mass flow rates are reported in Table 3.2. Pressure dependence was found to be negligible; temperature is 300 K as oxygen is injected at ambient temperature.

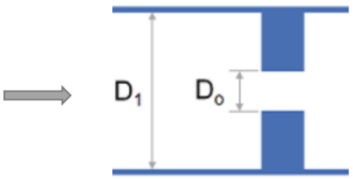

Figure 3.18: *Orifice schematic.*

	Oxygen Mass Flow Rate		
	50 g/s	75 g/s	100 g/s
C_d - Injector Plate A	0.6023	0.6015	0.6010
C_d - Injector Plate B	0.6304	0.6218	0.6171

Table 3.2: *Estimated discharge coefficients for Injector Plate A and B.*

Injection pressure estimation

The injection pressure, i.e. the pressure of the oxidizer flow upstream the Injector Plate, was estimated in order to be able to define the number of holes on the Injector Plate suited to grant a correct pressure jump. In particular, the design choice was to have a limited pressure jump to avoid flow choking, as the oxidizer flow is already choked in the feedline (see Section 3.8 for more details).

The compressible fluid flow across an orifice in un-choked conditions may be calculated as [34]:

$$\dot{m} = C_d A_O \sqrt{2 p_1 \rho_1 \frac{\gamma}{\gamma - 1} \left[\left(\frac{p_2}{p_1} \right)^{2/\gamma} - \left(\frac{p_2}{p_1} \right)^{\gamma + 1/\gamma} \right]} \tag{3.5}$$

where subscript 1 and 2 indicate orifice upstream and downstream conditions, respectively. γ is the ratio of specific heats while A_O is the orifice throat area. The mass flow rate through the orifice is limited by the discharge coefficient, and usually the product between C_d and A_0 is called *corrected* or *effective* throat area.

Under choked flow conditions, instead, the flow rate becomes [34]:

$$\dot{m} = C_d A_0 \sqrt{\gamma p_1 \rho_1 \left(\frac{2}{\gamma + 1} \right)^{\frac{\gamma + 1}{\gamma - 1}}} \tag{3.6}$$

It can be shown that choking conditions are reached as soon as the ratio between the orifice downstream pressure (p_2) and the upstream total pressure (p_{T1}) is lower than the so-called *critical ratio* (*CR*).
Assuming an isentropic flow through the orifice, i.e. without heat transfer nor dissipations, p_{T1} is constant. Imposing choked flow in the orifice throat, i.e. Mach number equal to 1, the lowest efflux pressure (p_{eff}) may be computed.

$$p_{T1} = p_1 \left(1 + \frac{\gamma - 1}{2} M_1^2 \right)^{\frac{\gamma}{\gamma - 1}} = const = p_{eff} \left(\frac{\gamma + 1}{2} \right)^{\frac{\gamma}{\gamma - 1}} \tag{3.7}$$

$$CR = \frac{p_{eff}}{p_{T1}} = \left(\frac{2}{\gamma + 1} \right)^{\frac{\gamma}{\gamma - 1}} \tag{3.8}$$

The *critical ratio*, defined as the ratio of the lowest efflux pressure to the total upstream pressure, provides hence a useful tool to evaluate whether or not the orifice is chocked. If the orifice downstream pressure (p_2) is lower than the lowest efflux reachable (p_{eff}), i.e. $p_2/p_{T1} < CR$, the flow is choked.

On the basis of the above reported equations, an algorithm was implemented in MATLAB® to evaluate the injection pressure on the basis of the engine operating conditions (oxygen mass flow rate $\dot{m}_{ox}$ and chamber pressure p_c) and Injector Plate properties. As $\dot{m} = \dot{m}_{ox}$ and $p_c = p_2$ are known, the algorithm computes the injection pressure p_1 by means of an iterative cycle. As shown in the algorithm flowchart in

Figure 3.19, p_1 is firstly guessed and then it is corrected iteratively to respect mass conservation.
The algorithm enabled to characterize the behavior of any Injector Plate geometry in terms of relative injection pressure, thus allowing the selection of the number of holes needed to ensure a correct pressure jump under various operating conditions. Injector Plate A and B, with respectively 7 and 19 holes for oxygen passage, were chosen. The estimated injection pressures for some chamber pressure values and are reported in Table 3.3 and 3.4.

For estimating both the discharge coefficient and the injection pressure, as well as for any other calculation performed in the thesis wok, oxygen thermophysical properties from National Institute of Standards and Technology (NIST) database were used.

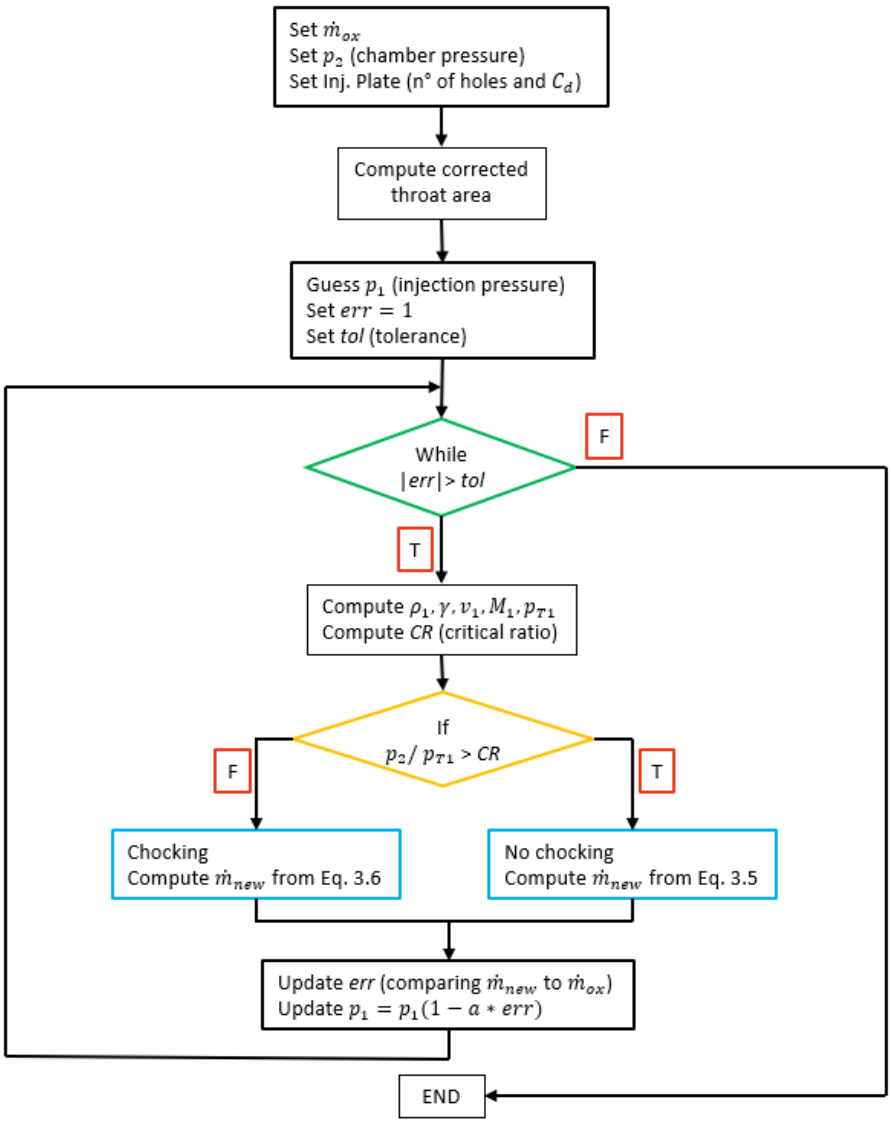

Figure 3.19: *Flowchart of the algorithm implemented to estimate the injection pressure.*

Injector Plate A

$\dot{m}_{ox}$= 50 g/s		$\dot{m}_{ox}$= 75 g/s		$\dot{m}_{ox}$= 100 g/s	
p_1 [bar]	p_2 [bar]	p_1 [bar]	p_2 [bar]	p_1 [bar]	p_2 [bar]
2.49	1.5	3.69	1.5	4.92	1.5
3.48	3	4.09	3	4.98	3
5.28	5	5.64	5	6.16	5
10.14	10	10.32	10	10.57	10
15.09	15	15.21	15	15.38	15

Table 3.3: *Estimated injection pressure as function of chamber pressure and oxidizer mass flow rate - Injector Plate A.*

Injector Plate B

$\dot{m}_{ox}$= 50 g/s		$\dot{m}_{ox}$= 75 g/s		$\dot{m}_{ox}$= 100 g/s	
p_1 [bar]	p_2 [bar]	p_1 [bar]	p_2 [bar]	p_1 [bar]	p_2 [bar]
1.61	1.5	1.78	1.5	2.00	1.5
3.06	3	3.14	3	3.25	3
5.04	5	5.08	5	5.15	5
10.02	10	10.04	10	10.07	10
15.01	15	15.03	15	15.05	15

Table 3.4: *Estimated injection pressure as function of chamber pressure and oxidizer mass flow rate - Injector Plate B.*

3.3.5 Nozzle Plate

The Nozzle Plate, built in AISI 304L stainless steel, represents the engine's closure and it is located downstream of the Post-Chamber. As well as the Injector Head and Flanges, it features a 150 mm external diameter and 8 holes for M8 bolts located on a circumference of 130 mm diameter.

The Nozzle Plate has 20 mm thickness and, as shown in the cross section view of the technical drawing in Figure 3.20, its peculiarity is to present an internal housing to accommodate the nozzle. In addition, an O-ring groove was machined on the its contact surface to the Post-Chamber.

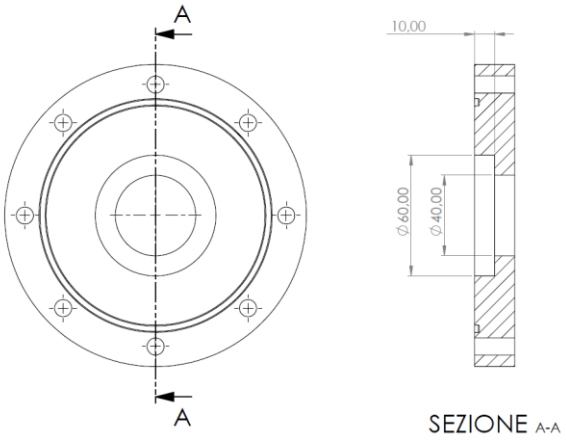

Figure 3.20: *Section view of the Nozzle Plate drawing (simplified version). Dimensions in millimeters.*

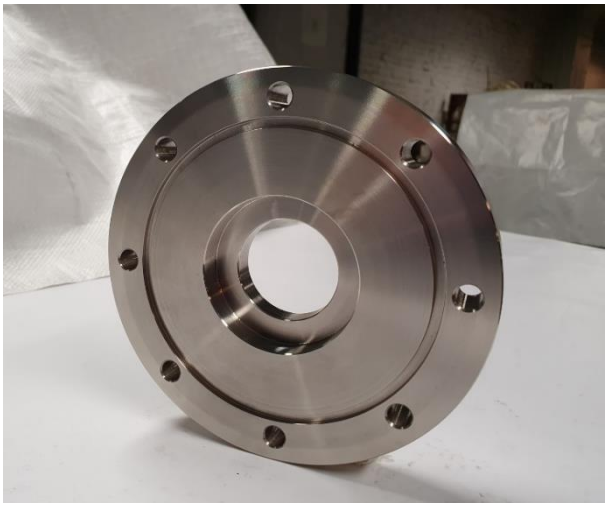

Figure 3.21: *Nozzle Plate*

3.3.6 Grain Holder and Pre-Chamber Insert

As shown seen in Figure 3.22, the Grain Holder and the Pre-Chamber Insert are the two components located at the bottom of the Main-Chamber and Pre-Chamber, respectively.
As the name implies, the Grain Holder has the function of holding in place the solid fuel grain and hence features a rectangular groove to accommodate it. Since the sole presence of the Grain Holder would imply the existence of a step in its fore end, a Pre-Chamber Insert was added to preserve a uniform internal section and avoid the formation of turbulent structures in the flow field.

Brass C36000, composed of 61.5% copper, 35.5% zinc and 3% lead [35], was chosen as the material for both the Grain Holder and Pre-Chamber Insert due to its high machinability, compatibility with oxygen and high thermal conductivity, which is important to avoid overheating. Brass C36000 thermal conductivity is 115 W/(m·K) [35], rather higher than stainless steel one, which is around 16 W/(m·K) for AISI 304L [32].

Both the Grain Holder and the Pre-Chamber Insert are held in place to the respective chambers by M5 stainless steel screws, as shown in Figure 3.3.

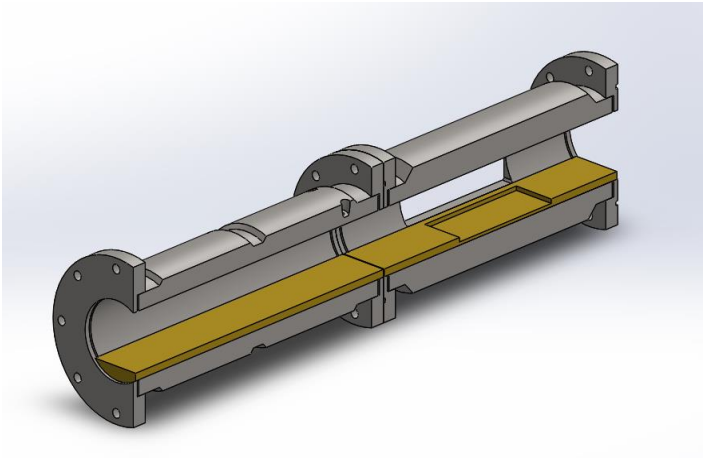

Figure 3.22: *CAD image of the Grain Holder and Pre-Chamber Insert placed on the respective chambers.*

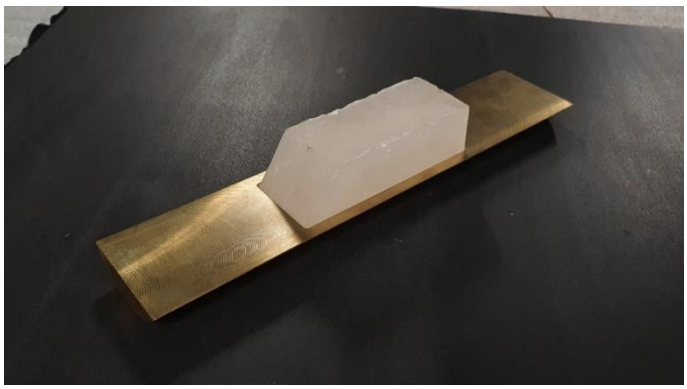

Figure 3.23: *Picture of the paraffin grain positioned on the Grain Holder.*

3.4 Glass

The two Glasses are fundamental components for *MOUETTE*, as they ensure that the internal ballistics of the hybrid rocket engine can be visualized from outside, granting the major requirement of optical accessibility. As the Glass is fragile, it was necessary to select the material and design the component, as well as its coupling to the Main-Chamber and the Window Frame, with particular care. A picture of the Glass is reported in Figure 3.24.

3.4.1 Material Selection

The three main criteria used for material selection were: operating temperature, mechanical load and useful transmittance range. The materials that were considered together with their optical, mechanical, and thermal properties are shown in Table 3.5, while their transmittance curve is shown in Figure 3.25.

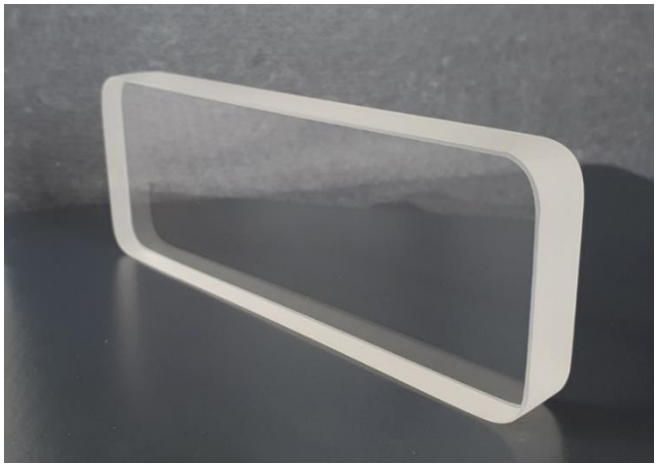

Figure 3.24: *Quartz Glass picture.*

The Glass operates under high temperature conditions, as a consequence, it was essential to choose a material with a high maximum continuous operating temperature and a low coefficient of thermal expansion. The minimum thermal expansion coefficient is desired because, otherwise, a large expansion of the Glass, which is accommodated in the Window Frame, would eventually lead to its breakage.
Soda lime, borosilicate and magnesium fluoride glasses were therefore discarded.
Sapphire has very good mechanical properties, but, due to its extreme hardness (second hardest material on Earth) and high melting point, the manufacturing process is challenging and expensive. This, added to its high thermal expansion coefficient made sapphire inappropriate as material for the Glass.

Therefore, the choice was to have quartz Glasses. Quartz and silica are basically the same material, the difference is only that quartz is made from melted and cleansed naturally occurring quartz sand with larger amount of contamination in the product, while fused silica is a pure version of quartz synthetized from various gases. Quartz has both a high maximum continuous operating temperature and the lowest thermal expansion coefficient, which make it perfect for *MOUETTE* application. Indeed, the major advantage of quartz is its increased stability: the mechanical properties are significantly less sensitive to temperature variations than other glasses as borosilicate. In addition, although inferior to sapphire, quartz possesses significantly greater hardness than more common glass materials. This allows to avoid/minimize the formation of superficial cracks in the Glass caused by small impacts during the assembly phase. In any case, the Glass assembly procedure to the Main-Chamber and Window Frame must be done very carefully.
As can be seen in the transmittance curves shown in Figure 3.19, the transmittance value of quartz, i.e. the ratio of electromagnetic energy transmitted through a body to the incident one, is good over a considerable range of wavelengths.

	Unit	Soda Lime Glass	Borosilicate	Quartz	Fused Silica	Sapphire	Magnesium Fluoride
General							
Chemical Formula, Composition	(weight %)	SiO_2:74, Na_2O:15, CaO:5, others	SiO_2:80+, B_2O_3:7-13%, Na_2O, others	SiO_2:99	SiO2:99	Al_2O_3:99	MgF_2:99
Density	(g/cm^3)	2.2-2.52	2.2-2.4	2.2	2.2	3.98	3.18
Optical							
Useful Transmission	(nm)	320-2300	325-2100	200-2400	180-2200	150-5000	110-7500
Refractive index (588 nm)	-	1.52	1.47	1.46	1.46	1.76	1.38
Mechanical [I]							0
Young's Modulus	(GPa)	72	64	73	73	335	138
Tensile Strength	(MPa)	41	27-62	50	50	275 [II]	140
Hardness, Vickers	-	550	520-580	1000-1200	1000-1200	1940	400
Poisson's ratio	-	0.23	0.21	0.17	0.17	0.25	0.27
Weibull variability of strength	-	6 [III]	30 [IV]	8.82 [V]	10.2 [VI]	5	5
Weibull stress	(MPa)	129 [III]	71 [IV]	115 [V]	180 [VI]	485	96
Thermal							
Softening Point	(°C)	1450	800-850	1730	1600	2300 [VII]	1255
Max. Continuous Operating Temperature	(°C)	260	280-350	950-1150	950-1100	1200	500
Thermal Conductivity at 300 K	(W/mK)	0.96	1.1-1.2	1.38	1.38	27.21	11.6
Coefficient of Expansion	(10^{-6}/K)	3.5-9	3.25-4	0.55	0.55	8.4	8.9

properties perpendicular to optical axis

materials are birefringent for exact refractive indexes see references

[I] mechanical and optical properties are dependent on fabrication method and surface finish; [II] fractural strength; [III] Kimble R-6; [IV] BK-7; [V] standard polish; [VI] "super polish"; [VII] melting point

Table 3.5: *Optical material properties [36].*

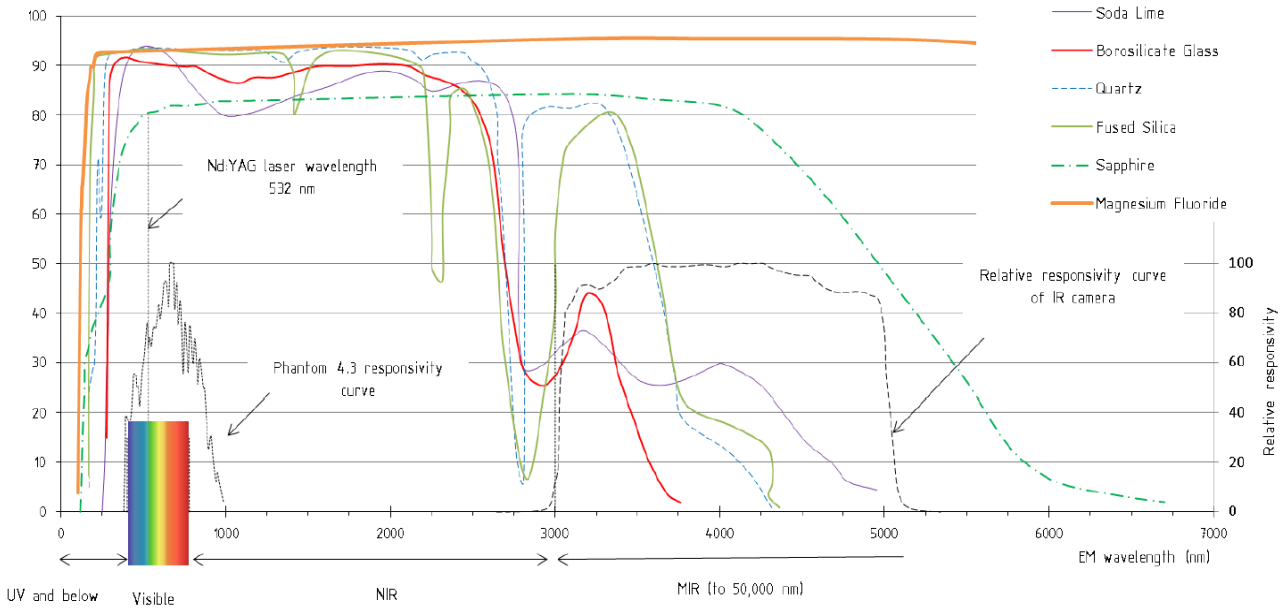

Figure 3.25: *Transmittance (in %) curves of optical materials [36].*

3.4.2 Thickness Sizing

In accordance with Reference [36], the minimum Glass thickness (t) required for a sight window on pressure vessels can be calculated as:

$$t = \frac{1}{2} D_0 \left(\frac{K \cdot SF \cdot \Delta p}{\sigma_y} \right)^{1/2} \tag{3.9}$$

where D_0 is the length of the window aperture (133 mm) as shown in Figure 3.26, K is a generalized constant for supported windows suggested by Reference [37], SF is the safety factor, Δp is the pressure difference between the pressure inside the chamber and the external atmospheric one and σ_y is the tensile yield strength.
Considering a safety factor of 2.5 to account for possible overpressures and to derate the allowable stress of quartz, and a maximum pressure difference as a result of the limit chamber pressure of 15 bar, the minimum Glass thickness required is 15.2 mm. It was therefore decided to have a quartz Glass of 16 mm thickness.

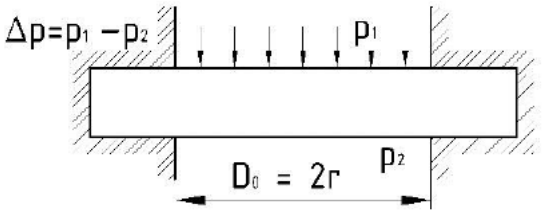

Figure 3.26: *Reference image for a supported window [36].*

3.4.3 Glass Dimensioning and Interfaces

Each quartz Glass features a 150 x 56 mm rectangular shape with rounded corners and has been designed to be positioned in the special slot machined on the side faces of the Main-Chamber, and then held in place by the Window Frame.
Since the Glass is a fragile component, it was decided, in addition to an accurate design of the Window Frame (refer to Section 3.3.3), to adopt a system of gaskets to avoid direct contact between Glass and metal parts and the possible formation of cracks due to impacts. First of all, both slots to accommodate the glass at the Main-Chamber and the Window Frame have a size of 153 x 60 mm, slightly larger than the Glass for the purpose of introducing an external gasket layer, as reported in Figure 3.27. Furthermore, two lateral layers of gaskets were introduced on the side contact surfaces between Glass and Main-Chamber, and between Glass and Window Frame. The whole system of gaskets is shown in Figure 3.28.
In addition to the Glass protection, the gasket layers also ensure the sealing of the window to avoid flow leakage.

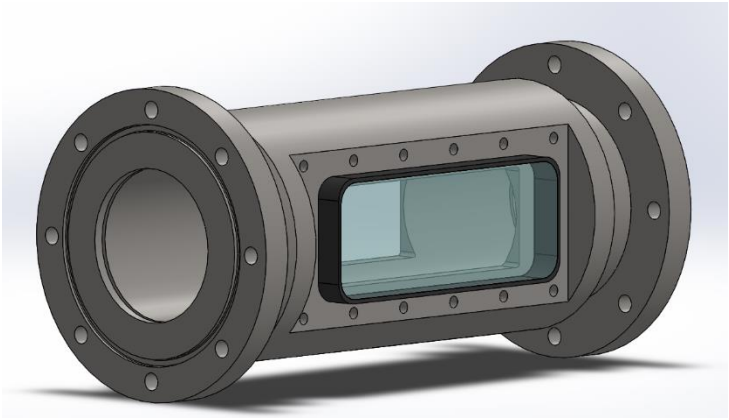

Figure 3.27: *CAD image of the Glass positioned on the Main-Chamber.*

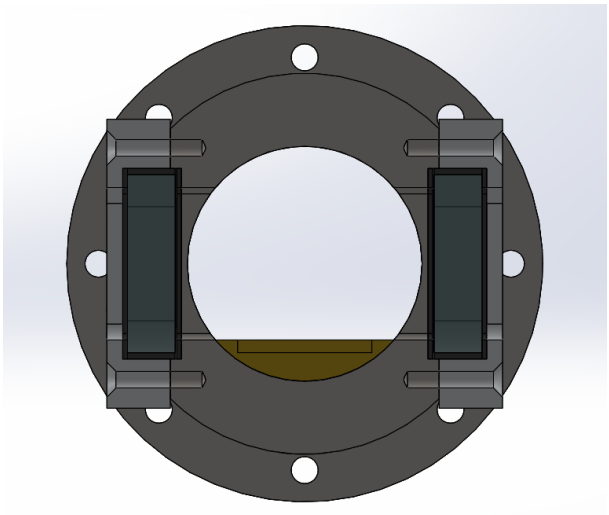

Figure 3.28: *CAD section view of the Main-Chamber.*

3.5 Gaskets

Due to the modular design of the engine, which is not a single-piece but consists of several interconnected components, as well as the presence of two side windows, the gaskets are fundamental elements of *MOUETTE* as they ensure the connections' sealing, preventing flow leakage.

The engine requires gaskets in correspondence of the following connections.

- *Flanges connection*. In particular, this refers to the connection between the structural components of *MOUETTE*, namely the connections between: Injector Head and Pre-Chamber, Pre-Chamber and Main-Chamber, Main-Chamber and Post-Chamber, Post-Chamber and Nozzle Plate. Sealing is ensured by four O-rings with a 3 mm cross section and an internal diameter of 110 mm.

Since, for each connection with O-ring sealing, only one gland is necessary, it was decided to machine the grooves to accommodate O-rings on the Injector Head, on the 2 Flanges of the Main-Chamber and on the Nozzle Plate.

- *Injector Head - Injector Plate connection.* The Injector Plate is accommodated in a slot inside the Injector Head. To avoid leakage and losses in the oxidizer flow, a sealing O-ring is introduced between the two contact surfaces, so that oxygen flows only to the injection holes on the Injector Plate. The O-ring features a 1.5 mm cross section and a 42 mm internal diameter.
- *Glass - Window Frame - Main-Chamber interface.* At the two side windows of the engine, where these three components are interconnected, gasket layers were used with the dual function of protecting the glass and ensuring sealing. Please refer to Subsection 3.4.3 for more details.

O-rings owe the sealing capacity to their elastic nature. As an elastomer is non-compressible, under a certain load, the O-ring deforms depending on the available volume of its housing. As consequence, it was essential to design the O-ring housing in function of its application to have a correct deformation and ensure sealing, as shown in Figure 3.29.
Therefore, the O-ring glandes for both *Flanges connection* and *Injector Head - Injector Plate connection* were calculated for the specific application of static axial squeeze face sealing (Figure 3.30), following the rules suggested in Reference [38].

Since, because of combustion, the temperature reached in the engine is much higher than the maximum operating temperatures of any elastomers, gaskets result to be consumable materials to be changed quite frequently. For this reason, although elastomers such as fluorocarbon rubbers (FPM/FKM) and methyl silicon vinyl rubbers (VMQ) would be preferable due to their better properties, the material selected was nitrile butadiene rubber, also known as NBR or Buna-N. NBR, indeed, is around 10 times cheaper than FKM and VMQ, and hence is more appropriate as consumable material.

Figure 3.29: *O-ring deformation caused by a pressurized fluid [39].*

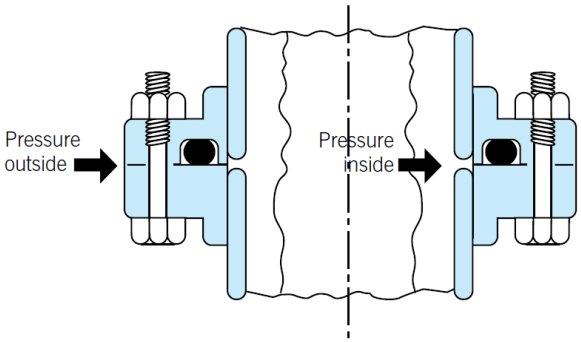

***Figure 3.30**: Static Application for O-rings with Axial Squeeze [38].*

3.6 Fuel Grain

The fuel sample is placed over the Grain Holder in correspondence of the Main-Chamber windows so that the combustion phenomenon can be visualized from the outside of the engine.
From now on, the generic term of fuel is referred to paraffin, as the latter is nowadays the most interesting hybrid fuel and because *MOUETTE* project was precisely pointed to investigate liquefying hybrid fuels.

As shown in Figure 3.31, the fuel sample has a parallelepiped shape, characterized, however, by an angled leading edge, in order to anchor the flame but at the same time avoid the generation of high turbulence. The propellant grain was obtained by melting raw paraffin pellets and subsequent cooling and solidification in a mold. The paraffin mold, shown in Figure 3.32, was 3D printed in the Aéro-Thermo-Mécanique Department Laboratory of *Université Libre de Bruxelles*.

***Figure 3.31:** Paraffin grain and pellets.*

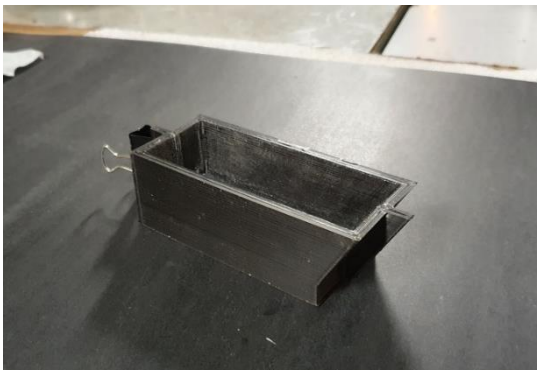

***Figure 3.32:** Mold for paraffin grains.*

3.7 Nozzle

3.7.1 Exhaust System Overview

The exhaust system of *MOUETTE* consists of a Convergent Insert and a Nozzle, both manufactured in graphite.
As the name suggests, the Convergent Insert is designed to be inserted inside the Post-Chamber and has the function of directing combustion products to the Nozzle. It features a length of 50 mm and, when inserted into the Post-Chamber, it rests on the Nozzle Plate as indicated in Figure 3.33. The Nozzle is positioned in the housing inside the Nozzle Plate, features a 20 mm length and has the crucial function of adjusting the combustion chamber pressure. A section view of *MOUETTE* complete with graphite parts is shown Figure 3.34.
Since, in *MOUETTE* applications, the specific impulse is not a parameter of interest, it was chosen to have a convergent Nozzle, instead of a convergent-divergent one, with the function of accelerating the flow of combustion products up to *Mach* 1 at its efflux section. As a consequence, the Nozzle throat area, which is the Nozzle's smallest cross-section and one of the most significant engine parameters as it establishes the chamber pressure, coincides with the efflux area. To meet *MOUETTE*'s requirement of operating at different values of chamber pressure, different Nozzles with different throat areas were designed. The procedure is explained in the following.

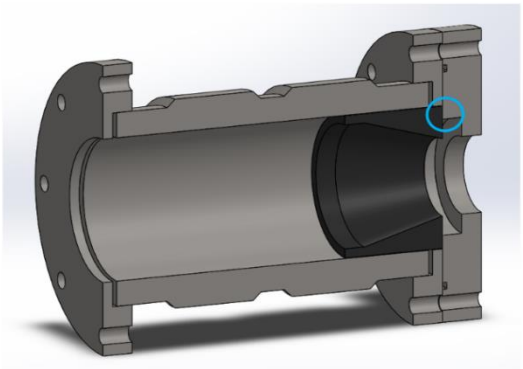

Figure 3.33: *CAD section view of Post-Chamber, Nozzle Plate and Convergent Insert.*

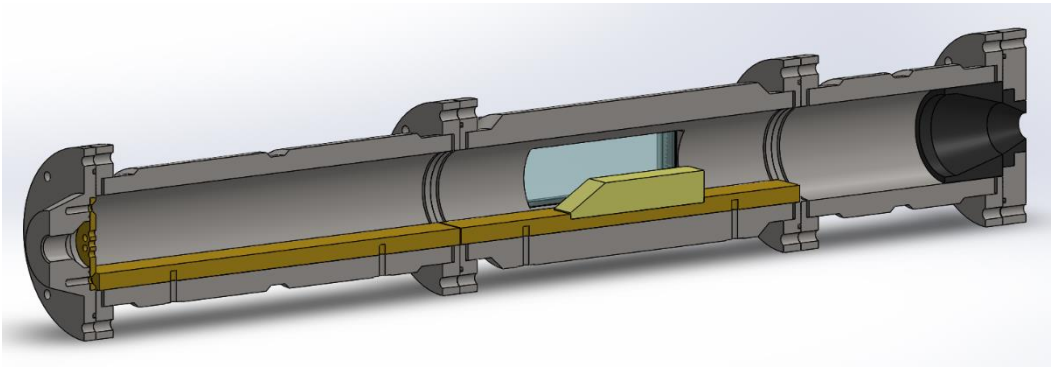

Figure 3.34: *CAD section view of MOUETTE.*

3.7.2 Combustion Process Estimation and Nozzles Selection

In order to calculate the Nozzle throat area, the characteristic velocity (c^*) definition was considered. Though not a physical velocity, c^* is frequently used as a merit parameter in rocket propulsion literature to compare the relative performance of different chemical rocket propulsion system designs and propellants, and it is defined as shown in Equation 3.10 [40].

$$c^* = \frac{p_c \, A_t}{\dot{m}} \tag{3.10}$$

It follows that, knowing the characteristic velocity, the desired chamber pressure (p_c) and the overall mass flow rate ($\dot{m}$) as the sum of the oxidizer ($\dot{m}_{ox}$) and fuel ($\dot{m}_f$) mass flow rates, the nozzle area to have a sonic throat (A_t) can be computed.

Therefore, to design *MOUETTE*'s Nozzle, the combustion process was estimated with the main goals of computing the fuel mass flow rate and the characteristic velocity.

Estimation of $\dot{m}_f$ and c^*

The characteristic velocity of a propulsion system can be computed using programs such as the *NASA Chemical Equilibrium with Applications (CEA) or Rocket Propulsion Analysis (RPA)*, specifying as inputs the propellant type, the chamber pressure and the oxidizer to fuel ratio (*O/F*). As a consequence, the first step consisted of estimating the regression rate and hence the fuel mass flow rate and the *O/F* ratio.
The evaluation of the mass of fuel leaving the solid grain because of combustion requires the knowledge of the velocity at which the propellant grain recedes. Since, during the design phase, the paraffin burning rate specific for *MOUETTE* was not known, an approximation was introduced: a regression rate correlation was selected and adopted from literature, in particular from Reference [41].

The regression rate was hence computed following the relationship in Equation 3.11, with coefficient a and exponent n equal to 0.15 and 0.46, respectively [41]. Then, the fuel mass flow rate was calculated (Equation 3.12) as the product of the regression rate, the burning area and paraffin density, which is 890 kg/m^3.

$$\dot{r} = a \, (G_{ox})^n \tag{3.11}$$

$$\dot{m}_f = \rho_f \, \dot{r} \, A_b \tag{3.12}$$

The resulting regression rate, fuel mass flow rate and oxidizer to fuel ratio, plotted in function of the oxidizer mass flux and mass flow rates, are reported in Figures 3.35, 3.36 and 3.37. In accordance with the typical values of combustion visualization experiments, the *O/F* ratio is much greater than classical cylindrical hybrid rocket engines. A large *O/F* ratio is indeed deliberately desired in visualization experiments, as the oxidizer excess acts to cool the combustion chamber and windows.

Following the $\dot{m}_f$ estimation and the consequent O/F ratio, the characteristic velocity was calculated using *RPA* software. An example of the result of this calculation is shown in Table 3.6.

Chamber pressure [bar]	Oxygen mass flow rate [g/s]	Fuel mass flow rate [g/s]	O/F	c^* [m/s]
3	50	2.7	18.5	1059

Table 3.6: *Example of the characteristic velocity computation.*

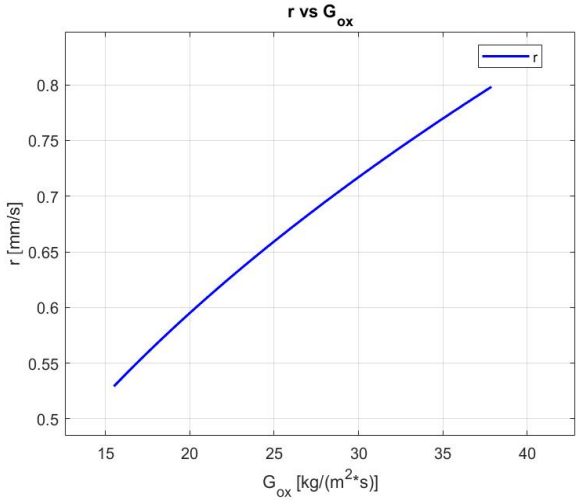

Figure 3.35: *Regression Rate vs Oxygen Mass Flux plot.*

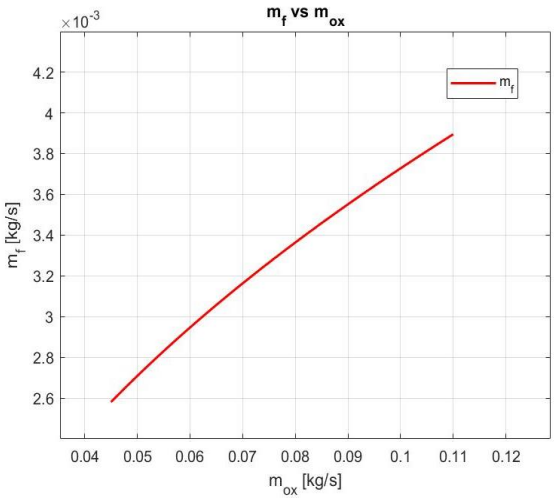

Figure 3.36: *Fuel Mass Flow Rate vs Oxygen Mass Flow Rate plot.*

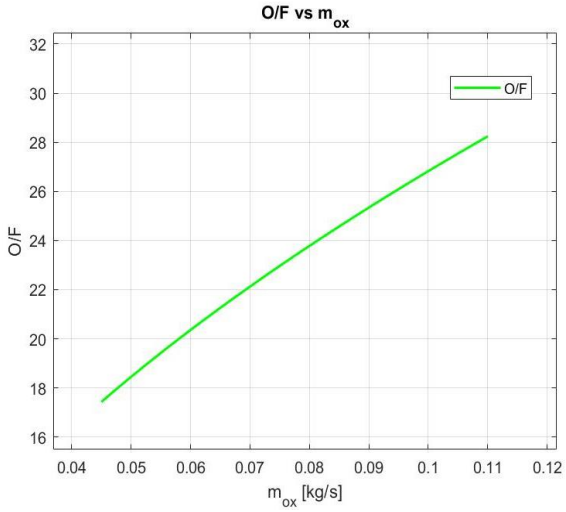

Figure 3.37: *Oxidizer to Fuel Ratio vs Oxygen Mass Flow Rate plot.*

Nozzles Selection

Once the *MOUETTE* operating conditions were chosen in terms of chamber pressure and oxidizer mass flow rate and the resulting combustion process parameters, i.e., fuel mass flow rate, O/F ratio, and characteristic velocity, were estimated, it was possible to calculate the required nozzle throat areas.
As result, five different nozzle geometries were designed to cover the required chamber pressure range from atmospheric conditions to 15 bar. In particular the following throat diameters were selected: 26 mm, 20 mm, 15 mm, 10 mm and 8 mm. The technical drawing of a Nozzle is reported in Figure 3.38, while a picture of the Nozzle – Nozzle Plate assembly is shown in Figure 3.39.

As a final consideration on the Nozzle design procedure, it should be noted that the Nozzle throat areas calculation was affected by an approximation error. In fact, the fuel burning rate was assumed to be equal to that proposed in Reference [41], whose applicability to *MOUETTE* case is, a priori, unknown.
Since the chamber pressure is determined by the throat size, it is then expected that the chamber pressure would be different from the nominal one. Future calibration tests will have the responsibility to determine the actual amount of fuel burned and the actual chamber pressure as function of the chosen and fixed parameters during a test, namely the oxidizer mass flow rate and the Nozzle geometry.

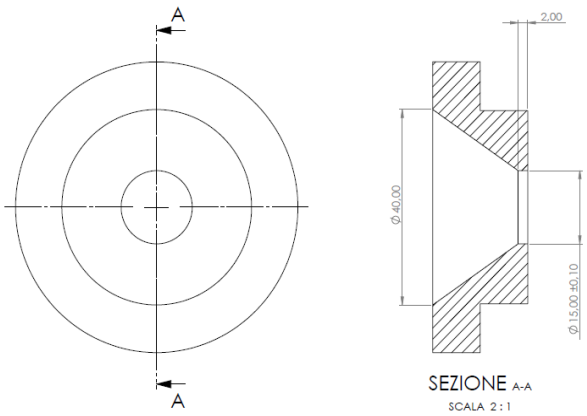

Figure 3.38: *Technical drawing of the 15 mm throat diameter Nozzle (simplified version). Dimensions in millimeters.*

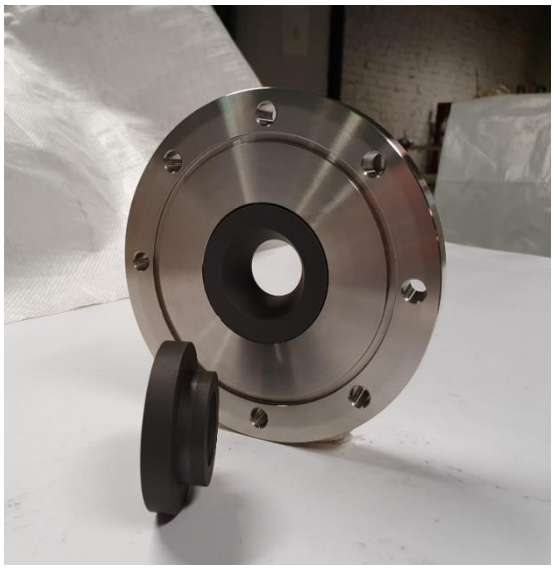

Figure 3.39: *Picture of Nozzle and Nozzle Plate assembly.*

3.8 Feed System

3.8.1 Feed System Overview

MOUETTE's feed system consists of a gaseous oxygen line to supply the oxidizer to the engine and a gaseous nitrogen line for extinguishing the combustion process. Each line features a pressure regulator located on the tank, with the task of setting the desired pressure, and a series of valves to control the flow. The piping and instrumentation schematic of the feed system is shown in Figure 3.40, while the description of each component is in Table 3.7. Please refer to Section 3.9 for the details of the feed system installation on the test bench.

3.8.2 Oxygen and Nitrogen Lines

In the following, the main features of the two lines are presented.
The oxygen line has an electro-pneumatic valve with NAMUR-mounting that acts as the main engine run valve. Being a normally closed valve, when actuated it allows oxygen to flow to the engine or stop the flow to cease combustion. Its pneumatic actuator is operated by nitrogen.
Downstream the oxygen tank, an electro (solenoid) valve is installed to purge the first part of the line when the electro-pneumatic valve is closed, at the end of each combustion test. In addition, the line is equipped with a choked orifice to control the oxygen mass flow rate.

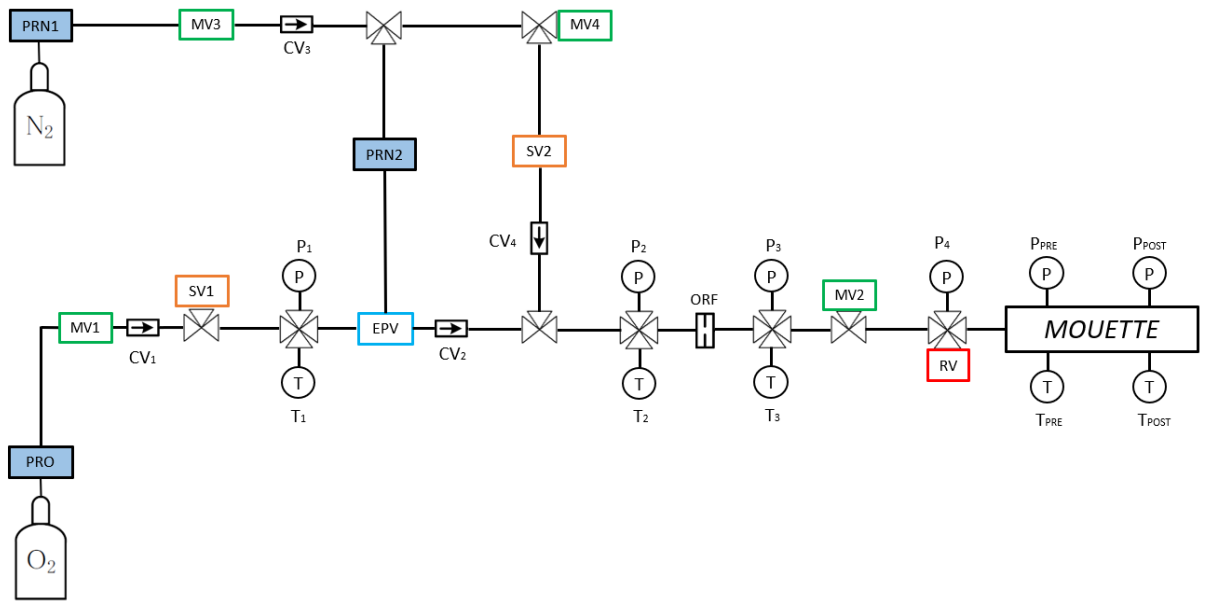

Figure 3.40: *Piping and instrumentation schematic of MOUETTE's feed system.*

Feed line code	Description
CV1 - CV2	Check valve oxygen line
CV3 - CV4	Check valve nitrogen line
EPV	Electro-pneumatic ball valve for oxygen flow control
MV1 - MV2	Manual ball valve oxygen line
MV3 - MV4	Manual ball valve nitrogen line
ORF	Choked orifice
P	Pressure transducer
PRN1	Nitrogen pressure regulator on tank
PRN2	Nitrogen pressure regulator on pneumatic actuator line
PRO	Oxygen pressure regulator on tank
RV	Pressure relief valve
SV1	Solenoid valve for oxygen purge
SV2	Solenoid valve for nitrogen flow control
T	Thermocouple

Table 3.7: *Description of MOUETTE feed system components as indicated in Figure 3.40.*

The size of the oxygen line piping was carefully chosen taking into account the ignition hazard. The use of valves and tube fittings that are compatible with oxygen and have ignition temperatures well above the oxygen flow temperature, leads to the fact that ignition of these materials is not a risk under nominal flow conditions. However, the ignition may occur because of abnormal, localized high temperatures [42] caused, in this case, by the particle impact ignition mechanism. The particle impact ignition mechanism is basically consequence of the heat generated when particles strike a material with sufficient velocity to ignite the particles and/or the material. This ignition phenomenon requires the following elements [43]:

- foreign particles entrained in the oxygen flow;
- high gas velocities, typically greater than 30 m/s;
- an impact point ranging from 45° to perpendicular to the path of the particle.

Since the temperature variation in the line is completely negligible, from the conservation of mass and ideal gas law, Equations 3.13 and 3.14 show that the highest flow velocity occurs in correspondence of the lowest pressure. As the pressure in the line drops after the choked orifice, it was hence decided to position it as close as possible to the engine. Moreover, each oxygen line component was scrupulously cleaned before the assembly to ensure the removal of contaminants and reduce the hazard of ignition.

The nitrogen line has an electro valve that is opened at the end of the tests to shut down the engine. As nitrogen is an inert gas, when injected at ambient temperature, much lower than the one present in the engine during combustion, it cools the combustion chamber and cease the burning phenomenon.
In addition, a secondary line branching off from the main nitrogen line is present. It is equipped with a pressure regulator and is intended to supply pressurized gas to the pneumatic actuator of the oxygen line electro-pneumatic valve.

Both lines are equipped with two manual ball valves each. A first one downstream of the tank to prevent unwanted flow passage during rest conditions and to be opened before testing, a second one to purge the lines when a test is completed.
For safety reasons, a pressure relief valve was introduced right before the engine.

3.8.3 Orifice

The choked orifice is a fundamental component of *MOUETTE*'s feed system as it used to produce the desired mass flow rate. It is basically a Venturi constriction (convergent-divergent nozzle) where, due to the cross section area reduction in the convergent part, the initially subsonic flow is accelerated to sonic conditions, i.e. with a *Mach* number equal to 1. The choked flow condition is useful and convenient because the mass flow rate results to be independent of the downstream pressure, but only depends on the orifice upstream conditions.
In *MOUETTE* application, the pressure on the upstream side of the constriction was imposed and, then, the calibrated orifice dimensions required to provide the desired choked mass flow rate were computed. Since the oxygen mass flow rates of interest are three (50 g/s, 75 g/s and 100 g/s), the orifice was designed, and then manufactured at the Aéro-Thermo-Mécanique Department Laboratory of *Université Libre de Bruxelles*, in order to be adjustable over three different throat diameters.

Figure 3.41: Choked orifice manufacturing on the lathe of the ATM laboratory of Université Libre de Bruxelles from a hexagonal bar of brass.

3.8.4 Pressure Transducers and Thermocouples

As shown in the schematic in Figure 3.34, *MOUETTE* was equipped pressure transducers and thermocouples to measure the thermophysical properties of the flow both in the feed line and in the engine. Their application is described in Table 3.8.

To install the sensors in the Pre-Chamber and Post-Chamber, four threaded holes (two per chamber) for 1/8" NPT connections were machined, see Figure 3.42.

Feed line code	Description
$p_1 - T_1$	Pressure and temperature measurements in the high-pressure sector of the oxygen line
$p_2 - T_2$	Pressure and temperature measurements on the orifice upstream side
$p_3 - T_3$	Pressure and temperature measurements on the orifice downstream side
p_4	Injection pressure measurement
$p_{PRE} - T_{PRE}$	Pressure and temperature measurements in *MOUETTE* Pre-Chamber
$p_{POST} - T_{POST}$	Pressure and temperature measurements in *MOUETTE* Post-Chamber

Table 3.8: *Description of MOUETTE pressure sensors and thermocouples.*

Figure 3.42: *Detail of the two 1/8" NPT threaded holes in the Post-Chamber.*

3.9 Ignition

The solid fuel grain ignition is performed through a so-called *rocket candy*, used as a pyrotechnic igniter. As shown in Figure 3.43, the *rocket candy* is placed on top of the Grain-Holder, near the solid fuel grain, and it is wrapped by a nichrome wire. When a voltage is applied across the wire, the latter heats up due to Joule effect and causes the rocket candy to ignite. The burning of the *rocket candy* generates hot gases causing the fuel grain to heat up and gasify, so that the onset of oxygen flow leads to the grain ignition. After the rocket candy is ignited, the nichrome wire burns through, breaks and is then pushed out of the engine by hot gases.

Rocket candy is basically a type of rocket propellant featuring sugar as fuel, and containing an oxidizer, such as potassium nitrate (KNO_3). The *rocket candies* for *MOUETTE* ignition featured a composition of 40% sugar and 60% KNO_3, their preparation procedure is rather simple and it is explained in the following:

1. Measure the correct mass of sugar and potassium nitrate to respect the desired composition.
2. Mix the two substances in a pan.
3. Put the pan on a hot plate.
4. "Cook" the mixture and mix continuously with a spatula.
5. When the mixture turns caramel color and becomes dense, remove the pan from the heat source.
6. Pour the product in a mold of the desired shape.

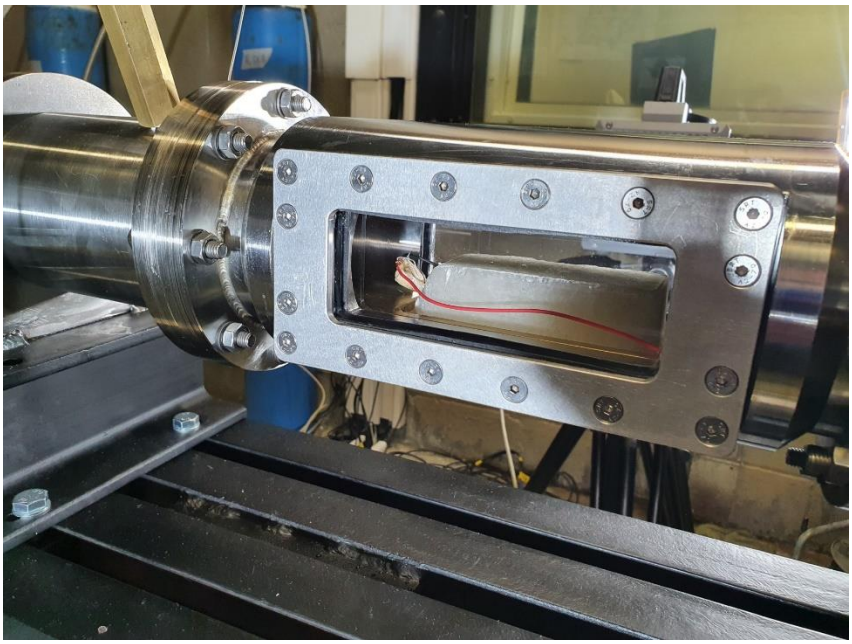

Figure 3.43: *Rocket candy positioned inside the engine.*

3.10 Test Bench

The *MOUETTE* test bench has been designed with the purpose of securing the engine and facilitating the assembly and disassembly procedures.
The test bench consists of a frame Table on which a steel component, called Sole, is mounted. The Sole is characterized by two rails on which double-t components can be fixed in the desired position. The technical drawing of the frame Table is shown in Figure 3.44, while a picture of the Table with the Sole on it is provided in Figure 3.45. The Table features four wheels, each one equipped with a brake, to ensure easy mobility.

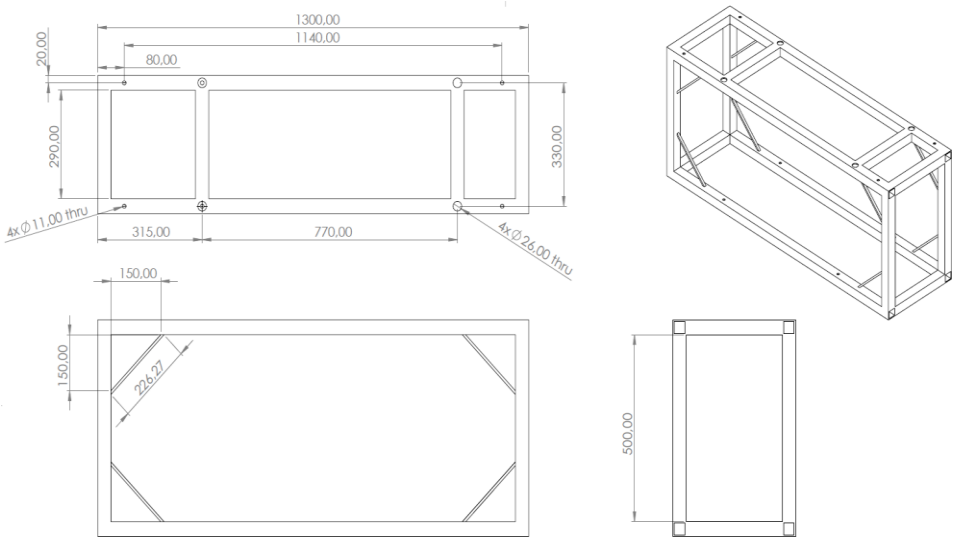

Figure 3.44: *Technical drawing of the frame Table.*

Figure 3.45*: Picture of the frame Table with Sole on it.*

To properly design the fastening of *MOUETTE* to the test bench, the generated thrust was estimated. Knowing the chamber pressure, the oxidizer mass flow rate and estimating the fuel mass flow rate as explained in Subsection 3.7.2., the combustion temperature was computed with *Rocket Propulsion Analysis* software. Afterwards, the temperature and the pressure at the Nozzle exit (T_{eff},p_{eff}) were calculated from the isentropic flow relations, considering that the convergent Nozzle was designed to be choked, hence featuring a *Mach* number equal to 1 at its efflux section (M_{eff} = 1). Finally, the efflux velocity of combustion products from the Nozzle and the thrust generated were computed with Equation 3.13 and 3.14, respectively. The maximum thrust generated for the conditions of maximum chamber pressure and oxidizer mass flow rate was estimated to be around 100 N.

$$v_{eff} = M_{eff}\sqrt{R\,\gamma\,T_{eff}} \tag{3.13}$$

$$F = \left(\dot{m}_{ox} + \dot{m}_f\right) v_{eff} + \left(p_{eff} - p_{amb}\right) A_t \tag{3.14}$$

It was therefore chosen to lay the engine on two Supports in correspondence of the Pre-Chamber and Post-Chamber, with fixing ensured by two Clamps. Each Support is welded on the respective double-t component. Since the thrust, although low, is not negligible, the Pre-Chamber and the Post-Chamber have been machined to present a groove to accommodate the Supports and the Clamps (see Figure 3.46), with the purpose of avoiding a possible sliding of the motor in axial direction. The detail of the connection between the engine, the Support and the Clamp is shown in Figure 3.47, while a picture of *MOUETTE* assembled to the test bench is provided Figure 3.48.

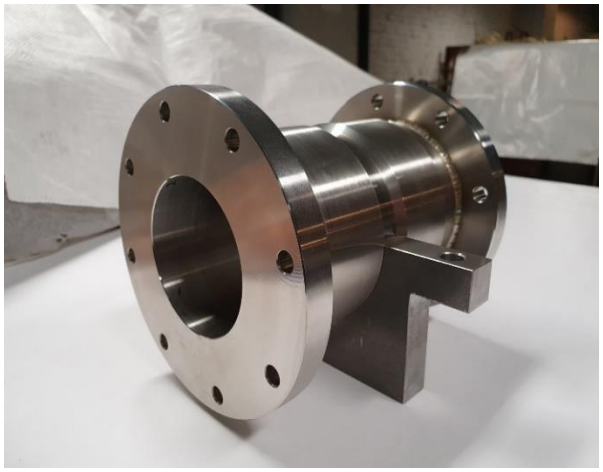

Figure 3.46: *Picture of the Post-Chamber with particular attention to the central groove.*

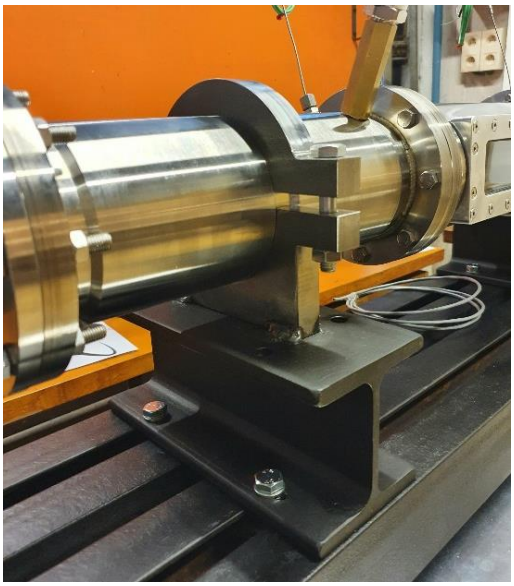

Figure 3.47: *Detail of the Pre-Chamber connection to the test bench.*

The feed line was installed on a grid panel by means of pipe supports, in order to have a certain gap between pipes and grid to ensure the opening and closing of manual valves and an easy working on tube fittings. The panel was then fixed on a lateral side of the Table with screws (Figure 3.49).

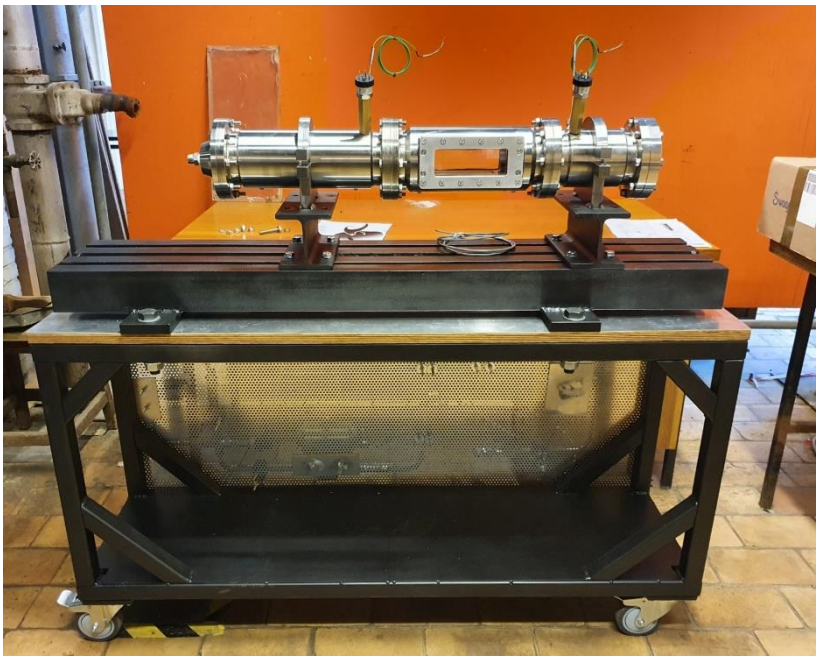

Figure 3.48: *MOUETTE test bench.*

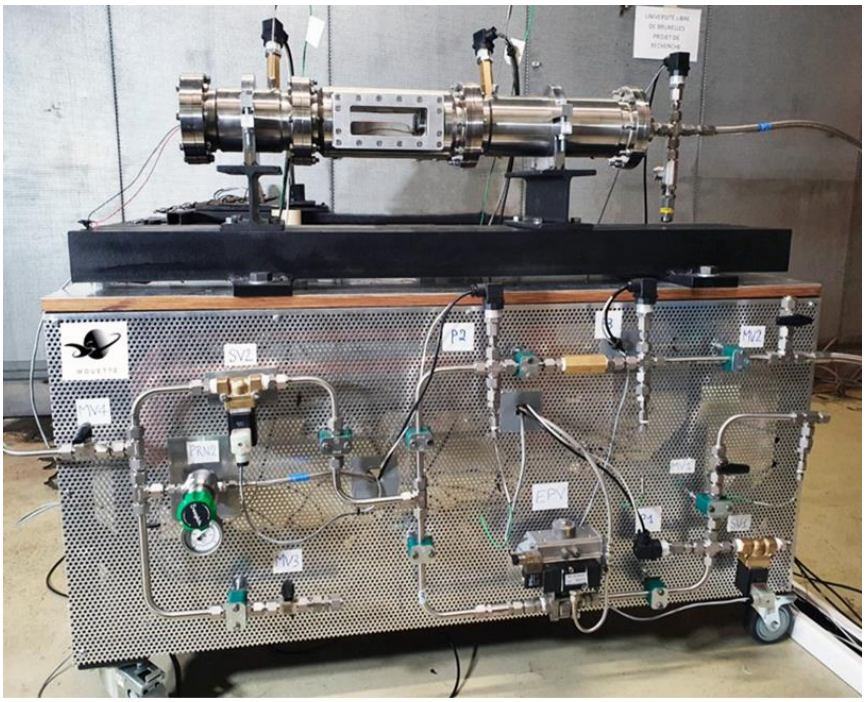

Figure 3.49: *Feedline mounted on the test bench.*

4. Engine Commissioning and Experimental Activity

4.1 Test Facility

Engine pressurization tests and a verification test campaign have been conducted at the Belgian Air Component Air Base of Beauvechain. The test facility consists of a safe room with an exhaust gas duct enabling to perform firing tests, and an adjacent control room featuring a bulletproof glass to allow a view of the test room interior. In addition to the test bench, the safe room comprises, for safety reasons, a shelter for tanks. The control room is equipped with the apparatus to remotely control the engine and to acquire and record measurements. The organization, the arrangement and the equipment of the test facility is shown in Figure 4.1.

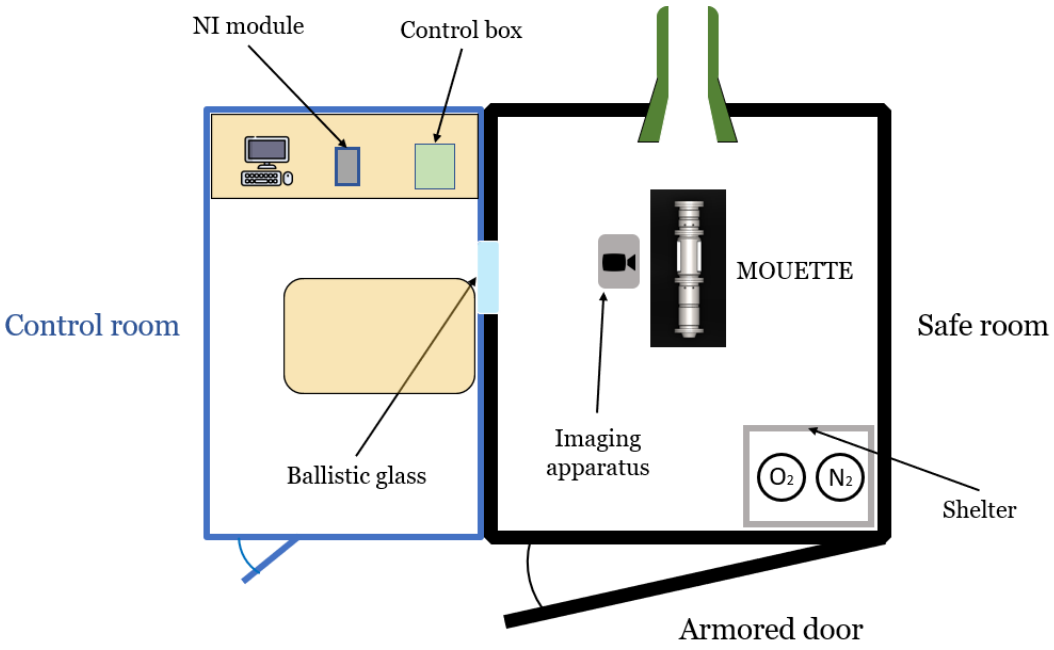

Figure 4.1: *Schematic of the test facility at Beauvechain Air Base.*

4.2 Data Acquisition and Control System

A LabVIEW program was developed to manage a National Instruments (NI) DAQmx USB 6218 data acquisition, processing and distribution system, which function is to acquire sensor data and control solenoid valves and ignition to perform tests.
For data acquisition, the signal from pressure sensors and thermocouples is transmitted as input to the NI card via low impedance (50 Ohm) coaxial cables, connected to it through BNC adapters. To control each test, the NI module, managed by a LabVIEW Virtual Instrument panel, commands the opening/closing of solenoid valves and sends current to the nichrome wire for ignition by operating relays located in a control box, along with a power supply. The electrical schematic of the control box is reported in Figure 4.2.

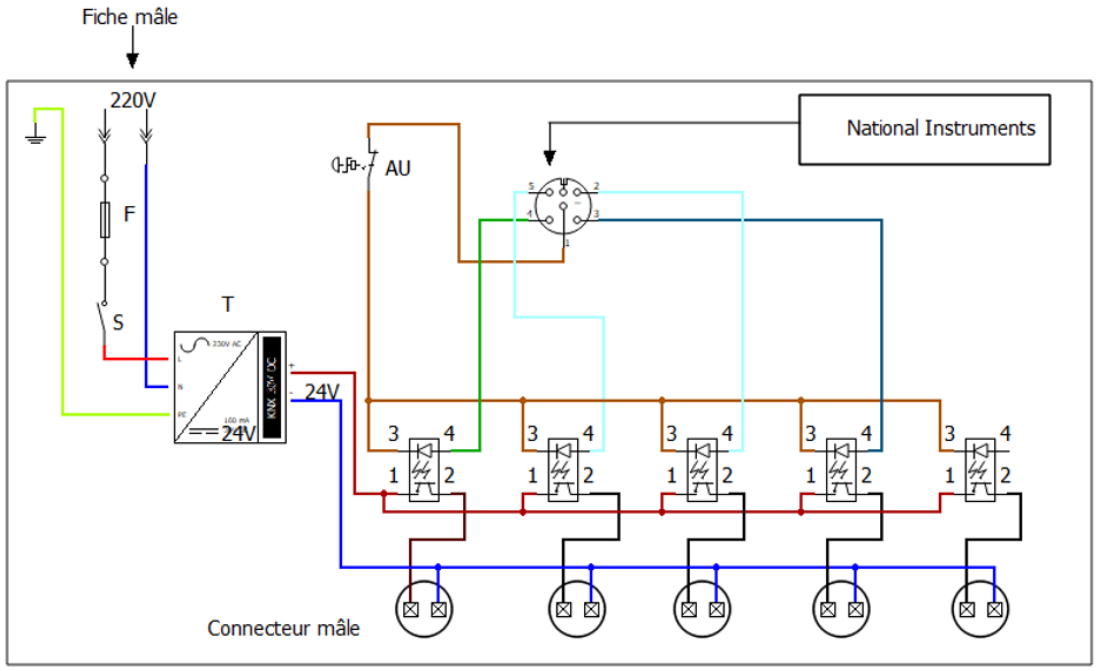

Figure 4.2: *Electrical schematic of the control box.*

The Virtual Instrument (VI) allows recording of test data and 'manual' control of valves thanks to the interactive panel shown in Figure 4.3. In order to grant a fast update frequency, the LabVIEW program has been developed to manage: a) data acquisition and valve control, b) data recording and writing and c) data display on the screen, by means of three independent but inter-communicating loops.
In addition, once "*Start sequence*" is pressed, the VI is programmed to automatically execute a series of operations to independently complete a test. The automatic procedure is explained in the following.

Before running a test, the program requires to enter the test time, the purge time and the maximum allowed chamber pressure. The program then starts reading and

recording data from the sensors and, at a specified instant of time, power is supplied to the nichrome wire wrapping the igniter. Once the *rocket candy* is ignited and generates hot gases, the program opens the electro-pneumatic valve, which is oxygen main run valve, to begin the solid fuel sample burning. Oxygen hence flows to feed the combustion process. After the pre-specified test time, the oxygen valve is closed and the solenoid valve in the nitrogen line is opened to purge the engine and extinguish the combustion process.
If, during the test, the chamber pressure exceeds the pre-specified maximum value, the program automatically terminates the normal test procedure, closes the oxygen valve and opens the nitrogen line to cease combustion.
The direct control of electro valves using their respective buttons becomes effective, and the "*Start sequence*" button is enabled, only when all the switches on the checklist are turned on, in such a way to be sure that all the necessary procedures to perform a safe and correct test are completed.

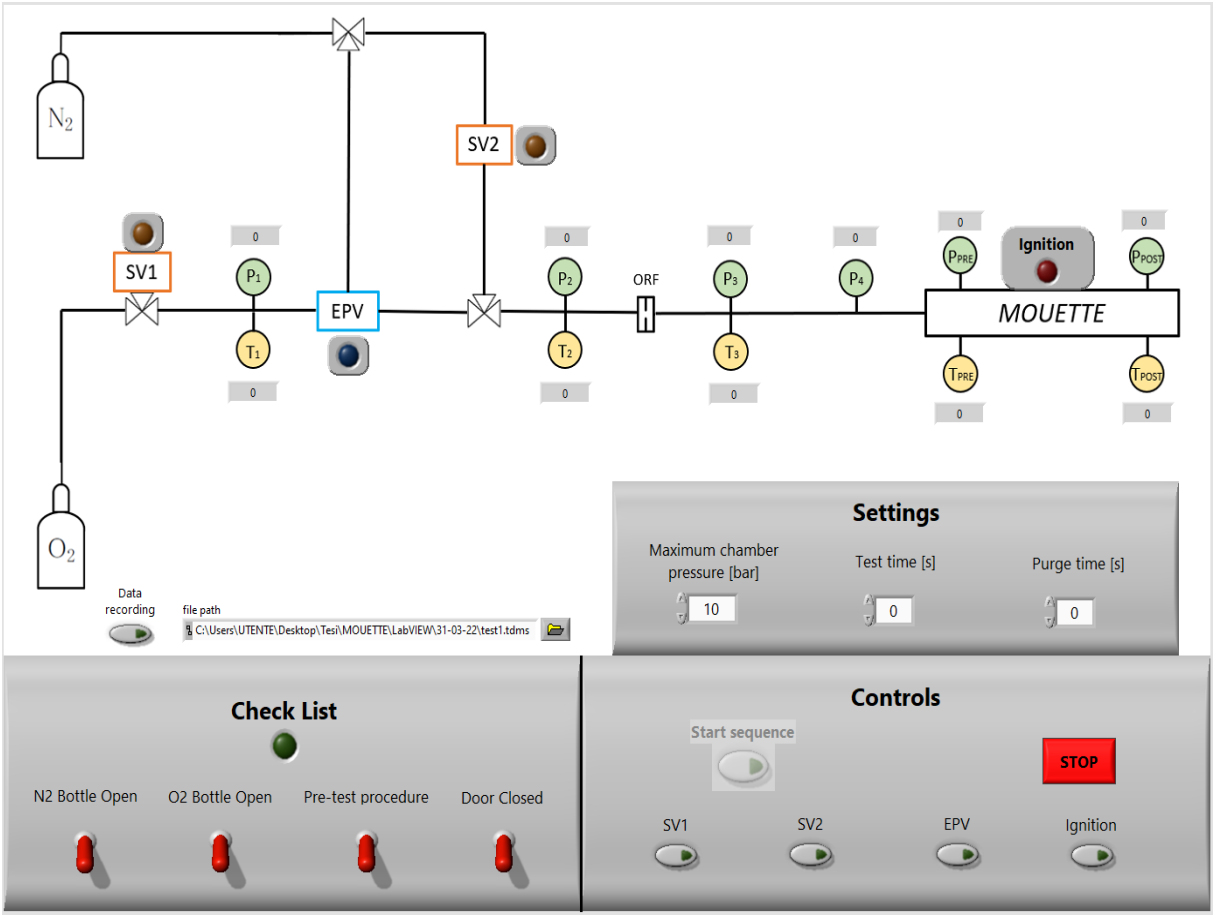

Figure 4.3: *LabVIEW Virtual Instrument panel.*

4.3 Imaging Apparatus

The hybrid combustion in the engine is visualized via high-speed imaging together with different chemiluminescence filters. High-speed videos are recorded using a Photron FASTCAM SA4, courtesy of the Royal Military Academy of Belgium, a high-performance high-speed camera able to record up to 30000 fps, operated by the Photron FASTCAM Viewer software (PFV).

Imaging of excited species, such as OH* and CH*, is nowadays a popular technique used to visualize combustion processes and study flames. It is based on chemiluminescence, i.e. the emission of light as the result of a chemical reaction. In an exothermic chemical reaction, such as combustion, the molecules of combustion products are excited, resulting in an excited electronic state. When this state decays into an electronic ground state, an electromagnetic radiation is emitted. In the combustion reaction zone, chemiluminescence can thus provide information about OH*, CH*, C_2* and CO_2* radicals, which are responsible for much of the visible and ultraviolet chemiluminescence in typical hydrocarbon flames [44].

The arrangement of the test bench and the imaging apparatus is shown in Figure 4.4.

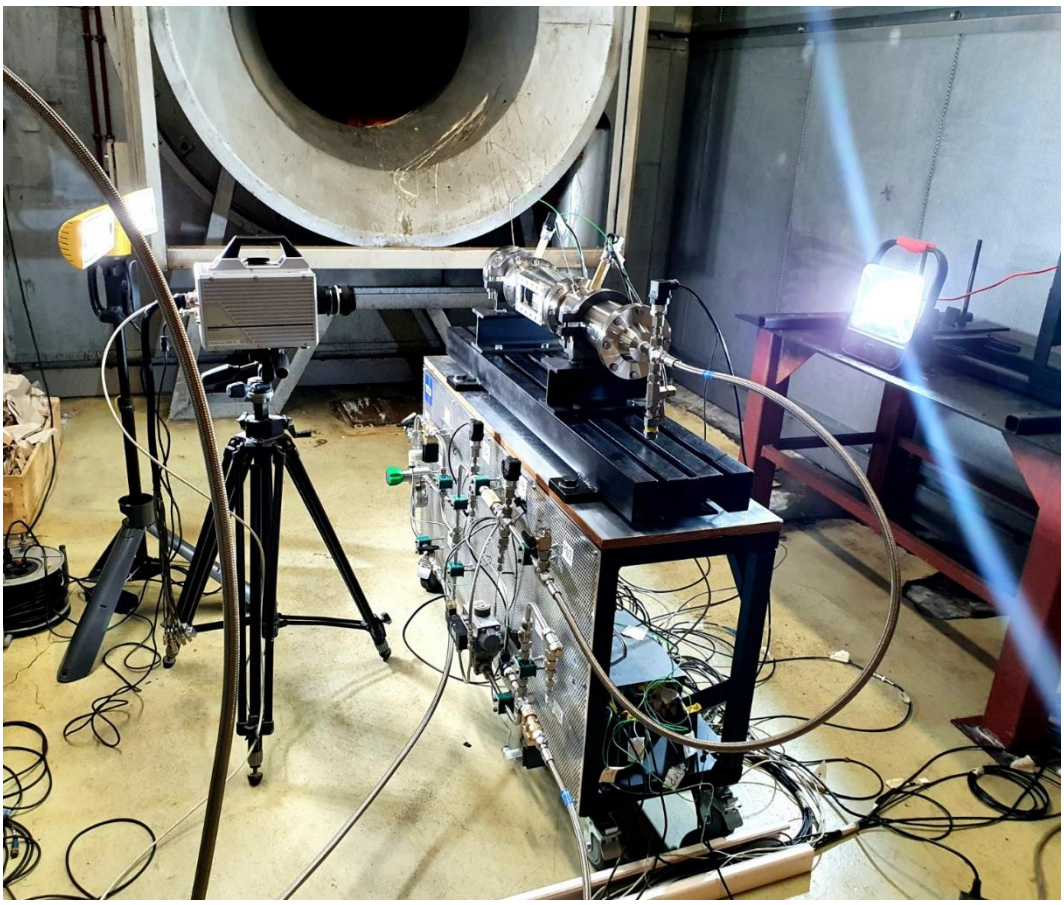

Figure 4.4: *Test bench and imaging apparatus.*

4.4 Verification Test Campaign

A verification test campaign of *MOUETTE* engine and related testing apparatus was conducted at Beauvechain Air Base in early April 2022.

Initially, cold flow pressure tests were carried out to assess the overall behavior of the feed system, engine's mechanical components and related bolted connections, with the result that, after a careful final setup of gasket arrangement in the area of the Main-Chamber windows, the equipment proved to be successfully capable of withstanding high levels of inside pressure, without showing any leakage.

Afterwards, various ignition tests were performed to verify the operation of the *rocket candy* as a pyrotechnic igniter over the desired range of oxidizer mass flow rates and combustion chamber pressures. Figure 4.5 shows *MOUETTE* engine during the first ignition test carried out with $\dot{m}_{ox}$ of 50 g/s, Injector Plate B and Nozzle with throat diameter of 20 mm.

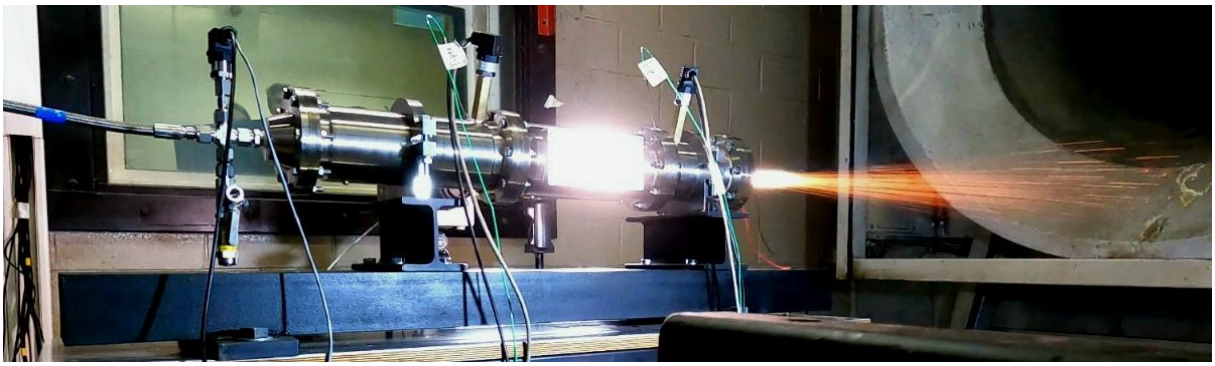

Figure 4.5: *MOUETTE first firing test (31/03/2022).*

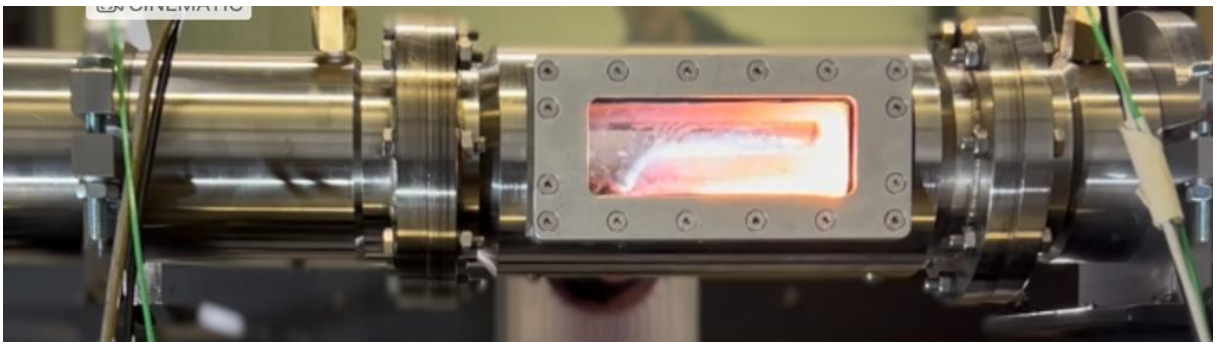

Figure 4.6: *MOUETTE firing test, detail of the combustion process.*

Combustion tests were conducted successfully and the recorded chamber pressure data were in good agreement with the design values. All mechanical equipment, the instrumentation, the feed system, the bench, the support structure, and the engine itself performed as expected. Furthermore, the data acquisition and control system properly supported each operational step and allowed for the full completion of each

test without any inconvenience. Figure 4.6 shows how the combustion of the paraffin grain develops inside MOUETTE 's Main-Chamber and was captured by a standard camera.

In addition to the verification of the engine operation, the preliminary test campaign was carried out with the goal of setting up the high-speed camera apparatus and tune the recording of high-speed and chemiluminescence videos, as well as the related data processing.
Figure 4.7 provides the high-speed images showing the development of the flame over the fuel grain surface during the ignition phase. However, the following fully-developed combustion process was observed to be too bright for the visualization with the high-speed camera alone, resulting in total overexposure.

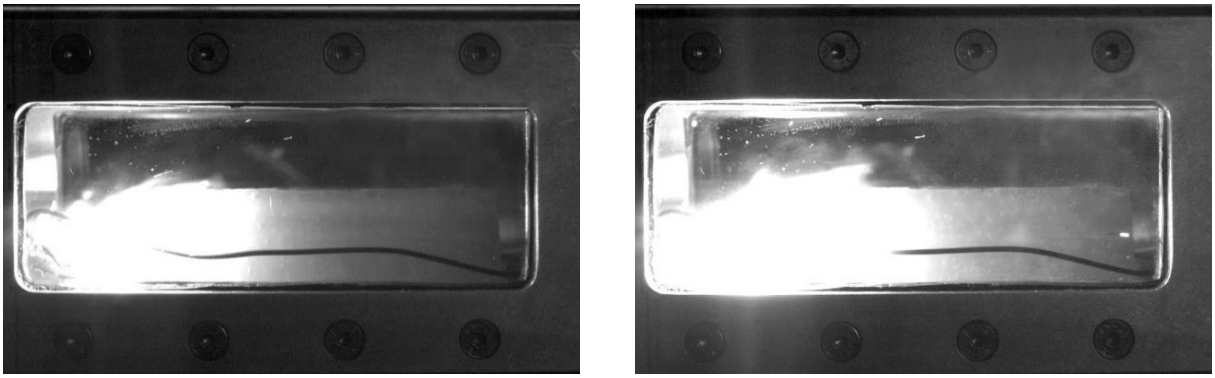

Figure 4.7: *High-speed images of the flame development over the fuel surface during ignition. Oxygen flows from left to right.*

The high-speed camera was then equipped with CH* and OH* chemiluminescence filters that, after a careful tuning of the camera settings and the video recording program, provided an excellent visualization of the combustion process.
Figures 4.8 and 4.9 show examples of the captured CH* and OH* chemiluminescence images, respectively. For both filters, videos were recorded with a frame rate of 1000 fps and a shutter speed of 1/frame seconds, while the diaphragm opening in the light path of the objective was 5.6 for CH* filter and 2.8 for OH* filter.

The OH* chemiluminescence images in Figure 4.9 are particularly significant and very encouraging for the whole research project. In fact, although preliminary, they show the development of roll waves in the reacting boundary layer over the fuel grain that, according to state-of-the-art theory and experimental results, characterize the hybrid combustion process of liquefying solid fuels. As predicted by Kelvin-Helmholtz instability theory, i.e. the fluid instability that occurs when there is a velocity difference across the interface between two fluids, hydrodynamic and surface tension forces lead to deformation of the interface between the liquid paraffin layer and gaseous oxygen, resulting in the formation of axial waves. The development of roll waves is a key event in the onset of the droplet entrainment phenomenon.

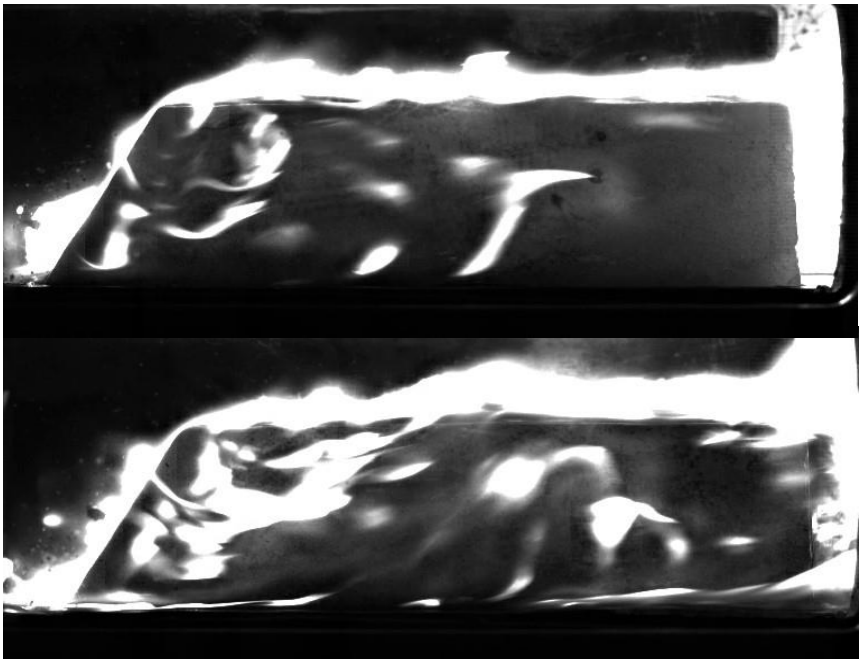

Figure 4.8: *CH* chemiluminescence images of paraffin combustion at 5 bar. Oxygen flows from left to right.*

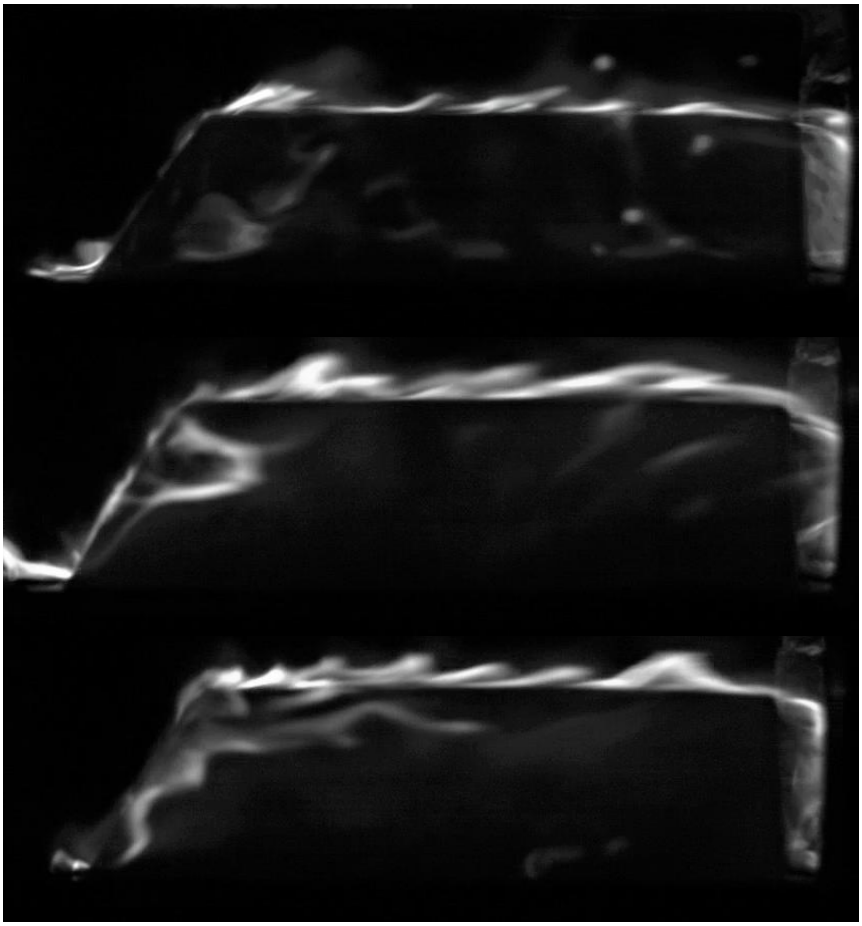

Figure 4.9: *OH* chemiluminescence images of paraffin combustion at 2.5 bar, detected development of roll waves. Oxygen flows from left to right.*

In conclusion, the preliminary test campaign resulted to be successful as the engine and the associated test equipment were verified to operate as intended during the design phase.
Furthermore, although some tuning work still needs to be done to optimize the performance of the system, especially concerning visualization techniques, the collected high-speed images have confirmed the effective possibility to study the internal ballistics of hybrid rocket combustion with *MOUETTE* engine.

5. Conclusions and Future Developments

MOUETTE, a hybrid rocket engine with optical access, was developed during this thesis work. To have designed a rocket engine from scratch, commissioned it, and had it operational in just 6 months was a quite significant accomplishment.
The combustion visualization facility was conceived to enable a deep comprehension of the challenging internal ballistics of hybrid rocket engines via visual analysis, even at paraffin-based fuels supercritical pressure conditions. Real-time data of the combustion process will not only allow an extensive characterization of the phenomenon, but also support an improvement of numerical models for CFD simulations, which are currently not accurate enough, especially for liquefying solid fuels. The project was developed with the mission of increasing the *Technology Readiness Level* of hybrid propulsion, in order to make it a competitive candidate for the next generation of launch systems and in-space missions.
The engine is capable of operating under a wide range of operating conditions, both in terms of oxidizer mass flow rate and combustion chamber pressure, and the verification test campaign has confirmed the goodness of the project. The combustion visualization facility, in fact, allows to analyze the internal ballistics of liquefying solid fuels, characterized by the entrainment process, through the images recorded by a high-speed camera equipped with OH* and CH* chemiluminescence filters.
The engine, as it is, is ready for the start of experimental campaigns regarding the characterization of the hybrid combustion process at different chamber pressures and the analysis of the effects of different propellant grain geometries and additives on the internal ballistics.

In order to visualize in even more detail the turbulent reacting boundary layer, the fuel melt layer on the grain surface and the entrainment of droplets, it would be interesting to install in the future a schlieren imaging apparatus, such as the background-oriented schlieren (BOS). The BOS is an optical density visualization technique that uses the distortion and the displacement of the image of a background dot panel, caused by local density gradients, to reconstruct the flow field. Moreover, it could be developed

an algorithm to process high-speed images and track the evolution of the entrained droplets in the boundary layer and in the oxidizer flow.

The modular structure of *MOUETTE* ensures simple mounting procedures and provides access to the inside of the motor, so that the components affecting the operating conditions, namely the injection plate and nozzle, can be easily replaced as needed. In addition, the modular design gives the engine a particularly advantageous feature for scientific research: versatility. For example, in the future it would be possible to operate *MOUETTE* as a more conventional hybrid engine, i.e. without optical access and with a cylindrical fuel grain, by simply replacing or eliminating the Main-Chamber.

Finally, as further future developments, it would be interesting to design and integrate a system for the collection, sampling and analysis of combustion products and, in addition, to characterize experimentally and with visual investigations the re-ignition process inside a hybrid propulsion engine.

APPENDIX A – Hybrid Combustion Model

The combustion model for a hybrid rocket engine proposed by Marxman et al. [6] is here reported.
Assuming quasi-steady conditions and neglecting thermal radiation:

$$\dot{Q}_c = \rho_f \, \dot{r} \, \Delta H_f \tag{A.1}$$

where $\dot{Q}_c$ is the convective heat flux (heat transfer per unit area) to the grain surface, ρ_f the fuel density, $\dot{r}$ the regression rate and ΔH_f the effective heat of gasification of the solid fuel. The effective heat ΔH_f is the total energy required to gasify a unit mass of solid fuel originally at the internal temperature of the solid grain.
To derive a useful expression of the regression rate, Marxman et al. made the following assumptions.

1) The gas mixture, composed by two groups of components having molecular weights of the same order and similar collision cross sections, may be replaced by an effective binary mixture.
2) Lewis number, the ratio of thermal diffusivity to mass diffusivity, is assumed to be equal to unity ($Le = 1$).
3) Prandtl number, the ratio of viscous diffusion to thermal diffusion, is assumed to be equal to unity ($Pr = 1$).

As consequence, if the Reynolds analogy is valid, i.e. the transport of energy and momentum in a boundary layer are similar, the heat flux is then independent of both the transport mechanism and the magnitudes of reaction rates, and it is described by an equation formally identical to that for a pure, nonreacting gas. The convective heat flux at the fuel surface or wall (subscript w) can be therefore written as:

$$(\dot{Q}_c)_w = \left(\frac{\lambda}{C_p} \frac{\partial h}{\partial y} \right)_w \tag{A.2}$$

where λ is the thermal conductivity, C_p is the specific heat at constant pressure, h is the sum of sensible (thermal) and chemical (heat of formation) enthalpies and y is the coordinate normal to the fuel surface.
The convective heat transfer coefficient, also referred as Stanton number (C_h), defined in terms of the mass flux and enthalpy at the flame, with subscript c referring to the conditions at the location where combustion occurs, i.e. at the flame, is:

$$C_h = \frac{(\dot{Q}_c)_w}{\rho_c \, u_c \, (h_c - h_w)} \tag{A.3}$$

Substituting Equations A.3 and A.2 in Equation A.1:

$$\rho_f \, \dot{r} \, \Delta H_f = C_h \, \rho_c \, u_c \, (h_c - h_w) = C_h \, \rho_c \, u_c \, \Delta h \tag{A.4}$$

Applying Reynold analogy and considering $Pr = 1$, the heat exchange coefficient C_h may be linked to the local surface friction coefficient:

$$C_h = C_f \frac{\rho_e u_e^2}{2\,\rho_c\, u_c^2} \tag{A.5}$$

where $C_f \equiv \frac{\tau_w}{\frac{1}{2}\rho_e u_e^2}$ and the subscript e refers to undisturbed flow conditions (boundary layer edge), and the following expression is obtained:

$$C_h = \frac{\rho_f\, \dot{r}\, \Delta H_f}{\rho_c\, u_c\, \Delta h} = C_f \frac{\rho_e u_e^2}{2\,\rho_c u_c^2} \tag{A.6}$$

The phenomenon of the blocking effect, i.e. the reduction of the convective heat transferred from the flame region to the grain surface because of the diffusion in the flow of vaporized fuel mass, is accounted through the non-dimensional blowing parameter B. In particular, the friction (C_f) and the heat transfer (C_h) coefficients are corrected with the following experimental relationship [8]:

$$\frac{C_f}{C_{f0}} = \frac{C_h}{C_{h0}} = \left[\frac{\ln(1+B)}{B}\right]^{4/5} \left[\frac{1 + 1.3B + 0.364B^2}{\left(1+\frac{B}{2}\right)^2 (1+B)}\right]^{1/5} \tag{A.7}$$

where C_{f0} and C_{h0} are the same coefficient without considering the blocking effect.
The blowing parameter is defined according to Equation A.8:

$$B \equiv \frac{2\,(\rho\, u)_w}{\rho_e\, u_e\, C_f} = \frac{u_e}{u_c} \frac{(h_c - h_w)}{\Delta H_f} = \frac{u_e}{u_c} \frac{\Delta h}{\Delta H_f} \tag{A.8}$$

Combining Equation A.6 and A.8, the regression rate results:

$$\dot{r} = \frac{\rho_e\, u_e\, C_f\, B}{2\,\rho_f} \tag{A.9}$$

Then, Marxman et al. observed that, for the range $5 \le B \le 100$, which encompasses most hybrid operation, the expression A.7 may be approximated with a much simpler relation:

$$\frac{C_f}{C_{f0}} = \frac{C_h}{C_{h0}} = 1.2\, B^{-0.77} \tag{A.10}$$

with the friction coefficient without blowing:

$$\frac{C_{f0}}{2} = 0.03\, Re_x^{-0.2} \tag{A.11}$$

Finally, considering that $Re_x = \frac{\rho_e\, u_e\, x}{\mu}$ and that $G = \rho u$ is a mass flux, the regression rate expression is:

$$\dot{r} = 0.036\, \frac{G^{0.8}}{\rho_f} \left(\frac{\mu}{x}\right)^{0.2} B^{0.23} \tag{A.12}$$

APPENDIX B – List of MOUETTE components

P/N	Description	Material
MOUPR001	FlangeMain	AISI 304L
MOUPR002	FlangePre/Post	AISI 304L
MOUPR003	PreChamber	AISI 304L
MOUPR004	PostChamber	AISI 304L
MOUPR005	InjectorHead	AISI 304L
MOUPR006	InjectorPlate-A	Brass (C360)
MOUPR007	MainChamber	AISI 304L
MOUPR008	NozzlePlate	AISI 304L
MOUPR009	GrainHolder	Brass (C360)
MOUPR010	PreChamberInsert	Brass (C360)
MOUPR011	WindowFrame	Aluminum
MOUPR012	1/8NPT-G1/4BSPP Adapter	Brass (C360)
MOUAS013	MainChamber-Welded	AISI 304L
MOUAS014	PostChamber-Welded	AISI 304L
MOUAS015	PreChamber-Welded	AISI 304L
MOUAS016	MOUETTE-Metalworks	/
MOUPR017	InjectorPlate-B	Brass (C360)
MOUPR018	Glass	Quartz
MOUPR019	Convergent	Graphite
MOUPR020	Nozzle-A	Graphite
MOUPR021	Nozzle-B	Graphite
MOUPR022	Nozzle-C	Graphite
MOUPR023	Nozzle-D	Graphite
MOUPR024	Nozzle-E	Graphite
MOUPR025	Support	Steel
MOUPR026	Clamp	Steel
MOUPR027	Orifice	Brass (C360)
MOUPR028	Table - test bench	Steel
MOUPR029	Mold for paraffin grain	PLA

Table B: *List of MOUETTE's components.*

APPENDIX C – Stress analysis of hollow bars

With the purpose of knowing the allowable internal pressure supported by the engine combustion chambers, a structural analysis of hollow bars was performed following the guidelines proposed in Reference [45].

The first step in calculating the stress distribution in thick cylindrical vessels consists of determining the tangential (σ_t) and radial (σ_r) stresses in an undefined cylinder, open at the ends and subjected to internal pressure p_i and external pressure p_e. For symmetry reasons, σ_t and σ_r are functions of the radius r only, which results in being the only independent variable in the problem.
Considering the generic elementary cube in Figure C.1a, with two faces directed radially and two faces directed tangentially with respect to the circumference of center O, the stresses σ_t and σ_r can be calculated by imposing equilibrium on translation in the radial direction and compatibility of the strains ϵ_t and ϵ_r induced by the stresses.
The expressions of σ_t and σ_r obtained by solving the resulting system of two linear differential equations of the first order with variable coefficients, solved imposing the boundary conditions C.1 and C.2, are reported in Equations C.3 and C.4.

$$for \quad r = R_i, \quad \sigma_r = -p_i \tag{C.1}$$

$$for \quad r = R_e, \quad \sigma_r = -p_e \tag{C.2}$$

$$\sigma_t(r) = \frac{1}{R_e^2 - R_i^2}\left[p_i R_i^2\left(1 + \frac{R_e^2}{r}\right) - p_e R_e^2\left(1 + \frac{R_i^2}{r}\right)\right] \tag{C.3}$$

$$\sigma_r(r) = \frac{1}{R_e^2 - R_i^2}\left[p_i R_i^2\left(1 - \frac{R_e^2}{r}\right) - p_e R_e^2\left(1 - \frac{R_i^2}{r}\right)\right] \tag{C.4}$$

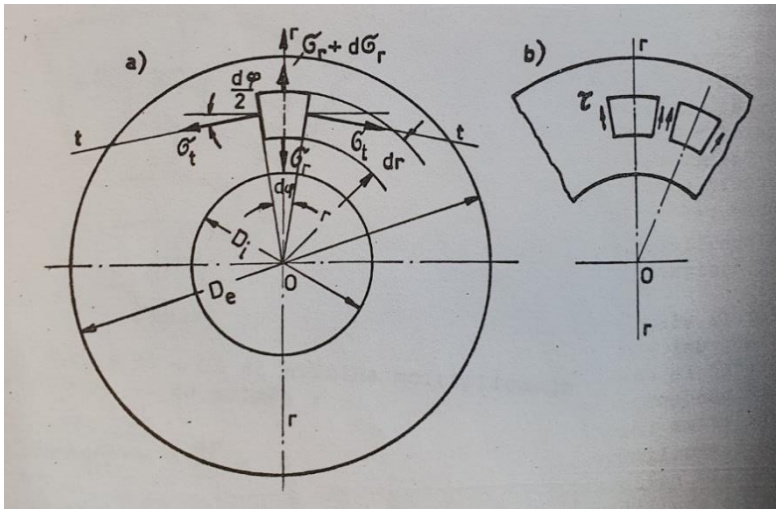

Figure C.1: *Representation of a generic elementary cube in a thick cylindrical vessel [45].*

For a thick cylindrical vessel closed at the ends, there is additionally a constant axial tensile stress:

$$\sigma_a = \frac{\pi\, R_i^2\, (p_i - p_e)}{\pi\, (R_e^2 - R_i^2)} \tag{C.5}$$

It is possible to demonstrate that the tangential, radial and axial stresses are, in any point, principal stresses, i.e. acting on planes on which shear stresses are nil. Considering the generic elementary cube in Figure C.1b, one has that, by load symmetry, the shear stresses (τ) should both be in the same direction. Then, considering an elementary cube placed side by side to the previous one, for geometric and load symmetry with respect to the center O, the τ should be equal and equally arranged. However, for the principle of action and reaction, the τ on flanked faces must be equal and opposite. As consequence, the shear stresses result to be equal to zero.

The stress diagrams as a function of radius (with r going from R_i to R_e) are shown in Figure C.2. It is evident that σ_t and σ_r are both maximum in absolute value at the internal radius.

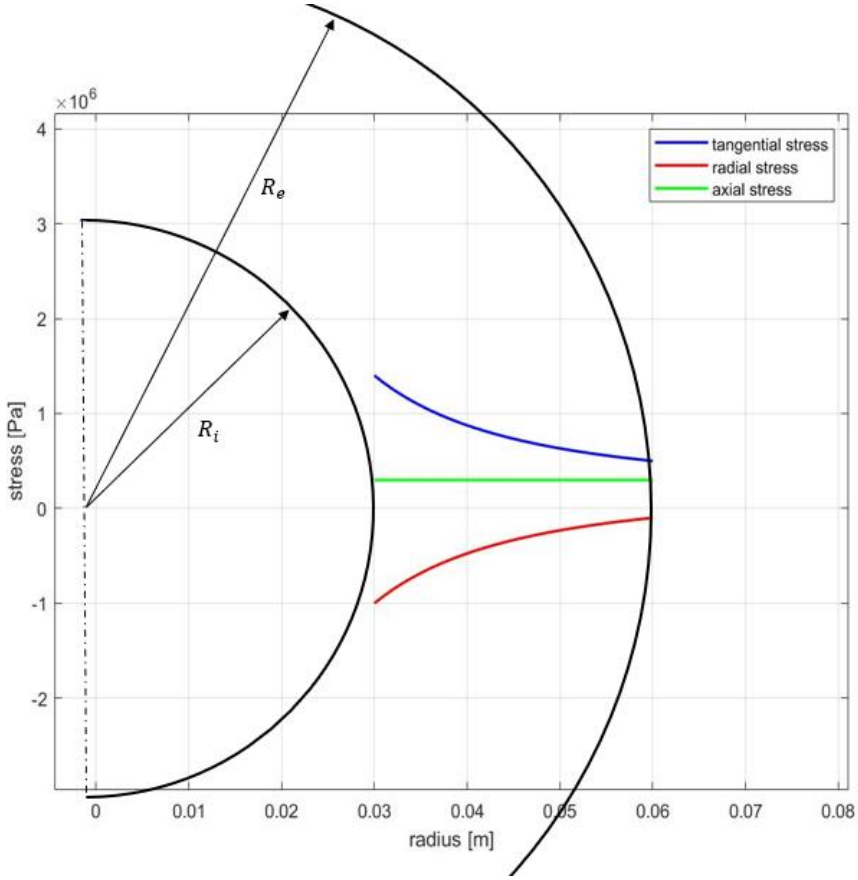

Figure C.2: *Diagrams of σ_t, σ_r and σ_a along the cylinder thickness as a function of the radius. Stress calculated with generic values, namely R_i=0.03 m, R_e=0.06 m, p_i=10 bar and p_e=1 bar.*

To obtain the equivalent stress (σ^*) and apply a strength criterion, the maximum tangential and radial stresses are then considered, see Equations C.6 and C.7.

$$\sigma_t(r = R_i) = \sigma_{t,max} \tag{C.6}$$

$$\sigma_r(r = R_i) = \sigma_{r,max} \tag{C.7}$$

By applying the maximum shear stress theory and the Tresca-Guest criterion:

$$\tau_{max} = \frac{1}{2}\max\left(|\sigma_{t,max} - \sigma_{r,max}|, |\sigma_{r,max} - \sigma_a|, |\sigma_a - \sigma_{t,max}|\right) = \frac{1}{2}\sigma_y \tag{C.8}$$

$$|\sigma_{t,max}| > |\sigma_a| > |\sigma_{r,max}| \tag{C.9}$$

and considering that Equation C.9 is always verified, the strength criterion results:

$$\sigma^* = |\sigma_{t,max} - \sigma_{r,max}| \leq \sigma_y \tag{C.10}$$

where σ_y is the tensile yield strength.

By computing the equivalent stress σ^* and comparing it to the tensile yield strength of AISI 304L stainless steel, which is 210 Mpa, it was therefore possible to estimate the maximal internal pressure supported by the hollow bars used for the building of the Pre-Chamber, Main-Chamber and Post-Chamber. Considering an external pressure p_e equal to atmospheric one, the maximum allowed pressures inside the chambers are reported in Table C.

As expected, stainless steel hollow bars are capable of withstanding very high internal pressure. It should be noted that the chambers are not sized to withstand the maximum 15 bar pressure of the engine chamber, but to meet the optical accessibility requirement.

Hollow bar	Dimensions [m]	Maximum allowed internal pressure [bar]
Pre-Chamber & Post-Chamber	$R_i = 0.037,\ R_e = 0.054$	550
Main-Chamber	$R_i = 0.037,\ R_e = 0.06$	650

Table C: *Maximum allowed internal pressure for the AISI 304L stainless steel hollow bars used for MOUETTE's chambers manufacturing.*

Bibliography

[1] Altman, D., and Holzman, A., “Overview and History of Hybrid Rocket Propulsion”, *Fundamentals of Hybrid Rocket Combustion and Propulsion*, American Institute of Aeronautics and Astronautics, Jan. 2007, pp. 1-33.

[2] Chiaverini, M., “Review of Solid-Fuel Regression Rate Behavior in Classical and Nonclassical Hybrid Rocket Motors”, *Fundamentals of Hybrid Rocket Combustion and Propulsion*, American Institute of Aeronautics and Astronautics, Jan. 2007, pp. 37-126.

[3] Alkuam, E.A. and Alobaidi, W.M., “Experimental and Theoretical Research Review of Hybrid Rocket Motor Techniques and Applications”, Advances in Aerospace Science and Technology, 2016, pp. 71-82.

[4] Karabeyoglu, M. A., Cantwell, B. J., and Altman, D., “Development and Testing of Paraffin-Based Hybrid Rocket Fuels”, 37th AIAA/ASME/SAE/ASEE Joint Propulsion Conference, Salt Lake City, UT, 2001.

[5] Karabeyoglu, A., Altman, D., and Cantwell, B. J., “Combustion of Liquefying Hybrid Propellants: Part 1, General Theory", Journal of Propulsion and Power, Vol.18, No. 3, 2002, pp. 610-620.

[6] Marxman, G. and Gilbert, M., “Turbulent Boundary Layer Combustion in the Hybrid Rocket", 9th Symposium (International) on Combustion, Elsevier, 1963, pp. 371-383.

[7] Leccese, G., Cavallini, E., and Pizzarelli, M., "State of Art and Current Challenges of the Paraffin Based Hybrid Rocket Technology”, Italian Space Agency (ASI), AIAA Propulsion and Energy Forum, August 2019.

[8] Marxman, G. A., Wooldridge, C. E., and Muzzy, R. J., “Fundamentals of Hybrid Boundary Layer Combustion,” Heterogeneous Combustion, edited by H. G.Wolfhard, I. Glassman, and L. Green, Jr.,Vol. 15,AIAAProgress in Astronautics and Aeronautics, Academic Press, NewYork, 1964, pp. 485–521.

[9] Gomes, S., Rocco, L., Rocco, J. A., “Swirl Injection Effects on Hybrid Rocket Motors”, Journal of Aerospace Technology and Management, Vol. 7, No. 4, October-December 2015, pp. 418-424.

[10] Quadros, F. D. A., Lacava, P. T., “Swirl Injection of Gaseous Oxygen in a Lab-Scale Paraffin Hybrid Rocket Motor”, Journal of Propulsion and Power, Vol. 35, No. 5, September-October 2019.

[11] Bertoldi, A. E., Veras, C. A. G., Hendrick, P., “Experimental Evaluation of Pressure-Swirl Injection System over Solid Fuel Regression Rate in Hybrid Rockets”, 7th European Conference for Aeronautics and Space Sciences (EUCASS), 2017.

[12] Bouziane, M., Bertoldi, A. E., Lee, D., Milova, P., Hendrick, P., Lefebvre, M., “Design and Experimental Evaluation of Liquid Oxidizer Injection System for Hybrid Rocket Motors”, 7th European Conference for Aeronautics and Space Sciences (EUCASS), 2017.

[13] Risha, G. A., Evans, B. J., Boyer, E., Kuo, K. K., “Metals, Energetic Additives, and Special Binders Used in Solid Fuels for Hybrid Rockets”, Fundamentals of Hybrid Rocket Combustion and Propulsion, American Institute of Aeronautics and Astronautics, 2007, pp. 413-456.

[14] Carrick, P. and Larson, C., “Lab scale test and evaluation of cryogenic solid hybrid rocket fuels", 31st AIAA/SAE/ASME/ASEE Joint Propulsion Conference and Exhibit, San Diego, CA, 1995.

[15] Larson, C., Pfeil, K., DeRose, M., and Garrick, P., “High pressure combustion of cryogenic solid fuels for hybrid rockets", 32nd AIAA/SAE/ASME/ASEE Joint Propulsion Conference and Exhibit, Lake Buena Vista, FL, 1996.

[16] Gramer, D., Rice, E., Knuth, W., Clair, C. St., "Experimental Investigation of a Metallized Cryogenic Hybrid Rocket Engine", 34th AIAA/SAE/ASME/ASEE Joint Propulsion Conference and Exhibit, July 1998.

[17] Clair, C. St., Rice, E., Knuth, W., Gramer, D., "Advanced Cryogenic Solid Hybrid Rocket Engine Developments: Concept and Testing", 34th AIAA/SAE/ASME/ASEE Joint Propulsion Conference and Exhibit, July 1998.

[18] Karabeyoglu, M. A. and Cantwell, B. J., “Combustion of Liquefying Hybrid Propellants: Part 2, Stability of Liquid Films", Journal of Propulsion and Power, Vol. 18, No. 3, 2002, pp. 621-630.

[19] Chandler, A., Jens, E. T., Cantwell, B. J., and Hubbard, G. S., "Visualization of the Liquid Layer Combustion of Paraffin Fuel at Elevated Pressures", 63rd International Astronautical Conference (IAC), Naples, Italy, 2012.

[20] Jens, E. T., Mechentel, F. S., Cantwell, B. J., Hubbard, G. S., and Chandler, A., "Combustion Visualization of Paraffin-Based Hybrid Rocket Fuel at Elevated Pressures", 50th AIAA/ASME/SAE/ASEE Joint Propulsion Conference, Cleveland, OH, 2014.

[21] Muzzy, R., "Schlieren and Shadowgraph Studies of Hybrid Boundary Layer Combustion", AIAA Journal, Vol. 1, No. 9, 1963, pp. 2159-2160.

[22] Strand, L., Ray, R., Anderson, F., and Cohen, N., "Hybrid Rocket Fuel Combustion and Regression Rate Study", AIAA, SAE, ASME, and ASEE, Joint Propulsion Conference and Exhibit, 28 th, Nashville, TN, 1992, p. 1992.

[23] Chiaverini, M. J., Kuo, K. K., Peretz, A., and Harting, G. C., "Regression-Rate and Heat-Transfer Correlations for Hybrid Rocket Combustion", Journal of Propulsion and Power, Vol. 17, No. 1, 2001, pp. 99-110.

[24] Nakagawa, I. and Hikone, S., "Study on the Regression Rate of Paraffin-Based Hybrid Rocket Fuels," Journal of Propulsion and Power, Vol. 27, No. 6, 2011, pp. 1276-1279.

[25] Chandler, A., Jens, E. T., Cantwell, B. J., and Hubbard, G. S., "Visualization of the Liquid Layer Combustion of Paraffin Fuel for Hybrid Rocket Applications", 48th AIAA/ASME/SAE/ASEE Joint Propulsion Conference, Atlanta, GE, 2012.

[26] Kobald, M., Ciezki, H., and Schlechtriem, S., "Optical Investigation of the Combustion Process in Paraffin-Based Hybrid Rocket Fuels", 49th AIAA/ASME/SAE/ASEE Joint Propulsion Conference, San Jose, CA, 2013.

[27] Kobald, M., Verri, I., and Schlechtriem, S., "Theoretical and Experimental Analysis of Liquid Layer Instability in Hybrid Rocket Engines", CEAS Space Journal, Vol. 7, No. 1, 2015, pp. 11-22.

[28] Petrarolo, A., Kobald, M., and Schlechtriem, S., "Liquid Layer Combustion Visualization of Paraffin-Based Hybrid Rocket Fuels", 53rd AIAA/SAE/ASEE Joint Propulsion Conference, Atlanta, CA, 2017.

[29] Petrarolo, A., Kobald, M., and Schlechtriem, S., "Visualization of Combustion Phenomena in Paraffin-Based Hybrid Rocket Fuels at Super-Critical Pressures", 54rd AIAA/SAE/ASEE Joint Propulsion Conference, Cincinnati, OH, 2018.

[30] Paravan, P., Bisin, R., Carlotti, S., Maggi, F., and Galfetti, L., "Diagnostic for Entrainment Characterization in Lique-fying Fuel Formulations", 54rd AIAA/SAE/ASEE Joint Propulsion Conference, Cincinnati, OH, 2018.

[31] Johnsson, J. E., Glarborg, P., and Dam-Johansen, K., "Thermal Dissociation of Nitrous Oxide at Medium Temperatures", 24th Symposiums on Combustion, 1992, pp. 917-923.

[32] Harvey, P. D., "Engineering Properties of Steels", American Society for Metals, Metals Park, OH, 1982.

[33] Albright, L. F., "Albright's Chemical Engineering Handbook", chapter 5.7 Flow Measurement and Control, pp. 453-462.

[34] United States Federal Emergency Management Agency "Handbook of Chemical Hazard Analysis Procedures", 1989, chapter B.3.

[35] Davis, J. R., "ASM Specialty Handbook - Copper and Copper Alloys", ASM International, Metals Park, OH, 2001.

[36] Ihracska, B., Crookes, R. J., Montalvão, D., Herfatmanesh, M. R., Peng, Z., Imran, S., Korakianitis, T., "Material Selection and Detailed Design of Optical Windows Under High Loads", Journal of Material & Design.

[37] Yoder Jr, P.R., "Mounting Optics in Optical Instruments", SPIE Press 2008.

[38] Eriks, "Technical Handbook O-rings", Sealing Elements.

[39] Epidor, "O-ring catalogue", Seals and Rubber Technology.

[40] Sutton, G. P. and Biblarz, O., "Rocket Propulsion Elements", John Wiley & Sons, 2017.

[41] Galfetti, L., Merotto, L., Boiocchi, M., Maggi, F., and DeLuca, L. T., "Experimental Investigations of Paraffin-Based Fuels for Hybrid Rocket Propulsion", 5th European Conference for Aeronautics and Space Sciences (EUCASS), 2013.

[42] Emerson, "Material Guidelines for Gaseous Oxygen Service".

[43] Beeson, H. D., Smith, S. R., and Stewart, W. F., "Safe Use of Oxygen and Oxygen Systems: Handbook for Design, Operation, and Maintenance", ASTM International, 2007.

[44] Nori, V., and Seitzman, J., "Evaluation of Chemiluminescence as a Combustion Diagnostic under Varying Operating Conditions", 46th AIAA Aerospace Sciences Meeting and Exhibit, Reno, NV, 2008.

[45] Massa, E., "Costruzione di Macchine, Volume Secondo", *Elementi delle Macchine*, Tamburini-Masson Editori, Milano 1976.

Acknowledgements

This thesis work for the Master of Science in Aeronautical Engineering lay within the framework of the ASCenSIon project, an innovative training network that aims to identify and advance critical technologies in the field of space access. The project received funding from the European Union's Horizon 2020 research and innovation program, under Marie Skłodowska-Curie grant agreement no. 860956.

At the end of the report, I would like to dedicate a few lines to all those who have contributed to this journey of personal and professional growth.
First of all, I would like to thank my supervisor, Prof. Roberto Andriani of Politecnico di Milano, and Prof. Antonella Ingenito, of the University La Sapienza of Rome, for the support and advice received during the whole thesis work, and also for enabling the collaboration with the Université Libre de Bruxelles.
To the Head of the Aéro-Thermo-Mécanique Department of Université Libre de Bruxelles, Prof. Patrick Hendrick, go my sincere thanks for having warmly welcomed and hosted me throughout the period of my stay in Brussels, continuously helped me in the performance of my work, and made me feel at all times as part of the Department itself.
A special thanks goes to the members of the Rocket Propulsion Group of the Aéro-Thermo-Mécanique Department, Prof. Artur Bertoldi and Dr. Riccardo Gelain, with whom I have daily shared the developments of the project, appreciating their great competence and continuous availability to collaborate.
Thanks to Olivier Berten, Head of the Aéro-Thermo-Mécanique Laboratory, and to his technical collaborators, Yves, Florent, Charly, Lionel and Adrien, for their fundamental operational help in the construction and assembly of the engine and the feed system, as well as in the setting up of the test facility, and thanks to Laurent Ippoliti for his valuable contribution without which it would have been very difficult to set up and make functional the engine's data acquisition and control system.
Thanks also to Shirley, Secretary of the Aéro-Thermo-Mécanique Department because she was irreplaceable in solving some organizational and logistic problems.
All of you have strongly contributed to allow me to live an experience that has been very stimulating and rewarding, from which I have acquired a lot, and of which I am sure I will keep a very pleasant memory for a long time.

Finally, I would like to thank infinitely my mother and my father for always supporting me in life and studies, without your teachings I would not have become the person I am today, and my girlfriend Michela for the wonderful *MOUETTE* logo, but especially for all the time she dedicates to me.

April 11, 2022,
Fabio Angeloni

Ringraziamenti

Questo lavoro di tesi di Laurea Magistrale in Ingegneria Aeronautica è stato svolto nell'ambito del progetto ASCenSIon, una rete di formazione innovativa che mira a identificare e far progredire le tecnologie nel campo dell'accesso allo spazio. Il progetto ha ricevuto i finanziamenti dal programma di ricerca e innovazione Horizon 2020 dell'Unione Europea, sotto il Marie Skłodowska-Curie grant agreement no. 860956.

A conclusione dell'elaborato, vorrei dedicare qualche riga a tutti coloro che hanno contribuito a questo percorso di crescita personale e professionale.
Desidero ringraziare innanzitutto il mio relatore, il Prof. Roberto Andriani del Politecnico di Milano, e la Prof.ssa. Antonella Ingenito, dell'Università La Sapienza di Roma, per il supporto e i consigli ricevuti durante tutto il lavoro di tesi, ed anche per aver reso possibile l'attività di collaborazione con l'*Université Libre de Bruxelles*.
Al Capo del Dipartimento di Aéro-Thermo-Mécanique dell'*Université Libre de Bruxelles*, Prof. Patrick Hendrick, vanno i miei più sentiti ringraziamenti per avermi calorosamente accolto e ospitato per tutto il periodo del mio soggiorno a Bruxelles, continuamente aiutato nello svolgimento del lavoro, e fatto sentire in ogni momento come parte del Dipartimento stesso.
Un ringraziamento speciale va ai componenti del Rocket Propulsion Group del Dipartimento di Aéro-Thermo-Mécanique, Prof. Artur Bertoldi e ing. Riccardo Gelain, con i quali ho quotidianamente condiviso gli sviluppi del progetto, apprezzandone la grande competenza e la continua disponibilità alla collaborazione.
Grazie a Olivier Berten, Responsabile del Laboratorio di Aéro-Thermo-Mécanique, e ai suoi collaboratori tecnici, Yves, Florent, Charly, Lionel e Adrien, per il fondamentale aiuto operativo nelle fasi di costruzione e assemblaggio del motore e della linea di alimentazione, nonché nell'allestimento dell'impianto di prova nel suo complesso, e grazie a Laurent Ippoliti per il prezioso contributo senza il quale sarebbe stato molto difficile predisporre e rendere funzionante il sistema di acquisizione di dati e controllo del motore. Grazie anche a Shirley, Segretaria del Dipartimento di Aéro-Thermo-Mécanique, perché nella soluzione di alcune problematiche organizzative e logistiche è stata insostituibile.
Avete tutti fortemente contribuito a permettermi di vivere un'esperienza che è stata per me molto stimolante e gratificante, dalla quale ho acquisito molto, e della quale sono sicuro conserverò a lungo un ricordo veramente piacevole.

Infine, desidero ringraziare infinitamente mia madre e mio padre per avermi sempre supportato nella vita e nel mio percorso di studi, senza i vostri insegnamenti non sarei diventato la persona che sono oggi, e la mia fidanzata Michela per il magnifico logo *MOUETTE*, ma soprattutto per tutto il tempo che mi dedica.

11 aprile 2022,
Fabio Angeloni